

**U.S. DEPARTMENT OF COMMERCE  
National Technical Information Service**

**AD-A030 278**

**PROCEEDINGS OF THE SPECIAL MEETING ON THE PHYSICS  
OF DETECTORS HELD AT U.S. NAVAL TRAINING DEVICE  
CENTER, ORLANDO, FLORIDA, ON 15 MARCH 1972**

**MICHIGAN UNIVERSITY, ANN ARBOR  
INSTITUTE OF SCIENCE AND TECHNOLOGY**

**AUGUST 1972**

Unclassified

Security Classification

DOCUMENT CONTROL DATA - R & D

(Security classification of title, body of abstract and indexing annotation must be entered when the overall report is classified)

1 ORIGINATING ACTIVITY (Corporate author) Willow Run Laboratories of the Institute of Science and Technology, The University of Michigan, Ann Arbor		2a. REPORT SECURITY CLASSIFICATION Unclassified	
		2b. GROUP	
3 REPORT TITLE PROCEEDINGS OF THE SPECIAL MEETING ON THE PHYSICS OF DETECTORS			
4 DESCRIPTIVE NOTES (Type of report and inclusion dates) Held at the U. S. Naval Training Device Center, 15 March 1972			
5 AUTHOR(S) (First name, middle initial, last name)			
6 REPORT DATE August 1972		7a. TOTAL NO OF PAGES 146	7b. NO OF REFS N/A
8a. CONTRACT OR GRANT NO. N00014-67-A-0181-0031		9a. ORIGINATOR'S REPORT NUMBER(S) 24180-10-X	
b. PROJECT NO		9b. OTHER REPORT NO(S) (Any other numbers than may be assigned this report)	
c.			
d.			
10 DISTRIBUTION STATEMENT Distribution of this document is unlimited.			
11 SUPPLEMENTARY NOTES		12 SPONSORING MILITARY ACTIVITY Office of Naval Research Arlington, Virginia	
13 ABSTRACT  These Proceedings contain 13 papers presented at the unclassified Physics of Detectors Meeting held at The Naval Training Device Center, Orlando, Florida on 15 March 1972.			

DD FORM 1473  
1 NOV 65

Unclassified  
Security Classification

PRICES SUBJECT TO CHANGE

Unclassified

Security Classification

14	KEY WORDS	LINK A		LINK B		LINK C	
		ROLE	WT	ROLE	WT	ROLE	WT
	Noise Semiconductors Lead chalcogenides Optical measurements Lead sulfide films InSb Pyroelectric detectors Infrared detectors Radiation damage Infrared quantum counters						

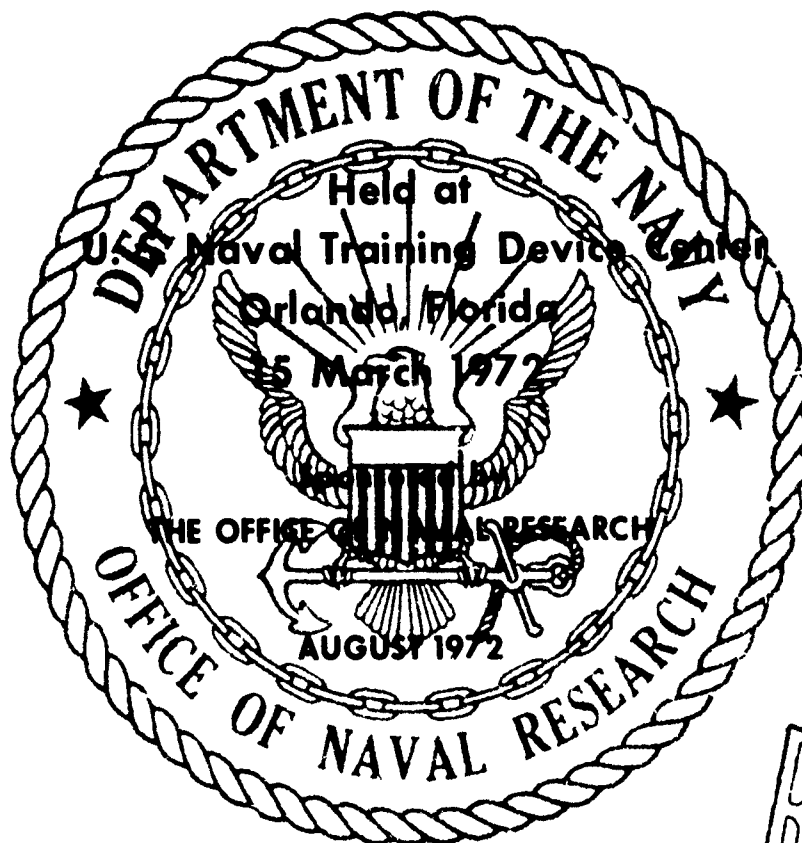
Unclassified

Security Classification

278125

ADA 030278

# PROCEEDINGS OF THE SPECIAL MEETING ON THE PHYSICS OF DETECTORS



Willow Run Laboratories  
Infrared Information and Analysis Center  
Institute of Science and Technology



REPRODUCED BY  
NATIONAL TECHNICAL  
INFORMATION SERVICE  
U. S. DEPARTMENT OF COMMERCE  
SPRINGFIELD, VA. 22161

D D C  
RECEIVED  
SEP 27 1976  
C  
DISTRIBUTION STATEMENT A  
Approved for public release  
Distribution Statement A

# PROCEEDINGS OF THE SPECIAL MEETING ON THE PHYSICS OF DETECTORS

Held at  
Naval Training Device Center  
Orlando, Florida  
15 March 1972

Sponsored by  
The Office of Naval Research  
Arlington, Virginia

Infrared Information and Analysis Center  
Institute of Science and Technology  
Willow Run Laboratories  
The University of Michigan  
Ann Arbor, Michigan

ACCESSION for	
NTIS	White Section <input checked="" type="checkbox"/>
DTIC	Buff Section <input type="checkbox"/>
UNAN OMPED	<input type="checkbox"/>
JUSTIFICATION	
BY	
DISTRIBUTION/AVAILABILITY CODES	
ALL INFORMATION CONTAINED HEREIN IS UNCLASSIFIED	
DATE 11/1/81 BY SP-6/STG/STG	
A	

UNCLASSIFIED

#### FOREWORD

The Infrared Information and Analysis (IRIA) Center is publishing this special Proceedings as part of its services to the infrared community. The one-day special meeting on the Physics of Detectors was sponsored by the Office of Naval Research.

This Proceedings contains papers presented in the Physics of Detectors meeting held at the Naval Training Device Center, Orlando, Florida on 15 March 1972. The meeting preceded the regular two-day meeting of the IRIS Detector Specialty Group, the Proceedings of which are published separately.

Authors were responsible for submitting camera copy of the individual manuscripts, and our thanks go to those authors who followed format requirements and met the publication deadline. Discussion sessions followed the oral presentation of these papers and were recorded on tape. Where possible, the tape has been transcribed, and the questions and answers are included after the reference sections of several of the papers.

The Willow Run Laboratories' number of this Proceedings is 24180-10-X.

Special thanks go to Prof. Henry Levinstein, Syracuse University, for his efforts in organizing the Physics of Detectors meeting.

UNCLASSIFIED

**UNCLASSIFIED**

**ABSTRACT**

**These Proceedings contain 13 papers presented at the unclassified Physics of Detectors Meeting held at The Naval Training Device Center, Orlando, Florida on 15 March 1972.**

**UNCLASSIFIED**

# UNCLASSIFIED

## CONTENTS

1. RECENT 1/f NOISE STUDIES, W. J. Moore (Naval Research Laboratory) . . . . .	1
2. RADIATION EFFECTS IN SEMICONDUCTORS USED AS INFRARED DETECTOR MATERIALS, J. A. Naber (Gulf Radiation Technology) . . .	13
3. BASIC DEVICE PROPERTIES IN THE LEAD CHALCOGENIDES, R. H. Rediker and J. N. Walpole (Massachusetts Institute of Technology) . . . . .	27
4. STRUCTURAL, CHEMICAL AND PHOTOELECTRONIC PROPERTIES OF LEAD SULFIDE FILMS; G. H. Blount, D. K. Smith, and R. T. Yamada (Santa Barbara Research Center) . . . . .	43
5. OPTICAL MEASUREMENTS ON PbSnTe, A. Lockwood and H. Levinstein, (Syracuse University) . . . . .	57
6. AUGER SPECTROMETER SURFACE STUDIES OF InSb AFTER DETECTOR FABRICATION PROCEDURES, R. E. Longshore (Army Night Vision Laboratory) . . . . .	73
7. RESULTS OF A STUDY OF THE INTERACTION BETWEEN LITHIUM AND SEVERAL DEEP ACCEPTOR IMPURITIES IN GERMANIUM, P. LoVecchio, K. Riley, and H. Levinstein (Syracuse University) . . . . .	83
8. RECOMBINATION CROSS-SECTION FOR HOLES IN Ge:Hg AND ELECTRONS IN N-TYPE Si, P. Norton, T. Braggins, and H. Levinstein (Syracuse University) . . . . .	93
9. PLZT AND SBN PYROELECTRIC DETECTORS, S. T. Liu and O. N. Tufté (Honeywell Corporate Research Center) . . . . .	101
10. POLYMERIC PYROELECTRIC DETECTOR, J. Cohen, C. F. Vezzetti, and S. Edelman (National Bureau of Standards) . . . . .	113
11. IMPROVED IRQC PERFORMANCE OF CdF <sub>2</sub> :Er <sup>3+</sup> BY GENERATION OF C <sub>2v</sub> AND C <sub>3v</sub> LOCAL SITE SYMMETRY, N. E. Byer, T. C. Ensign, and W. M. Mularie (Martin Marietta Corporation) . . . . .	119
12. DETECTION UNCERTAINTY, S. R. Borrello (Texas Instruments Incorporated) . . . . .	129
13. PREPARATION OF (Hg,Cd)Te BY A NEW HIGH PRESSURE FURNACE TECHNIQUE, J. Steininger, J. F. Butler, and J. B. Sohn (Arthur D. Little, Incorporated) . . . . .	135

Reverse page blank



# UNCLASSIFIED

.... This paper is UNCLASSIFIED

## RECENT 1/f NOISE STUDIES (U) (Unclassified)

W. J. Moore  
Naval Research Laboratory  
Washington, D. C. 20390

### 1. INTRODUCTION

(U) For the past several years there has been an increase in both experimental and theoretical interest in "1/f" noise. This has come about for several reasons. Some of these reasons are: (1) 1/f noise is almost universal in that it appears in most active circuit elements and in some that are usually considered passive. (2) There is a singularity in the magnitude of the noise as the frequency goes to zero. (3) The standard theoretical treatment of 1/f noise requires the presence of surface states which provide a range of trapping times; a situation which is probably not as universal as is the noise. Both experiment and theory have produced interesting and, in some cases, unexpected results.

### 2. STATISTICAL TECHNIQUE

(U) Digital techniques of waveform analysis have been used to measure the statistical parameters of the random noise. These digital techniques have been used to study a variety of devices including infrared detectors, diodes, and carbon resistors.

(U) These techniques measure the amplitude probability density,  $P(x)$ , and its moments. These measurements provide information on the statistics of the noise which complements the usual power spectrum determinations. The probability density is the probability that the noise amplitude takes a value between  $x$  and  $x + dx$ . The distribution can be measured using either analog or digital techniques but essentially requires that the waveform be sampled using one or more "windows", each of which sample one particular amplitude.

(U) If the distribution is "normal" (as appears to be the case for 1/f noise) then  $P(x)$  will vary as

$$P(x) = (1/\sigma\sqrt{2\pi})\exp[-x^2/2\sigma^2].$$

The parameter  $\sigma$  is the standard deviation and is a measure of the width of the distribution.

(U) Once the amplitude probability density is determined the moments of the distribution can be calculated. The moments of concern here are the mean, and the second, third, and fourth moments about the mean. These are defined as follows [1]:

$$\text{mean} = m = \int_{-\infty}^{\infty} x P(x) dx.$$

## UNCLASSIFIED

$$\text{Second central moment} = \mu_2 = \int_{-\infty}^{\infty} (x-m)^2 P(x) dx.$$

The second central moment is called the variance and denoted by  $\sigma^2$ .

$$\text{Third central moment} = \mu_3 = \int_{-\infty}^{\infty} (x-m)^3 P(x) dx.$$

$$\text{Fourth central moment} = \mu_4 = \int_{-\infty}^{\infty} (x-m)^4 P(x) dx.$$

(U) Two normalized quantities, skewness and kurtosis are often calculated from these moments. Their definitions are:

$$\text{Skewness} = \mu_3/\sigma^3$$

and

$$\text{Kurtosis} = \mu_4/\sigma^4.$$

The values of skewness and kurtosis are a measure of the shape of the distribution of amplitudes. For a normal distribution they have the values zero and three, respectively.

(U) Some of the important recent results which have been reported in the literature are:

- (1) The relative noise power is inversely proportional to the total number of carriers in the sample [2]. That is,

$$\langle (\frac{\Delta v}{v})^2 \rangle = \langle (\frac{\Delta \sigma}{\sigma})^2 \rangle = CN_{\text{tot}}^{-1} \frac{\Delta f}{f}.$$

Where  $N_{\text{tot}}$  = total number of carriers in the sample.

- (2)  $P(x)$  is normally distributed [3,4].
- (3) The measured variance is not constant, that is, when the measurement is repeated the value is different.
- (4) The distribution of variances, i.e. the probability density for the variances, is often skewed [3,5].

(U) In the present paper, we report on measurements designed to verify the results, (2), (3), (4) for typical elements exhibiting  $1/f$  noise. Our results cast doubt on properties (3) and (4) as fundamental to  $1/f$  noise. However we suggest possible sources not associated with  $1/f$  noise which may account for these apparent properties.

(U) A block diagram of the equipment used for these measurements is shown in Fig. 1. The pure analog approach includes the usual frequency spectrum analysis with a wave analyzer and includes the measurement of amplitude probability distributions for which a variety of analog devices are available. The digital approach can be either the specialized probability density determinations with a pulse height analyzer or full digital analysis in which each sample is recorded in real time on digital magnetic tape for later computer analysis. This last approach is the most versatile but also the most complicated. The pulse height

# UNCLASSIFIED

analysis technique is the easiest and most reliable. Large quantities of data can be accumulated easily. All the results reported here were acquired in this way.

## 3. RESULTS

(U) Typical amplitude probability densities taken using the pulse height analysis technique are shown in Figs. 2 and 3. In Fig. 2 the distribution is that of  $1/f$  noise from a slightly overbiased  $Hg_{1-x}Cd_xTe$  detector. The distribution is very nearly normal as can be seen from the values of skewness and kurtosis which are 0.003 and 2.99 respectively.

(U) The data of Fig. 3 is from a selected carbon resistor. This is also a nearly normal distribution, having a skewness of 0.009 and a kurtosis of 2.97. Also shown is the zero current measurement which indicates the magnitude of the other noise sources present.

(U) Two sources of error can easily modify data of this type. One is a systematic problem which occurs when there is no low frequency cutoff in the amplifying system. The second is the possible presence of noise transients which are not characteristic of "pure"  $1/f$  noise. These will be discussed in more detail.

(U) If dc coupled electronics is used there will be very low frequency components present. As a result, any measurement made in a finite amount of time and then repeated will result in a fluctuation in the measured quantity. All Fourier components with periods shorter than the sampling time will be properly averaged. Those components with longer periods will not be properly averaged and will produce a drift of the waveform during the measurement and consequently a change in the variance. A minimum variance will exist and be determined by the high frequency components. No maximum variance will exist, particularly when there is a large amount of low frequency noise. A skewed variance distribution will result. When the very low frequency noise is eliminated by a high pass filter this problem is not present.

(U) An example of the second source of error is shown in Fig. 4. This is an oscilloscope trace of noise from a carbon resistor of unknown manufacture. The bias is well within the power rating of the device. We have also seen similar noise in lead-sulphide detectors. The noise shown resembles the well known operational amplifier "popcorn" noise. It appears that the conductivity of the resistor has changed by a discrete amount for a short time and then returned to normal. Such noise pulses appear to be random and are a function of the bias across the device to the extent that a change in the bias usually changes the pulse repetition rate. These changes in conductivity appear to be superimposed on a normal  $1/f$  noise trace.

(U) The following model provides insight into the effect of this noise on the moments. Assume that all pulses have the same amplitude,  $a$ , probability,  $p$ , and are superimposed on a normal distribution given by

$$P_1(x) = (1/\sigma\sqrt{2\pi})\exp[-x^2/2\sigma^2].$$

## UNCLASSIFIED

The overall probability of having a value  $x$  then is composed of two parts:

(1) The probability of having the value  $x$  and no pulse, and (2) the probability of having the value  $x$  with an assist from a pulse of amplitude  $a$ . The total probability is given by

$$P(x) = [(1-p)/\sigma\sqrt{2\pi}]\exp[-x^2/2\sigma^2] + [p/\sigma\sqrt{2\pi}]\exp[-(x-a)^2/2\sigma^2].$$

From this probability density the central moments, and an approximate skewness-kurtosis relationship can be calculated. They are:

$$\mu_2 = \sigma^2 + a^2 p(1-p) \approx \sigma^2 + a^2 p$$

$$\mu_3 = a^3 p(1-p)(1-2p) \approx a^3 p$$

$$\begin{aligned} \mu_4 &= 3\sigma^4 + 6\sigma^2 a^2 p(1-p) + a^4 p(1-p)(1-3p+3p^2) \\ &\approx 3\sigma^4 + (6\sigma^2 a^2 + a^4)p \end{aligned}$$

$$\frac{\text{Kurtosis} - 3}{\text{Skewness}^2} \approx \frac{a}{\sigma} + F(a, \sigma)p \equiv A + Bp$$

(U) Two points should be made about these results. If the probability of pulsing is not the same for every run (i.e. if the number of pulses is not constant for every run) the variance  $\mu_2$  will fluctuate with a minimum value of  $\sigma^2$ . This leads to a skewed variance distribution. The second observation is that runs which exhibit a large skewness will also have a large kurtosis.

(U) A skewness vs kurtosis plot for an off-the-shelf carbon resistor is given in Fig. 5. It can be seen that there is a clear indication of a relationship such as that predicted with the ratio  $a/\sigma$  about ten (the term  $Bp$  is small). Both positive and negative skewness is observed and indeed the pulses have been observed to have both positive and negative sign. One can conclude that runs fitting the upper curve have pulses which are predominantly positive whereas those fitting the lower curve have predominantly negative pulses. It also suggests that such measurements might be a way to screen active devices for "popcorn" noise.

(U) During the course of repeatedly determining the probability density there was a slow drift in bias current. In Fig. 6 the measured variance is plotted as a function of bias current. This figure indicates that the usual  $I^2$  dependence is present.

(U) Another point of interest is that large fluctuations in the variance are not apparent when measurements are made using a wave analyzer. This is the result of ignoring transients which the operator can recognize as of a transient nature because of the short integration times used (a few seconds or less). Such transients are not ignored when the sampling technique is used.

(U) The results of variance measurements on two different off-the-shelf carbon resistors are given in Fig. 7. In part (A) the number of noise pulses was

## UNCLASSIFIED

small (in some cases records were discarded when large numbers of pulses were present). The variance and the inverse normalized variance of variance (that is  $\langle \sigma^2 \rangle^2 / \mu_2(\sigma^2)$ ) is about 13 in agreement with Brophy [3,5]. The distribution is only slightly skewed. In part (B) a large number of pulses occurred. The variance is large and the distribution is skewed. The distribution is very wide.

(U) A plot of similar data for a carefully chosen carbon resistor is given in Fig. 8. The variance is a factor of 20 smaller than that for the off-the-shelf resistors. The inverse normalized variance of variances is quite high indicating a very tight distribution (the tightest yet measured for  $1/f$  noise) and the variance distribution is not skewed.

(U) These experimental results show that some devices, including carbon resistors, produce  $1/f$  noise which behaves statistically very much like any other noise. The statistical peculiarities, particular the skewed variance distributions, which have been observed are not characteristic of all  $1/f$  noise.

(U) As a final comment, it is interesting to note that recent theoretical attempts to understand  $1/f$  noise [6,7] have focussed on the universality of the noise rather than specific sources of the noise. Common to these approaches is the idea that  $1/f$  noise is essentially a turbulent phenomena in electric current flow. The nature of the turbulence does not change from element to element, but only the source of the turbulence varies. The turbulence is shown to lead to a  $1/f$  spectral density.

### REFERENCES

1. See for example: C. E. Weatherburn, A First Course in Mathematical Statistics, Cambridge University Press, New York, 1968.
2. F. N. Hooge, Phys. Letters 29A, 139 (1969).
3. J. J. Brophy, Phys. Rev. 160, 827 (1968).
4. F. N. Hooge and A. M. H. Hoppenbrouwers, Physica 42, 331 (1969).
5. J. J. Brophy, J. Appl. Phys. 41, 2913 (1970).
6. P. H. Handel, Phys. Rev. A3, 2066 (1971).
7. S. Teitler and M. F. M. Osborne, Phys. Rev. Lett. 27, 912 (1971).

UNCLASSIFIED

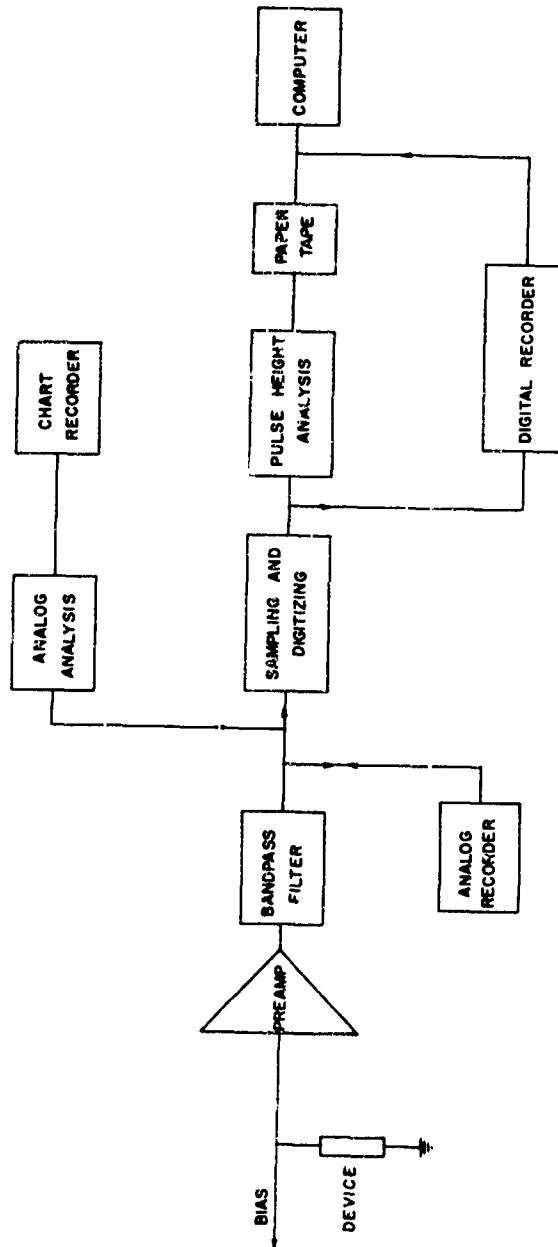


Figure 1. Block diagram of equipment used for statistical studies of noise.

UNCLASSIFIED

UNCLASSIFIED

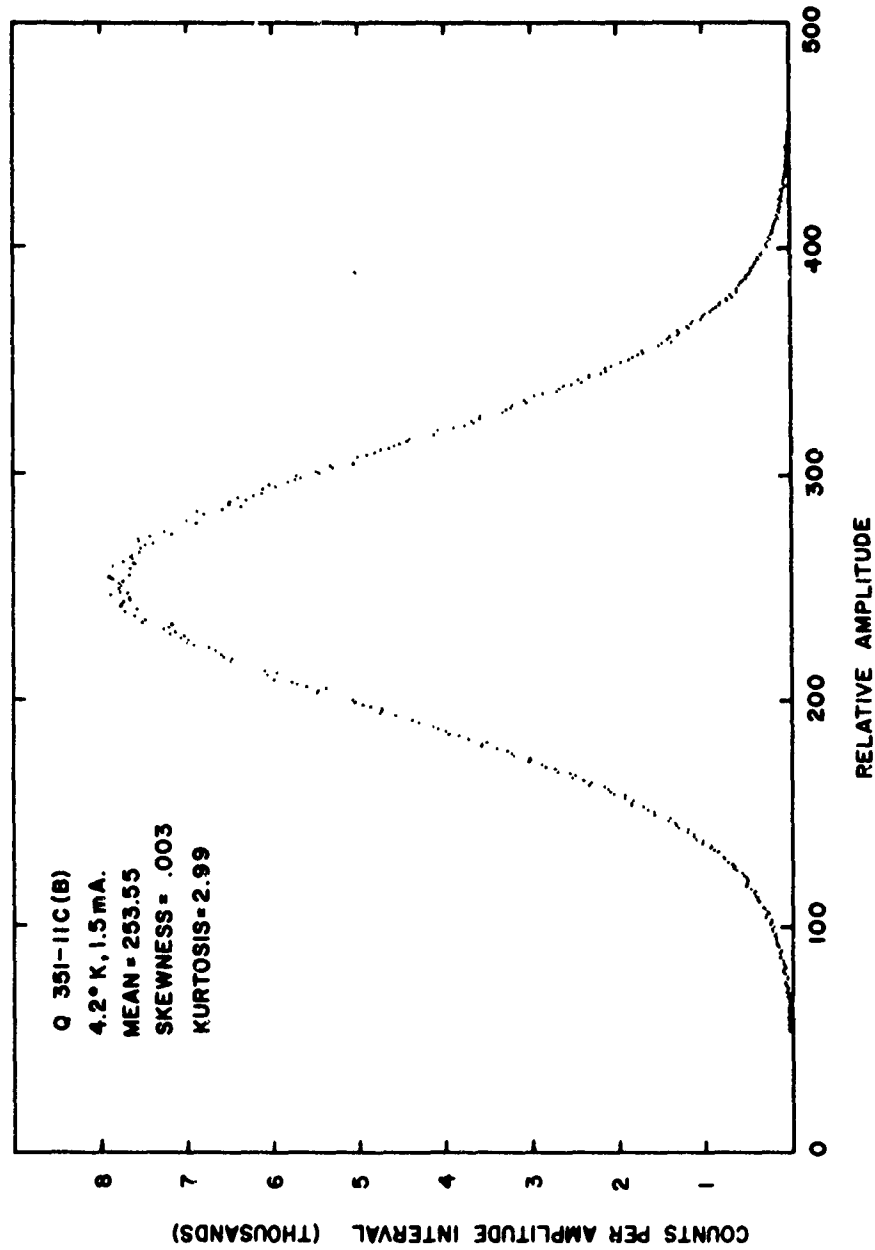


Figure 2. Amplitude probability density for 1/f noise from a  $\text{Hg}_{1-x}\text{Cd}_x\text{Te}$  detector.

UNCLASSIFIED

UNCLASSIFIED

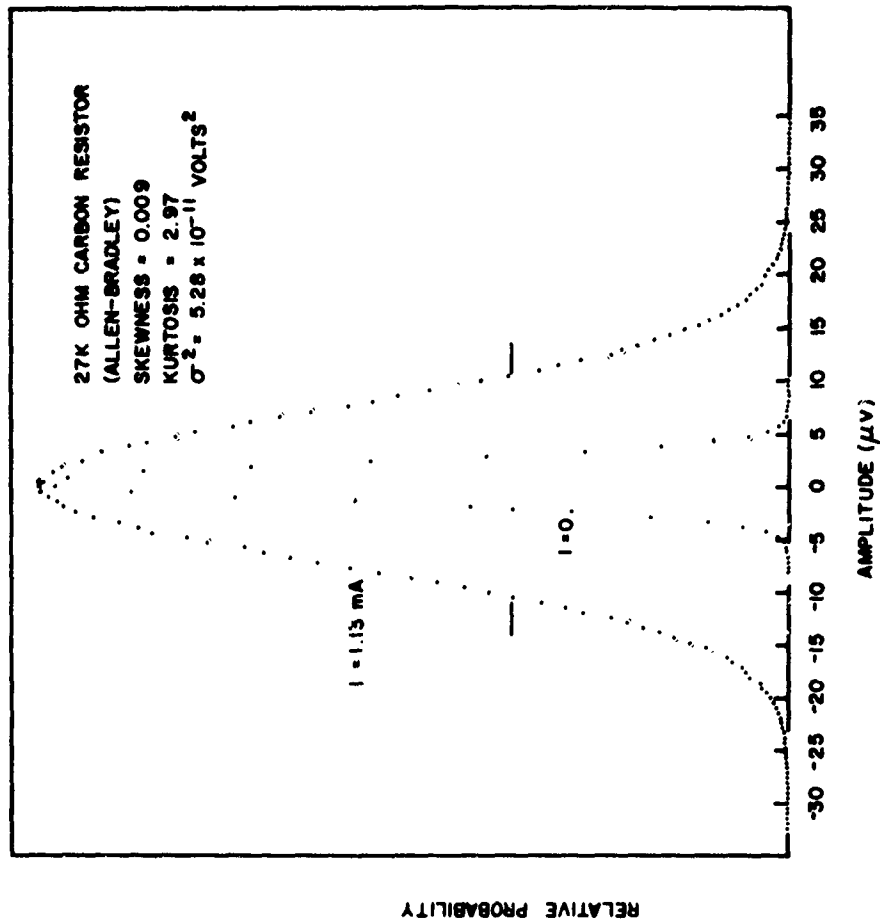


Figure 3. Amplitude probability density for a carefully selected low noise carbon resistor.

UNCLASSIFIED



UNCLASSIFIED

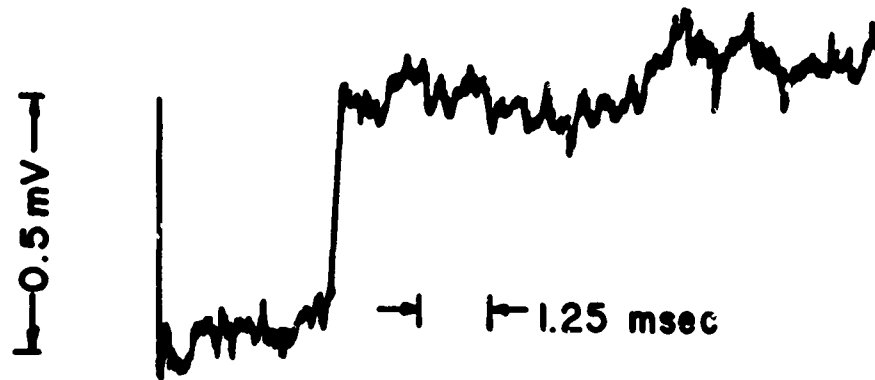


Figure 4. Typical pulse noise from an off-the-shelf carbon resistor under bias.

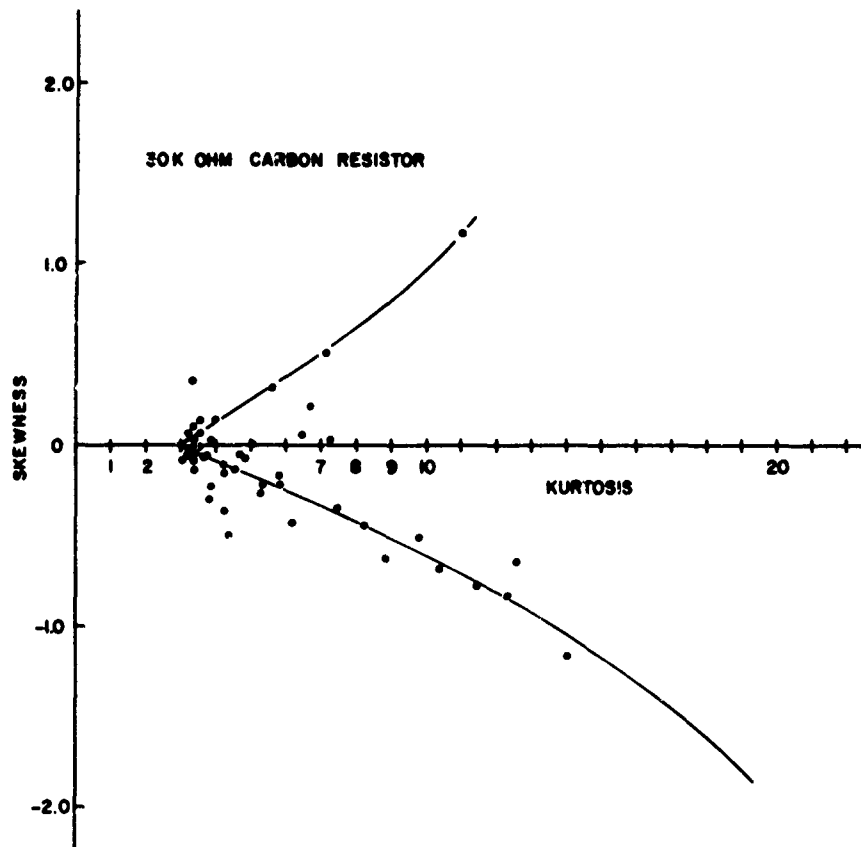


Figure 5. Skewness-kurtosis relationship for an off-the-shelf carbon resistor.

UNCLASSIFIED

UNCLASSIFIED

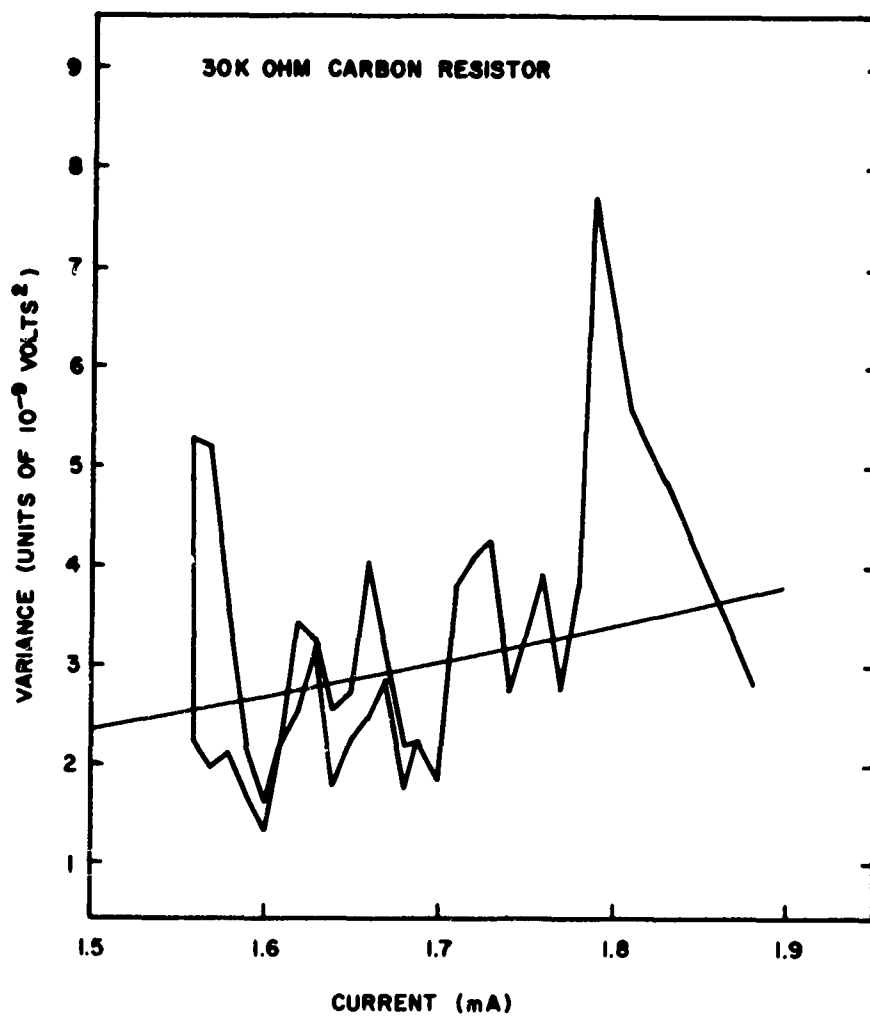


Figure 6. Measured variance as a function of bias current. The smooth line indicates a pure  $I^2$  dependence.

UNCLASSIFIED

UNCLASSIFIED

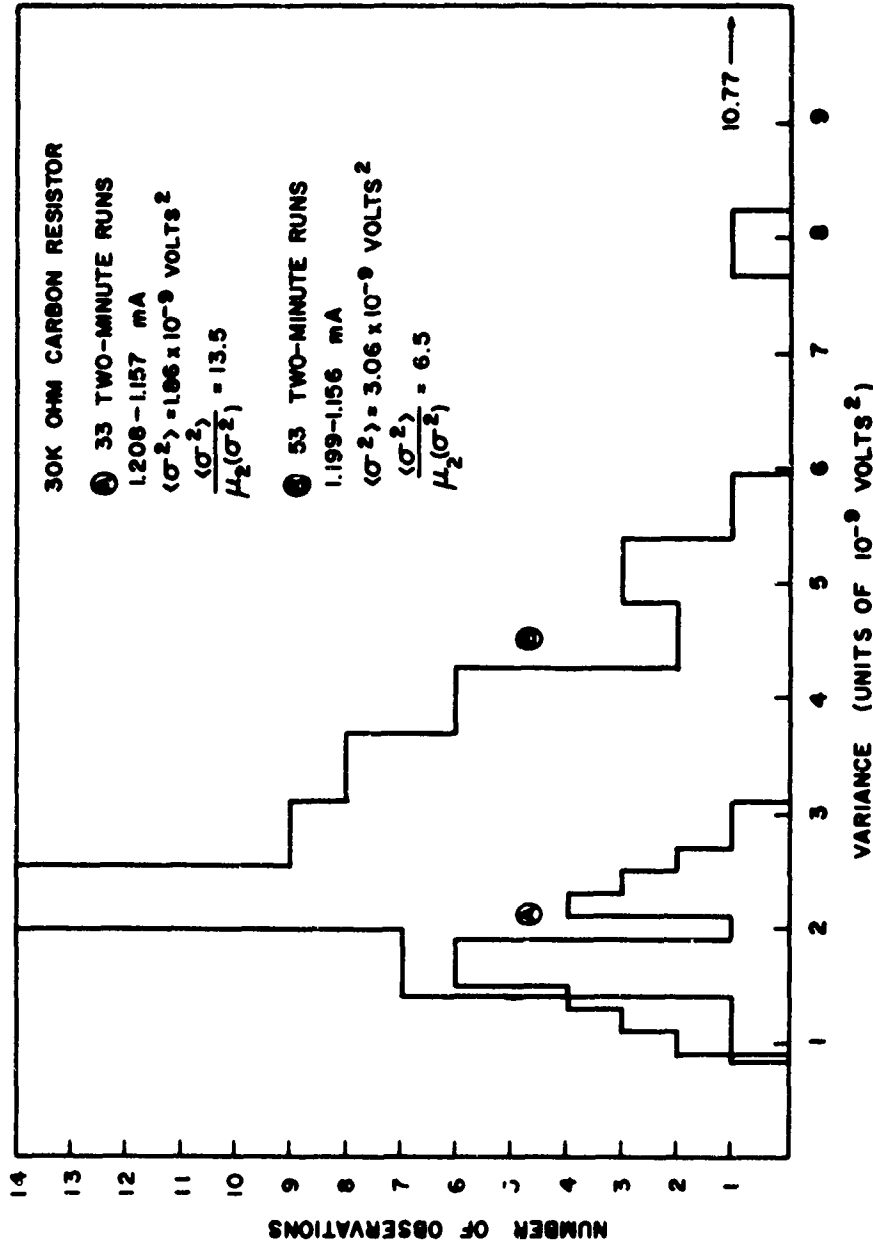


Figure 7. Distribution of variances for two-minute measurements of  $1/f$  noise from biased off-the-shelf carbon resistors. One point at  $10.77 \times 10^{-9}$  volts<sup>2</sup> is not shown.

UNCLASSIFIED

UNCLASSIFIED

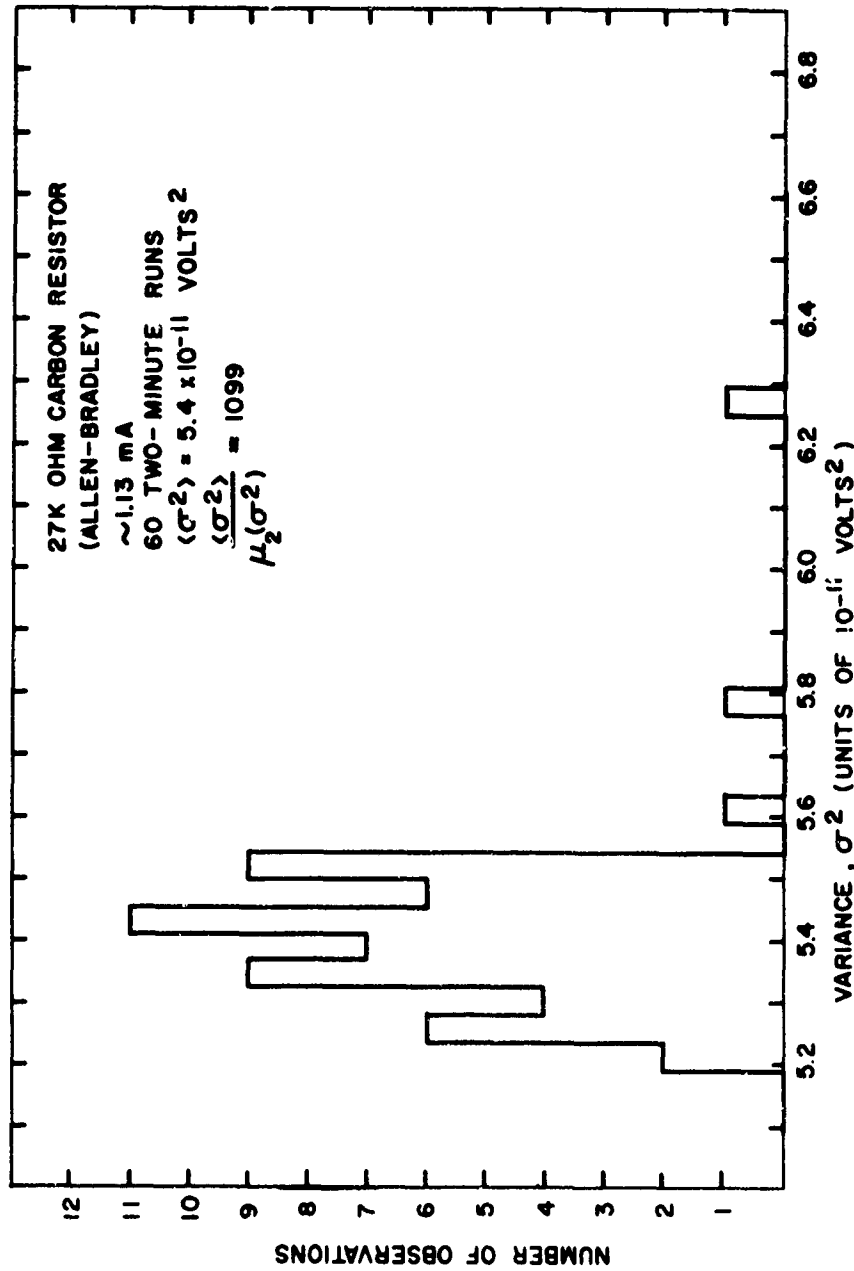


Figure 8. Distribution of variances for a carefully chosen low noise carbon resistor. This distribution is very tight and is not skewed.

UNCLASSIFIED

# UNCLASSIFIED

.... This paper is UNCLASSIFIED

## RADIATION EFFECTS IN SEMICONDUCTORS USED AS INFRARED DETECTOR MATERIALS

(Unclassified)

J. A. Naber  
Gulf Radiation Technology  
San Diego, California

### ABSTRACT

The introduction and annealing of irradiation produced permanent displacement damage effects in semiconductor materials will alter the output of infrared detectors. The introduction of the damage and its annealing depends on the semiconductor material, irradiating particle, semiconductor impurities, temperature and injection level. A knowledge of both the principles of operation of the infrared detector and the effects of radiation and annealing on the basic properties for operation of the detector, permits one to predict the changes in the detector output as a function of nuclear particle irradiation and annealing.

### 1. INTRODUCTION

When nuclear particles interact with semiconductors, changes are produced in the properties of these materials. These changes can be divided into two categories; namely permanent displacement effects and ionization effects. When lattice atoms are displaced from their lattice site, permanent displacement effects are produced. These effects are usually stable at the temperature of irradiation. However, at higher temperatures the effects are not stable. The disappearance of the permanent damage is known as annealing. Ionization effects are the manifestation of free electrons produced by the radiation interacting with atomic electrons. These ionization effects are usually transient phenomena and are present on a time scale up to seconds.

Over the past few years, studies of permanent damage caused by displacement effects have shown that some of the properties that can be altered by radiation include lattice parameter, stored energy, mobility, electrical conductivity, carrier lifetime, electron paramagnetic resonance, optical absorption, thermal conductivity, etc.

A knowledge of how all the above parameters are affected by irradiation is of interest when a microscopic description of the damage mechanisms in semiconductors is desired. However, radiation effects information is mainly needed to help predict the response of semiconductor devices. When this is the case, only selected radiation effects information on the properties that affect the device output characteristics are necessary.

This paper considers those permanent displacement effects in semiconductor materials that are of interest as infrared detectors. Gamma, electron, neutron, and proton irradiation of intrinsic photoconductive detectors are of primary interest. These intrinsic detectors include Si, Ge, GaAs, InP, ZnS, ZnSe, CdS, and CdSe with response in the 0.3- to 2-micron region.

## UNCLASSIFIED

### 2. PRINCIPLES OF OPERATION - INFRARED DETECTORS

In the operation of photoconductive infrared detectors, the output characteristics of primary interest are the signal voltage ( $V_S$ ), noise voltage ( $V_n$ ), and response time. In a simplified analysis, (1,2) the magnitude of the signal and generation-recombination noise voltages for electron dominated photoconductors can be expressed as:

$$V_S = eR_L Q_S A t \sigma \left( \frac{E_H}{h\nu} \right) \tau N \quad (1)$$

and

$$V_n = \frac{2 E R_L e}{h^2} \left[ t (\Delta f) \sigma A Q_B \right]^{\frac{1}{2}} \mu \tau N^{\frac{1}{2}} \quad (2)$$

where  $e$  is electronic charge,  $R_L$  is the load resistor,  $Q_S$  and  $Q_B$  are the signal and background photon fluxes, respectively.  $A$  is the illuminated detector area,  $t$  and  $h$  are the detector thickness and length, respectively.  $\sigma$  is the cross section for interaction between the incident photons and impurity center,  $E$  is constant supply voltage,  $\Delta f$  is bandwidth,  $\mu$  is carrier mobility,  $\tau$  is carrier lifetime, and  $N$  is the density of infrared active centers.

The photoconductive detector's response time is dependent on the carrier lifetime as illustrated in Fig. 1. Both the rise and fall time depends on the carrier lifetime.

The radiation-sensitive parameters in the output equations and response time are the carrier lifetime, mobility and density of infrared active centers. Each of these parameters is, to varying degrees, sensitive to nuclear particle radiation. Therefore, these are the electrical properties of major interest in studying the radiation effects in semiconductors used as infrared detectors.

### 3. RADIATION-SENSITIVE PROPERTIES

A description of the radiation sensitivity of the pertinent properties should not only include the introduction of damage but also the annealing. The description and magnitude of the introduction and annealing of damage depends on the semiconductor material, the irradiating particle, impurities, temperature, and injection level.

#### 3.1 INTRODUCTION TO DAMAGE

Irradiating semiconductor materials with gamma rays or low energy ( $\sim 1$  MeV) electrons mainly produces one type of microscopic damage and irradiation with neutrons or protons produces basically a different type of microscopic damage in a semiconductor. The damage caused by exposure to gamma rays or electrons is similar and produces point defects or simple complexes. The point defects are vacancy and interstitials while complexes include divacancies and vacancy-impurity configurations. The damage produced by the neutrons and protons is mainly clustered defects. The difference between the gamma-ray and electron damage and the neutron and proton damage is due to the difference in energy transfer by the incident particles.

The point defects or simple complexes produce donor and acceptor states or energy levels in the energy gap of the semiconductor (Fig. 2). The defect's effectiveness in altering the properties of the semiconductor depends on the defect's charge state, i.e., the Fermi level position relative to the defect's energy level position. These defects can act as additional recombination centers, thus decreasing the carrier lifetime. The defects can also act as carrier removal sites by altering the density of infrared active centers, i.e., remove carrier from the conduction or valence bands or

## UNCLASSIFIED

change the occupation of impurity states in the energy gap. The defects can also act as scattering centers thereby decreasing carrier mobility.

In Fig. 3, the cluster type of damage is shown as a damaged region within the undamaged lattice.<sup>(3)</sup> The cluster is pictured<sup>(4)</sup> as a group of displaced atoms with radius of  $10^3 \text{ \AA}$  and 50 displaced atoms. The interface between the damaged and undamaged regions forms a potential barrier that helps the damaged region act as a sink for carriers. This sink contains many recombination centers, or carrier removal sites. These clustered regions with large recombination rates will decrease the carriers' average lifetime in the semiconductor. The large density of defects in the clustered region will decrease the carrier concentration within the cluster. When the nondamaged and damaged carrier concentration's regions are integrated over the crystal, the average carrier concentration of the semiconductor will have decreased. In intrinsic detectors, the presence of the cluster will increase the number of infrared active centers by decreasing the carrier concentration. The cluster region with its potential barrier is an ideal scattering center, thus decreasing the mobility.

At low fluences, the changes in the electrical properties can be described in a simple analytical form. After a particle fluence,  $\phi$ , the average lifetime,  $\tau$ , can be expressed as

$$\frac{1}{\tau} = \frac{1}{\tau_0} + K\phi \quad (3)$$

where  $\tau_0$  is the initial lifetime and  $K$  is the degradation constant. Figure 4 shows the degradation of the lifetime for silicon when irradiated with electrons and neutrons, respectively. In a similar manner, the initial carrier concentration ( $n_0$ ) will decrease upon irradiation according to the relationship

$$n = n_0 - \frac{dn}{d\phi} \phi \quad (4)$$

where  $\phi$  is the fluence and  $dn/d\phi$  is the carrier removal rate. For intrinsic detectors at photon energies slightly larger than the band gap, a decrease in carrier concentration will produce an increase in the number of active infrared centers. This increase will be of the same form as Eq. 4. Figure 5 shows this effect as a function of electron and neutron fluences. In extrinsic detectors, the introduction of donor or acceptor states can act as counter doping for the infrared active centers. Depending on the type of center introduced, the density of infrared active centers could either increase or decrease with the linear form of Eq. 4. Finally, the decrease in mobility as a function of mobility can be expressed as

$$\frac{1}{\mu} = \frac{1}{\mu_0} + Z_S\phi \quad (5)$$

where  $Z_S$  is the introduction rate of scattering centers.

In both Figs. 4 and 5 note that the degradation is linear as suggested by Eqs. 4 and 5. Also note that the degradation constant and carrier removal rate is a function of irradiating particle. The figures show that exposure to neutrons is much more damaging than exposure to gamma rays.

The carrier lifetime, carrier concentration, and mobility do not have the same sensitivity to radiation. In a typical semiconductor, carrier lifetime is the most sensitive to radiation while the carrier concentration and mobility are less sensitive. Silicon with a lifetime of  $10^{-6}$  sec and

## UNCLASSIFIED

a resistivity of 10 ohm-cm contains approximately  $10^{13}$  to  $10^{14}$   $\text{cm}^{-3}$  recombination centers and has a carrier concentration of  $10^{15}$   $\text{cm}^{-3}$ . When  $10^{12}$  to  $10^{13}$   $\text{cm}^{-3}$  defects (recombination centers) have been introduced by the irradiation, the lifetime will start to decrease (10% change). The carrier concentration will be altered by 10% when  $10^{14}$   $\text{cm}^{-3}$  carrier removal sites have been introduced. The sensitivity of the mobility depends on the temperature of interest; however,  $10^{14}$   $\text{cm}^{-3}$  scattering centers will alter the mobility in the ionized impurity scattering region. In the lattice scattering temperature region, scattering center densities in excess of  $10^{14}$   $\text{cm}^{-3}$  must be introduced before the mobility will be altered. Since carrier lifetime is most sensitive to nuclear particle irradiation, the initial detector output parameter change will be due to changes in the carrier lifetime followed by changes in carrier concentration and mobility.

The number of defects depends on the type of irradiating particle and the fluence. Using various experimental data<sup>(9)</sup> and calculations<sup>(10)</sup> based on the energy going into non-ionizing lattice energy in silicon, it can be shown that for 1-MeV electron irradiations approximately 0.1 defect/ $\text{cm}^3$  is introduced per incident electron/ $\text{cm}^2$ . For neutrons, the introduction rate is about 5 defects/ $\text{cm}^3$  per incident neutron/ $\text{cm}^2$ . Gamma rays are less effective than either electrons or neutrons in producing damage. For each incident gamma/ $\text{cm}^2$ , 0.001 defects/ $\text{cm}^3$  are introduced. These defect introduction rates are consistent with the microscopic nature of the damage produced and their production by gamma rays, electrons, and neutrons. For equal fluences, the neutrons are the most damaging; electrons are less damaging; and gamma rays are the least damaging. For the above semiconductor example to degrade the carrier lifetime with  $10^{12}$  defects/ $\text{cm}^3$ , a gamma fluence of  $10^{15}$  gammas/ $\text{cm}^2$  is necessary. Likewise,  $10^{13}$  electrons/ $\text{cm}^2$  or  $2 \times 10^{11}$  neutrons/ $\text{cm}^2$  will produce the same effects. This relative effectiveness of gamma rays and neutrons in producing damage is evident on Figs. 4 and 5.

Two noteworthy examples of the impurity and injection level dependence of damage introduction are the impurity independence of neutron damage and the injection level dependence of the carrier lifetime degradation constant.

Neutron produced lifetime degradation<sup>(11)</sup> is independent of the type and concentration of impurities. This is consistent with the cluster nature of neutron damage where the density of defects in the cluster is much greater than any impurity concentration. On the other hand, the gamma and electron produced lifetime degradation<sup>(12)</sup> depends on the impurity type and concentration. This is also consistent with the point defect and simple complex nature of this damage.

The injection level dependence of the lifetime degradation constant<sup>(13)</sup> after neutron irradiation is clearly shown in Fig. 6. Note the order of magnitude change in the degradation constant as the injection level is altered by five orders of magnitude.

### 3.2 ANNEALING

After irradiation, the material parameters can be returned to their initial preirradiation values by either thermal or injection techniques. This result is termed "forward annealing". These same techniques can be used to cause the degradation to become more severe. This result is termed "reverse annealing". The annealing depends upon the method used, the type of material, type of irradiating particle, injection level, temperature, and impurities.

The annealing of point defect or simple complex damage is different from that of clustered damage. This means that the annealing of electron and gamma damage will differ from that of neutron or proton damage. The annealing is different in the temperature range over which it occurs and its kinetics. The point defects damage annealing (Fig. 7) usually occurs in a sharp stage while the



## UNCLASSIFIED

clustered damage anneals (Fig. 7) over a broad temperature range. The annealing of various radiation produced simple defects, stable at 273°K, have been studied. In silicon, the divacancy anneals at 550°K, the vacancy-phosphorous at 450°K, the vacancy-oxygen complex at 600°K.<sup>(14)</sup> Furthermore, point defect annealing usually occurs with first or second order kinetics while annealing kinetics for the clustered damage are quite complicated. This thermal annealing is due to the thermally-activated breakup of the complexes or clusters, or the thermally-activated diffusion of impurities or radiation-produced entities. The accompanying relaxation accounts for the annealing of the initially produced defects.

Besides thermal annealing, injection annealing<sup>(15)</sup> of defects is also possible. The mechanism for the injection annealing is accomplished by altering the charge state of the defect to a state in which it is more mobile than the stable damage condition. Figure 8 shows the injection isochronal annealing of the carrier concentration of p-Si after 300°K electron irradiation. This particular annealing is thought to be caused by altering the charge state of the vacancy to a state which is very mobile at 300°K.

It is evident that the damage introduced by irradiation can be thermally and sometimes injection annealed. For irradiations at 300°K, the damage can be thermally annealed at temperatures as low as 400°K. The possibility of annealing means that radiation produced changes in the carrier lifetime, carrier concentration and mobility can be completely removed. Elevated temperatures of 700°K may be necessary to return the material's properties to their preirradiation values.

#### 4. SUMMARY

Armed with a knowledge of the principles of operation of an infrared detector and the effects of irradiation and annealing on the pertinent properties for operation, it is possible to predict the response of infrared detectors to a nuclear particle environment. In general, it can be seen that upon irradiation the carrier lifetime, carrier concentration, and mobility will all decrease. Therefore, both the signal and noise voltages (g-r) will decrease. Since the response time depends on the carrier lifetime, as the damage is introduced (Fig. 1), the response time will decrease. These changes can possibly be annealed thermally and possibly by injection techniques and the detector can be returned to its initial performance characteristics.

#### REFERENCES

1. M. R. Holter, et al., "Fundamentals of Infrared Technology," 1962, MacMillan Company, New York.
2. P. Bratt, et al., Infrared Physics 1, 27 (1961).
3. B. R. Gossick, J. Appl. Phys. 30, 1214 (1959).
4. R. E. Leadon, IEEE Transactions on Nuclear Science, NS-17, 110, December 1970.
5. H. J. Stein, J. Appl. Phys. 37, 3382 (1966).
6. H. J. Stein, J. Appl. Phys. 39, 5283 (1968).
7. L. J. Cheng and J. Lori, Phys. Rev. 1, 1558 (1970).
8. J. W. Corbett, "Electron Radiation Damage in Semiconductors and Metals," Academic Press, New York (1966).
9. V. A. J. van Lint, "Mechanisms of Transient Radiation Effects," Gulf Radiation Technology Report GA-8810, August 28, 1968.

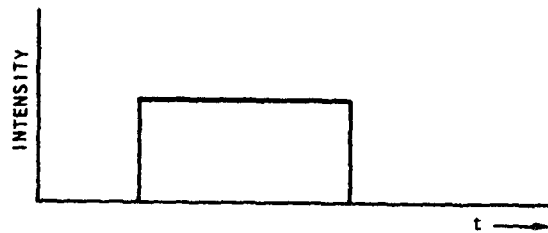
## UNCLASSIFIED

10. R. E. Leadon, J. A. Naber, and T. M. Flanagan, "Research on the Physics of Transient Radiation Effects," Gulf Radiation Technology Report GA-9334, April 1969.
11. H. J. Stein, Phys. Rev. **163**, 801 (1967).
12. L. C. Kimberly, et al., Phys. Rev. **B3**, 427 (1971).
13. J. W. Harrity, C. E. Mallon, and J. A. Naber, "Investigation of Short-Term Annealing with APFA-III," Gulf Radiation Technology Report GA-9384, November 1969.
14. G. D. Watkins, "Radiation Damage in Semiconductors," Seventh International Conference on the Physics of Semiconductors, p. 97, Academic Press, 1964.
15. J. L. Azarewicz, et al., "Research on the Physics of Transient Radiation Effects," Gulf Radiation Technology Report Gulf-RT-A10870, February 1972.

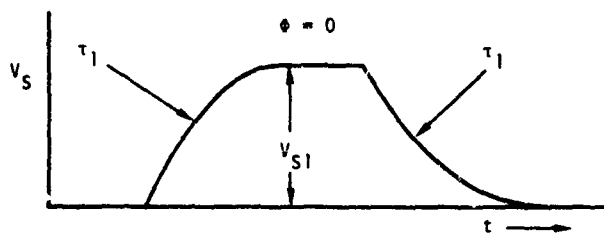
### QUESTION AND ANSWER SESSION

- Q. Are there not annealing steps below 80°K?
- A. Yes, if the damage is caused at, say 4°K, annealing can occur at 30°K and 60°K by injection annealing or irradiating with optical radiation.
- Q. What experimental techniques are used for establishing the effectiveness of the interaction between the radiation and the lattice?
- A. Primarily electron-spin resonance and EPR.

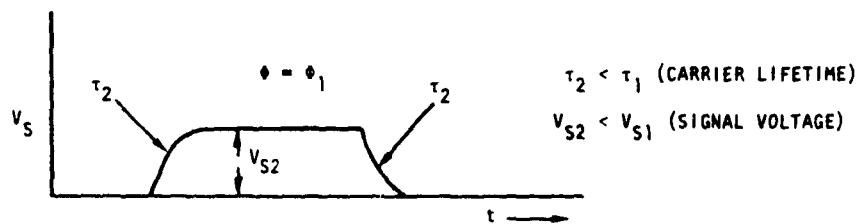
UNCLASSIFIED



A. INFRARED SIGNAL



B. RESPONSE PRIOR TO IRRADIATION



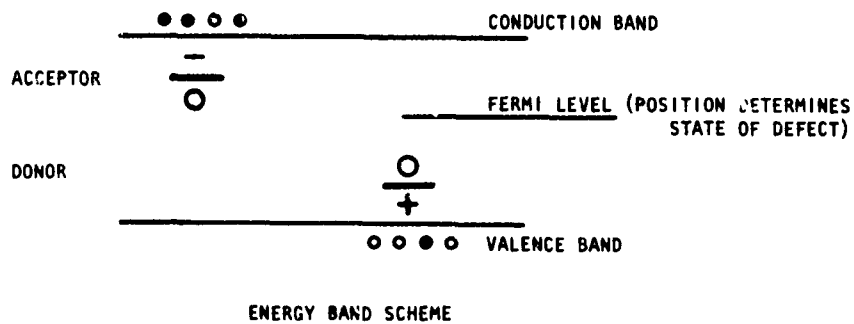
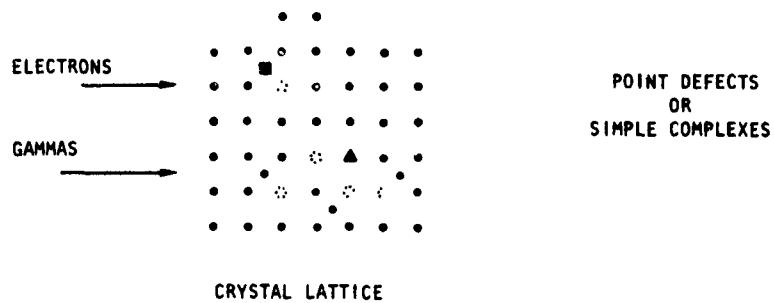
C. RESPONSE AFTER IRRADIATION

RT-00137

FIGURE 1. INFRARED DETECTOR RESPONSE TIME AND MAGNITUDE  
AFFECTED BY IRRADIATION.

UNCLASSIFIED

UNCLASSIFIED



RT-00138

FIGURE 2. GAMMA AND ELECTRON DISPLACEMENT DAMAGE MODEL.

UNCLASSIFIED

UNCLASSIFIED

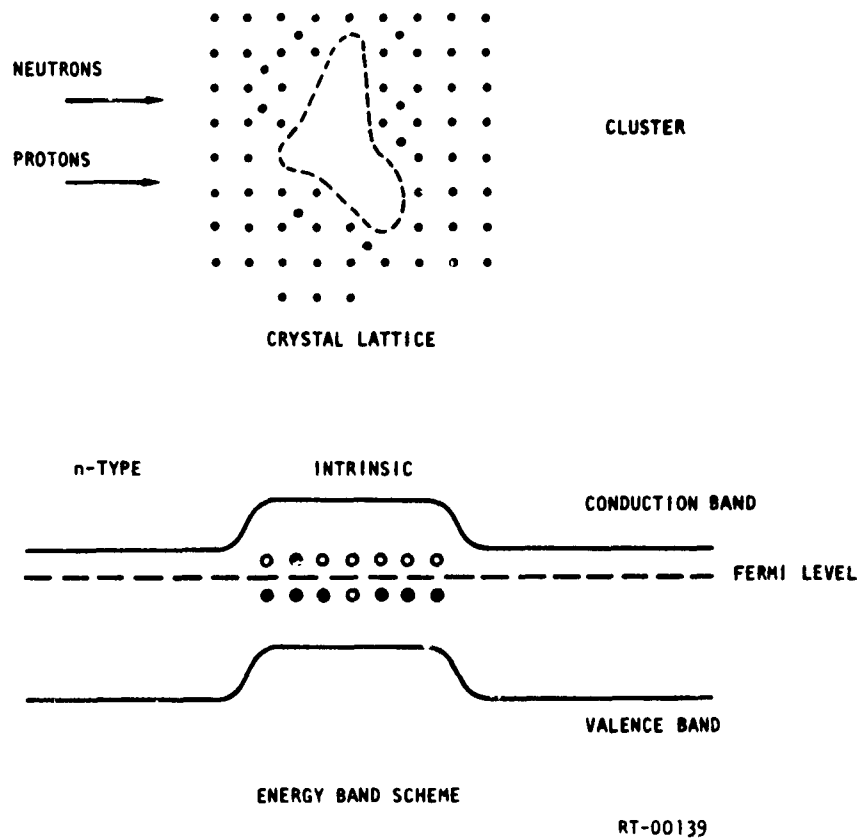


FIGURE 3. NEUTRON AND PROTON DISPLACEMENT DAMAGE MODEL.

UNCLASSIFIED

UNCLASSIFIED

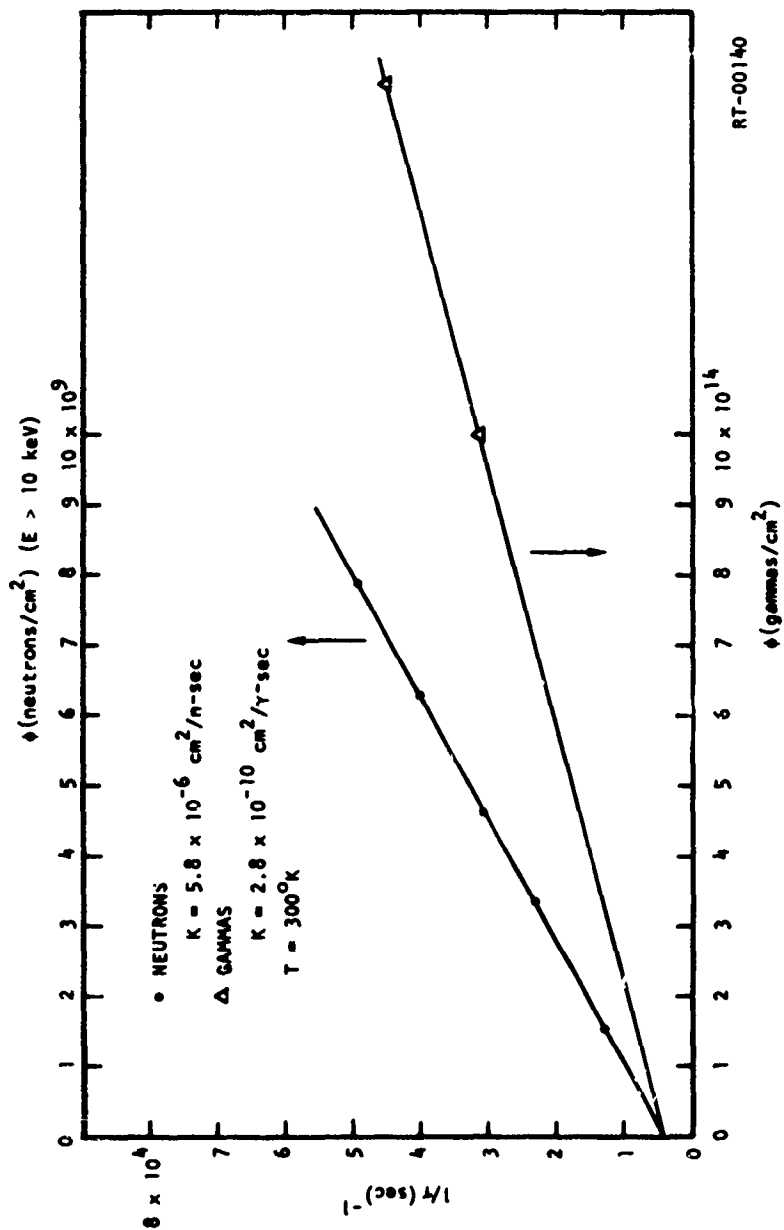


FIGURE 4. NEUTRON AND GAMMA DEGRADATION OF CARRIER LIFETIME IN 6-ohm-cm n-TYPE SILICON.

UNCLASSIFIED

UNCLASSIFIED

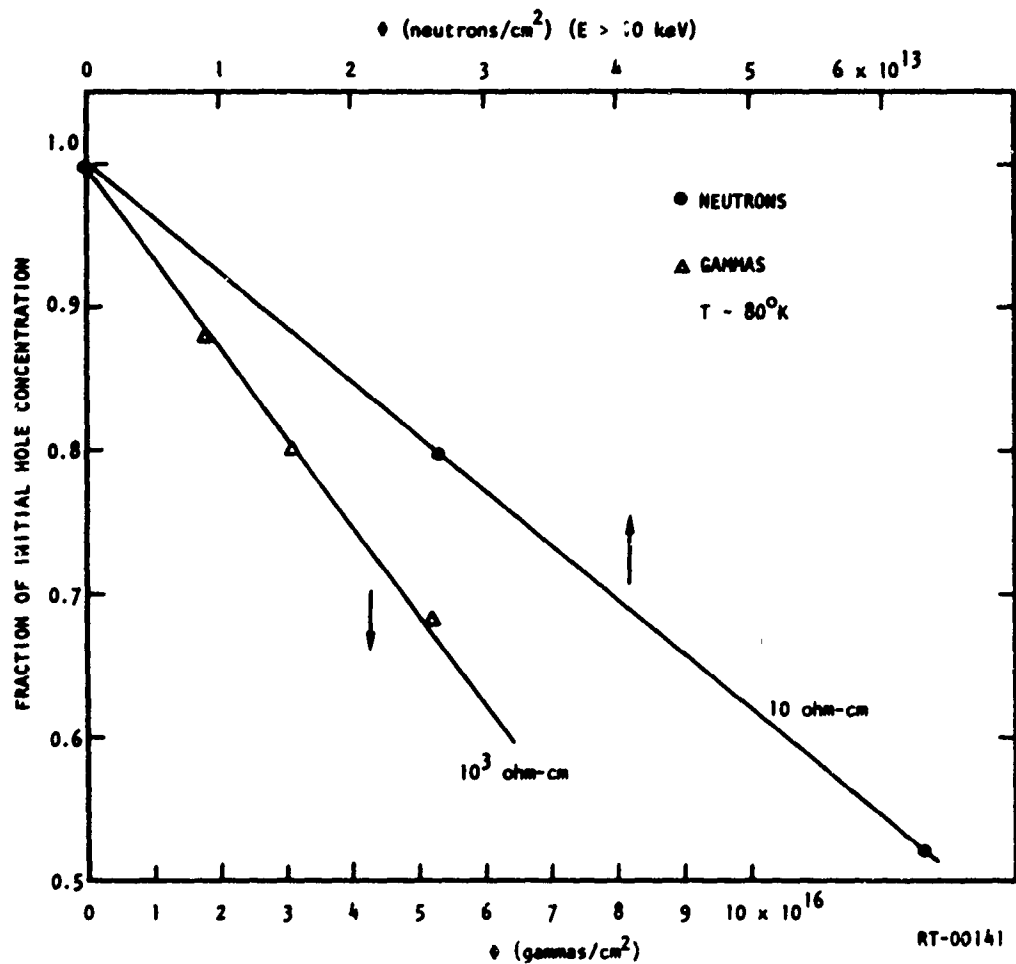


FIGURE 5. NEUTRON AND GAMMA DEGRADATION OF CARRIER CONCENTRATION IN p-TYPE SILICON.

UNCLASSIFIED

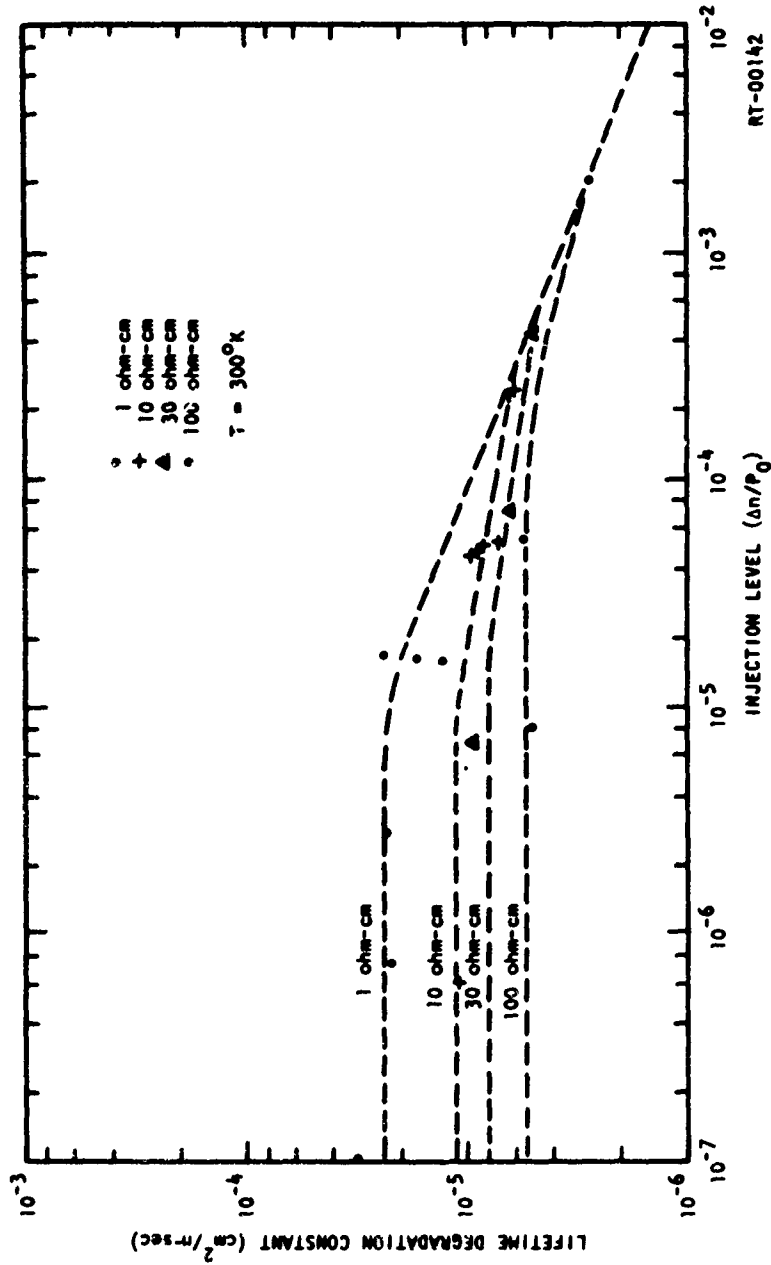


FIGURE 6. LIFETIME DEGRADATION CONSTANT AS A FUNCTION OF INJECTION LEVEL AFTER NEUTRON IRRADIATION OF p-TYPE SILICON.

UNCLASSIFIED



UNCLASSIFIED

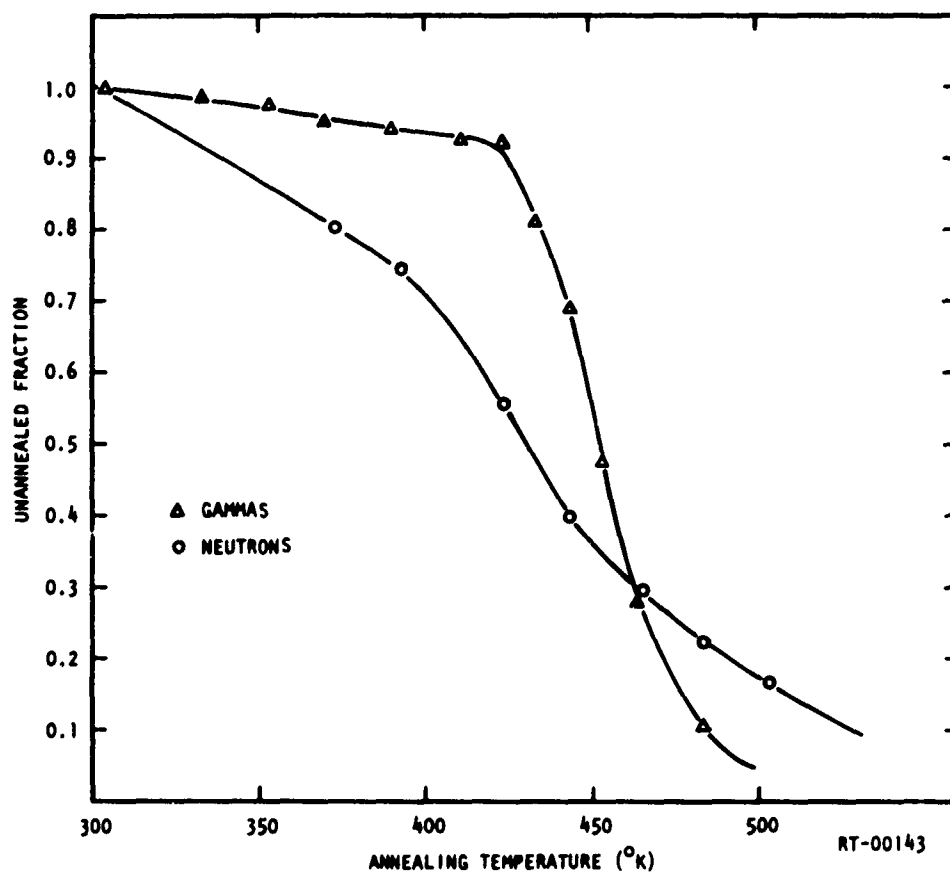


FIGURE 7. ISOCHRONAL ANNEAL OF LIFETIME OF n-TYPE SILICON AFTER GAMMA AND NEUTRON IRRADIATION AT 300°K.

UNCLASSIFIED

UNCLASSIFIED

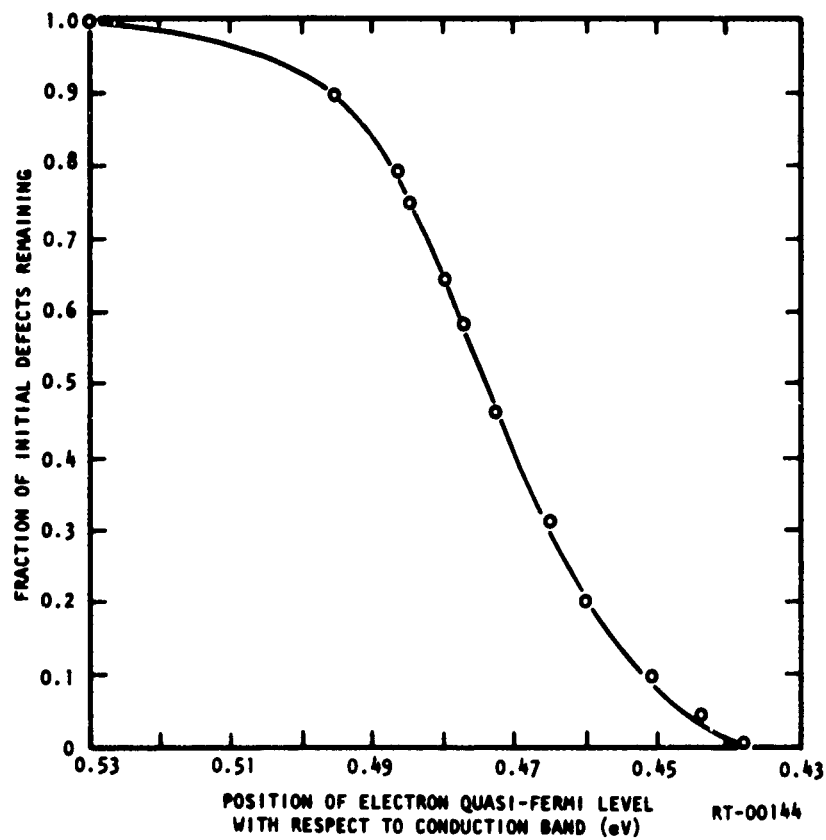


FIGURE 8. ISOCHRONAL ANNEAL AT 300°K, BY EXCESS CARRIER INJECTION, OF CARRIER REMOVAL SITES PRODUCED IN  $10^{-4}$ -ohm-cm p-TYPE SILICON BY A PULSED 30-MeV ELECTRON IRRADIATION.

UNCLASSIFIED

# UNCLASSIFIED

.... This paper is UNCLASSIFIED

## BASIC DEVICE PROPERTIES IN THE LEAD CHALCOGENIDES\* (Unclassified)

R. H. Rediker and J. N. Walpole†  
Department of Electrical Engineering  
Massachusetts Institute of Technology  
Cambridge, Massachusetts

### ABSTRACT

New developments in the understanding of basic device parameters important to the operation of infrared lasers and detectors in the lead and lead-tin chalcogenides are reviewed. These include: (1) the diffusion parameters which determine the depth of p-n junctions, the concentration profiles near the junctions, and other parameters necessary for annealing and processing these nonstoichiometric compounds; (2) the high electric field transport properties which give information on the rates of impact ionization and the velocity saturation of charge carriers in junction devices; and (3) the surface properties which determine the ohmic or rectifying behavior of metal-semiconductor contacts and which permit an unusual metal-semiconductor minority carrier injection mechanism.

### INTRODUCTION

This paper reviews some of the research performed over the past several years at M. I. T. to develop an understanding of basic parameters and technology in the Pb and Pb-Sn chalcogenides with the ultimate aim to improve device performance in these materials. Three programs will be described. The first program was directed towards the understanding of the diffusion processes in these materials and the determination of the diffusion parameters which control the depth of p-n junctions, and the concentration profile near these junctions. A knowledge of the diffusion process is also extremely valuable in the understanding and optimization of the annealing process used to reduce carrier concentration as well as to improve other material properties in these nonstoichiometric compounds. The work in this first program formed the Ph.D. thesis of Richard Guldi<sup>(1)</sup> and the M. S. thesis of Robert Broderson,<sup>(2)</sup> and has been described in part in the literature.<sup>(3)-(5)</sup> The second program was an investigation of the high electric-field transport properties of the Pb and Pb-Sn chalcogenides, in which the saturation velocity of the charge carriers and the rates of impact ionization were determined. The saturation velocity is important in determining the ultimate high-speed performance of photodiodes, particularly when one tries to mitigate the effect of the higher dielectric constant of the Pb chalcogenides and resultant higher junction capacitance by making the depletion region wider and the capacitance lower. The ultimate speed of the photodiode is in this case limited by the transit time of the carriers across the depletion region. The rate of impact

---

Supported by the Office of Naval Research

\* Present address: M. I. T. Lincoln Laboratory, Lexington, Mass.

# UNCLASSIFIED

ionization is relevant to avalanche breakdown in junctions, and as will be described below, the results suggest that avalanche breakdown should be much less of a problem in the Pb or Pb-Sn chalcogenides than in InSb, even though the bandgap — direct in both cases — is significantly smaller in the Pb-Sn chalcogenides. The work in this second program formed the Ph. D. thesis of Hugues St. Onge, <sup>(6)</sup> and the M. S. thesis of F. J. Leonberger, <sup>(7)</sup> and has also been described in part in the literature. <sup>(8)-(10)</sup> The third program was a study of metal-semiconductor contacts in the Pb-Sn chalcogenides and of the surface properties which determine whether such contacts are ohmic or rectifying. It turns out in fact that one can make a metal-semiconductor contact on p-type materials which will inject minority carriers into the semiconductor, as will be described below. The results of this program, which was in collaboration with K. Nill of Lincoln Laboratory, have been reported in detail in the literature. <sup>(11)-(13)</sup>

## DIFFUSION PROCESSES IN THE Pb-Sn CHALCOGENIDES

The all-pervading fact of life in the lead chalcogenides and their alloys is their deviation from stoichiometry. In Fig. 1 is shown a portion of the phase diagram for PbTe and (PbSn)Te near the stoichiometric composition of 50 atomic percent Pb, 50 atomic percent Te. The horizontal scale in this figure is greatly expanded. The arch-shaped curve in the center is the solidus curve for PbTe and gives as a function of temperature the limits of stability of the compound in the solid phase. The maximum excursion in the limit of stability as shown for the solid phase of PbTe is approximately from 50.01 percent Pb, 49.99 percent Te to 49.99 percent Pb, 50.01 percent Te. The liquidus line on the expanded scale of the figure is nearly flat; it does curve down eventually on either side of the compound.

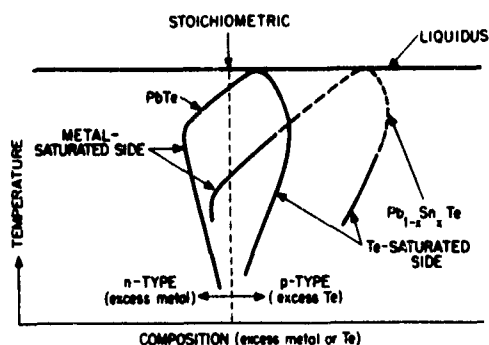


Figure 1. Expanded region of the phase diagrams for PbTe and (Pb, Sn)Te near the stoichiometric composition showing schematically the solidus lines or saturation limits of the compound or alloy and the liquidus line, which is nearly flat on the expanded scale.

The deviations from stoichiometry in the solid phase are due on a microscopic scale to point defects in the crystal lattice. <sup>(14)</sup> Excess Te results from Pb vacancies or Te interstitials, or both, while excess Pb results from Te vacancies or Pb interstitials, or both. The defects responsible for the deviations from stoichiometry are electrically active: Pb interstitials and Te vacancies acting as donors, and Te interstitials and Pb vacancies acting as acceptors. Thus, PbTe with excess metal is n-type and PbTe with excess Te is p-type. Knowledge of the extent of the range of the deviation from stoichiometry is obtained by measuring the carrier

# UNCLASSIFIED

density in saturated samples. The saturated samples are produced by annealing samples at the appropriate temperature with excess metal for the metal-saturated side or with excess Te for the Te-saturated side. (15)

If a sample is originally saturated n-type and then is heated at an appropriate temperature in a Te-rich environment, a p-type skin will be produced at the surface, as determined from the phase diagram. A gradient in the deviation from stoichiometry is established from this p-type skin into the n-type bulk and with time, the p-n junction will move deeper into the sample. The process by which the p-n junction is formed and moves into the sample is called interdiffusion (3), (4), (16) and involves the motion of lead and Te interstitials and vacancies in opposite directions due to this gradient in the deviation from stoichiometry. The motion of the junction appears to obey Fick's law — that is, the junction diffuses into the sample as though the process were described by a constant diffusion coefficient, and the junction depth varies as the square root of the diffusion time. It has been found, however, that for diffusion of n into p, the junction diffusion coefficient is larger by at least an order of magnitude in PbTe than for diffusions of p into n. (17) The opposite is true in PbSe. (15) For device applications it is very important to explain this effect, predict the junction diffusion coefficients, and understand the concentration profiles near the junction.

We have made new measurements of the tracer diffusion coefficients for  $Pb^{210}$  and  $Se^{75}$  in PbSe, which we have theoretically related to the interdiffusion constant for p-n junctions, expanding on the original treatment by Brebrick. (16) The interdiffusion predicted by our theory from radio-tracer results has been compared with experimental results on the diffusion of p-n junctions. The concentration profiles near the p-n junction as predicted by our theory from radiotracer measurements are presented.

In Fig. 2 the diffusion coefficient of  $Se^{75}$  in both Pb-saturated and Se-saturated PbSe is shown as a function of reciprocal temperature. Also shown in the figure are earlier results of Ban and Wagner, (18) which, as can be noted, do not agree with our results. This disagreement is believed to be real and due mainly to crystalline quality and surface preparation. The disagreement indicates that in obtaining information significant for devices, it is important to use device quality materials and processing steps consistent with those used in device fabrication. From Fig. 2 it is possible to obtain information on the mechanism for diffusion of Se in PbSe. There are five prominent mechanisms for diffusion in such a nonstoichiometric crystal: diffusion of vacancies, either

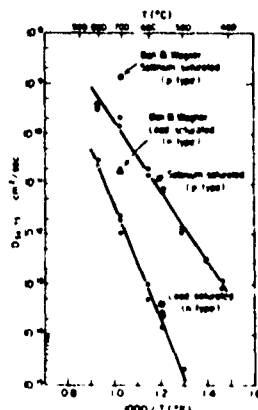


Figure 2. Measured diffusion coefficients of  $Se^{75}$  in lead-saturated and selenium-saturated PbSe. The arrows indicate data of other workers obtained at 700°C.

# UNCLASSIFIED

metal or non-metal; diffusion of interstitials, either metal or non-metal (including the interstitialcy mechanisms in which the interstitial displaces an atom which in turn becomes an interstitial); and diffusion of divacancies which are metal vacancy non-metal vacancy pairs. The divacancy mechanism has been shown to exist in NaCl<sup>(19)</sup> and InSb.<sup>(20)</sup> Since the concentration of selenium interstitials is obviously larger in selenium-rich material than in lead-rich material, while the opposite is true for selenium vacancies, and since the concentration of divacancies is independent of composition, it is clear that an interstitial diffusion mechanism holds for Se in selenium-rich material.\*

The experimental data obtained for Pb<sup>210</sup> tracer diffusion under conditions of Pb saturation and also of Se saturation are compared in Fig. 3 with earlier published data of Seltzer and Wagner.<sup>(21)</sup> Unfortunately, in the early experiments of Seltzer and Wagner, in addition to material quality problems, the defect concentration was not controlled. It should be pointed out that the theory of tracer diffusion<sup>(4)</sup> predicts that the larger of the two values of the diffusion coefficient observed at the two (metal and Te-rich) saturation limits would be the upper bound to the value of the diffusion coefficient at any deviation from stoichiometry between the saturation limits. Thus, as in the case of Se<sup>75</sup> tracer diffusion, our results for Pb<sup>210</sup> tracer diffusion do not agree with the earlier published data. Because the diffusion constant for Pb<sup>210</sup> in lead-saturated material (Fig. 3) is almost identical for Se in the same material (Fig. 2), it is expected that the divacancy mechanism for diffusion may be of importance in n-type material.

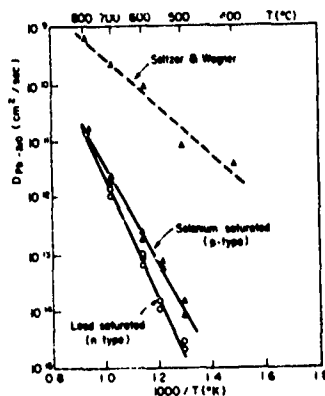


Figure 3. Measured diffusion coefficients of Pb<sup>210</sup> in lead-saturated and selenium-saturated PbSe. Also shown are the data of Seltzer and Wagner.

From these tracer results, one can determine the interdiffusion coefficient. For the purposes of this review, it will be assumed that diffusion via the divacancy mechanism can be neglected in this theoretical treatment. However, the corrections to the results if this assumption is inappropriate will be described. The results of the theory will be given; for detailed derivations, the reader is referred to Refs. 1 and 4. Two material parameters which are important in diffusion in non-stoichiometric semiconductors are first,  $n_i$ , the intrinsic carrier concentration, where

\* We rule out diffusion of Se through Pb vacancies since this mechanism implies antistructure disorder, which is unlikely in the Pb chalcogenides.

# UNCLASSIFIED

$n_i^2$  is equal to the product of the equilibrium hole and electron concentrations ( $n_i^2 = pn$ ); and second,  $k_o$ , the intrinsic disorder constant, where  $k_o$  is equal to the product of the concentrations of acceptor-type defects and donor-type defects,

$$k_o(T) = (V_N + I_M)(V_M + I_N) \quad (1)$$

where  $V_N$  and  $V_M$  are the concentrations of non-metal and metal vacancies, respectively, and  $I_N$  and  $I_M$  are the concentrations of non-metal and metal interstitials, respectively. If there were no interstitial defects ( $I_N = I_M = 0$ ),  $k_o$  would be the Schottky constant of the material. If we define  $\Delta$  as the deviation from stoichiometry in units of carriers  $\text{cm}^{-3}$  (each defect is assumed to produce one corresponding carrier), the interdiffusion coefficient is given by

$$D_{\Delta} = \{ D_p f + D_n (1 - f) \} \left[ 1 + \sqrt{(\Delta^2 + 4k_o) / (\Delta^2 + 4n_i^2)} \right] \quad (2)$$

where  $D_p$  and  $D_n$  are quantities that are calculated in Eqs. (4) to (11) below from the tracer diffusion coefficients, and  $f$  is the fraction of defects which are acceptor-type,

$$f = \frac{V_M + I_N}{V_M + I_N + V_N + I_M} = \frac{1}{2} \left[ 1 - \Delta / (\Delta^2 + 4k_o)^{1/2} \right] \quad (3)$$

Since  $D_p$  and  $D_n$  will be shown to be significantly different from each other, the interdiffusion coefficient varies appreciably with  $f$ , whose value changes according to Eq. (3) from unity in strongly p-type material to zero in strongly n-type material. Thus,  $f$  is the modulating function which changes the character of the interdiffusion coefficient as the deviation from stoichiometry changes from one type to another. The factor in square brackets in Eq. (2) does not contribute significantly to the variation of  $D_{\Delta}$  with  $\Delta$ .

The interdiffusion parameters  $D_p$  and  $D_n$  can be expressed in terms of the parameters

$$D_{pM}, D_{pN}, D_{nM}, D_{nN}$$

$$D_p = D_{pM} + D_{pN} \quad (4)$$

$$D_n = D_{nM} + D_{nN} \quad (5)$$

which in turn can be expressed providing  $\Delta^2 \gg 4k_o$  in terms of the four tracer diffusion constants we have measured:  $D_M(\Delta = p_{\text{sat}})$ ,  $D_M(\Delta = n_{\text{sat}})$ , the diffusion of  $\text{Pb}^{205}$  in selenium and lead-saturated material, respectively, and  $D_N(\Delta = p_{\text{sat}})$ ,  $D_N(\Delta = n_{\text{sat}})$ , the diffusion of  $\text{Se}^{75}$  in selenium and lead-saturated material, respectively, as given below:

$$D_{pM} = \frac{SD_M^*(p_{\text{sat}})}{p_{\text{sat}} f_v} \left[ 1 - \frac{k_o}{n_{\text{sat}} p_{\text{sat}}} \frac{D_M^*(n_{\text{sat}})}{D_M^*(p_{\text{sat}})} \right] \quad (6)$$

$$D_{nM} = \frac{SD_M^*(n_{\text{sat}})}{n_{\text{sat}} f_{Mi}} \left[ 1 - \frac{k_o}{n_{\text{sat}} p_{\text{sat}}} \frac{D_M^*(p_{\text{sat}})}{D_M^*(n_{\text{sat}})} \right] \quad (7)$$

$$D_{pN} = \frac{SD_N^*(p_{\text{sat}})}{p_{\text{sat}} f_{N1}} \left[ 1 - \frac{k_o}{n_{\text{sat}} p_{\text{sat}}} \frac{D_N^*(n_{\text{sat}})}{D_N^*(p_{\text{sat}})} \right] \quad (8)$$

$$D_{nN} = \frac{SD_N^*(n_{\text{sat}})}{n_{\text{sat}} f_v} \left[ 1 - \frac{k_o}{n_{\text{sat}} p_{\text{sat}}} \frac{D_N^*(p_{\text{sat}})}{D_N^*(n_{\text{sat}})} \right] \quad (9)$$

# UNCLASSIFIED

where the quantity  $S$  is the concentration of lattice site and  $f_{Ni}$ ,  $f_{Mi}$ , and  $f_v$  are correlation factors. The correlation factor  $f_v$  for vacancy diffusion is 0.7815 for the rock salt crystalline structure of PbSe. It differs from unity because once a tracer atom has moved by jumping into a particular vacancy, there is a greater than random probability that it will make its next jump back into the same vacancy. The values for correlation factors  $f_{Ni}$  and  $f_{Mi}$  depend on whether the interstitialcy mechanism (where the interstitial replaces a lattice site atom, which in turn becomes an interstitial) is important and can be as low as 0.33 or as high as unity.

From these equations it can be seen that only the order of magnitude of  $k_0$  need be known to determine whether the second terms in the brackets are negligible. When the second terms in the brackets may be dropped, as is the case for PbSe and PbTe, the interdiffusion parameters  $D_p$  and  $D_n$  may be obtained by using Eqs. (4) and (5).

$$D_p = \frac{S}{p_{sat}} [D_M^*(p_{sat})/f_v + D_N^*(p_{sat})/f_{Ni}] \quad (10)$$

$$D_n = \frac{S}{n_{sat}} [D_M^*(n_{sat})/f_{Mi} + D_N^*(n_{sat})/f_v] \quad (11)$$

By substituting the values of  $D_p$  and  $D_n$  from Eqs. (10) and (11) into Eq. (2), the interdiffusion coefficient  $D_\Delta$  can be obtained as a function of the deviation from stoichiometry,  $\Delta$ . In the comparison of the experimental results for  $D_\Delta$  with those predicted by Eq. (2), it will be possible to put bounds on the correlation factor for diffusion of interstitial selenium  $f_{Ni}$ , which as described above depends on details of this diffusion. Thus, our results yield information on the mechanism of interstitial diffusion. In Fig. 4, we have plotted  $D_\Delta$  as a function of the deviation from stoichiometry for  $k_0 \ll n_i^2$ , an extremely good assumption for the temperatures of the diffusions. Also shown in this figure is a step function model approximation to  $D_\Delta(\Delta)$ .<sup>(3)</sup> As mentioned above, the approximation that diffusion by divacancies is negligible which has been made in deriving  $D_\Delta$  from the tracer results may not be correct for n-type material. In this case, the values which have been derived from the tracer data in n-type material for  $D_n$  are upper bounds to the actual values since the divacancy mechanism does not contribute to interdiffusion.<sup>(1), (4)</sup>

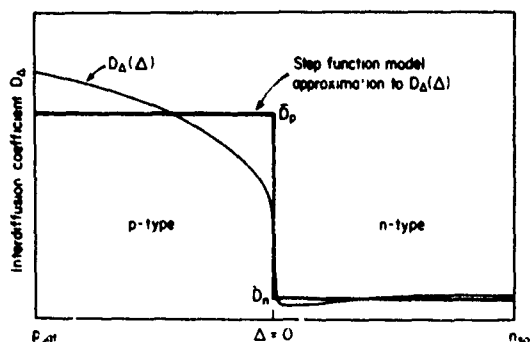


Figure 4. Schematic dependence of the interdiffusion coefficient  $D_\Delta$  on the deviation from stoichiometry  $\Delta$  and the step function approximation to  $D_\Delta$ .

Using these results for the variation of the interdiffusion coefficient  $D_\Delta$  with the deviation for stoichiometry, we have determined the concentration profile for the diffusion of n- into p-type material and for the diffusion of p- into n-type material. We have shown that the error introduced into these computer calculations by the use of the step-function approximation is less than a few percent, so in most cases for ease in computation, we have used the step-function approximation.



# UNCLASSIFIED

Figure 5 shows computed concentration profiles for p into n and n into p diffusions. The distance into the sample is normalized by the square root of time. There are several important pieces of information that can be obtained from this figure that are important to the device maker. First, note where the p-n junction occurs. Remember the diffusion in the p-type material is much larger than that in n-type material. For p into n diffusion, the junction is even deeper than predicted by the larger diffusion constant; for n into p diffusion, the junction is even shallower than predicted by the smaller diffusion constant. Also note that for n into p diffusion, our computations indicate that one can obtain a relatively lightly doped region extending from the p-n junction fairly deeply into the bulk. This is very significant because it predicts that one can use an optimized n into p diffusion to produce a relatively wide low-carrier region near the junction,<sup>(3)</sup> reducing junction capacitance and increasing the junction breakdown voltage.

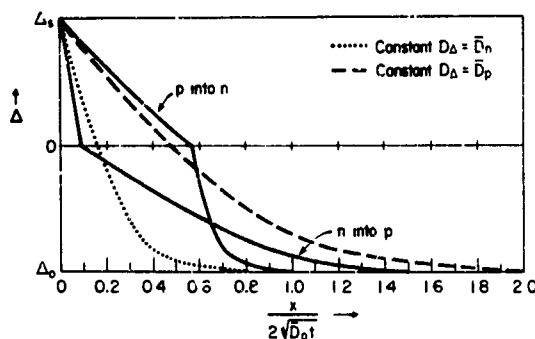


Figure 5. Calculated interdiffusion profiles using the step function approximation for  $\bar{D}_p = 9\bar{D}_n$  and  $\Delta_0$  the initial deviation of a semi-infinite sample, equal in magnitude to  $\Delta_s$ , the deviation at the surface. Distance into the sample  $x$  is normalized by the square root of time  $t$ .

Calawa and co-workers<sup>(15)</sup> observed several years ago that the motion of the p-n junctions obeyed Fick's law for diffusion — that is, the junctions diffuse in as though the process were described by a constant diffusion coefficient. Our radiotracer-derived results for the position of the p-n junction also follow Fick's law since the abscissa is normalized by the square root of time. Figure 6 compares experimental results of Calawa and co-workers<sup>(15)</sup> with the theoretical junction diffusion coefficients determined from the tracer data. The solid lines indicate the temperature range for which the predictions are based on actual tracer measurements, while the dashed lines indicate that the tracer data have been extrapolated to the lower temperature ranges. Note that all of the p-n junction data were taken with the same value of bulk carrier concentration  $\Delta_0$ , whereas the n-p junction data were taken for a wide range of the values of  $\Delta_0$ , the limits of which are indicated on the figure. Note that many of the data points which appear to agree with the n-p line for  $\Delta_0 = 5.4 \times 10^{17} \text{ cm}^{-3}$  are actually in disagreement since they correspond to  $\Delta_0 = 1.5 \times 10^{19} \text{ cm}^{-3}$ .

The agreement in Fig. 6 for the p into n junctions is excellent both in magnitude and in the variation with temperatures. The agreement in slope is most significant. The magnitude however, depends upon the exact value of the correlation factor for selenium interstitials. If a smaller value is taken for  $f_{Ni}$ , the theoretical line is shifted toward larger diffusion coefficients. It is difficult to distinguish between the interstitial diffusion mechanism (for which  $f_{Ni} = 1.0$ ) and the direct interstitialcy mechanism (in which the interstitial moves to a lattice site and the displaced lattice atom moves in the same direction to an adjacent interstitial position and for which  $f_{Ni} = 0.73$ ).

# UNCLASSIFIED

because of the scatter in both the tracer and the junction data. However, it can be safely concluded that the indirect interstitialcy mechanism (in which the original interstitial and the displaced lattice atom move in different directions and for which  $f_{NI} = 0.33$ ) is not significant.

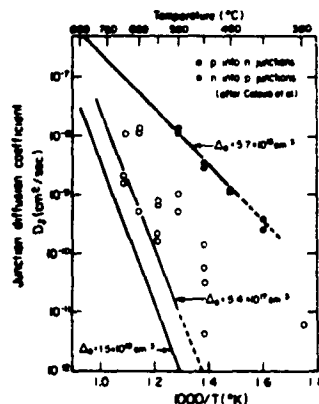


Figure 6. Comparison of PbSe experimental junction diffusion coefficients with predictions from tracer data. The solid lines are predictions in the temperature range of the tracer measurements and the dashed portions are extrapolations to lower temperatures than actually measured. The experimental points lying near the predicted line for  $\Delta_0 = 5.4 \times 10^{17} \text{ cm}^{-3}$  were actually obtained for  $\Delta_0 = 1.5 \times 10^{19} \text{ cm}^{-3}$ .

The disagreement in Fig. 6 for the n into p diffusions is believed to be due to the fact that, as shown in Fig. 5, on the one hand the junction is very shallow and thus can be greatly influenced by the perfection of the surface layer, and on the other hand there is significant diffusion in the long tail over a relatively large distance from the surface, which for the experimental results in Fig. 6 was comparable with the thickness of the samples. The lines in Fig. 6 were derived from the tracer data under the assumption that the sample thickness was infinite. It is obvious that if the thickness becomes small enough so it either sets a boundary condition on the diffusion, or if diffusion from the other side overlaps the diffusion from the first side, then the junction depth will be affected. Calculations taking into account finite thickness have been made<sup>(1)</sup> and bring results into better but by no means complete agreement. The possibility of surface damage affecting the results of the n into p junctions cannot be excluded. Lastly, it should be pointed out that when any contribution to the tracer coefficients due to divacancy diffusion, which we could not exclude for n-type material, is subtracted from the value of  $D_n$ , the junction diffusion coefficients predicted from the tracer results for n into p diffusion become even smaller, and the disagreement between them and the experimental junction diffusion coefficients even larger.

As a further test of the applicability of the interdiffusion model that has been developed, the model has been used to correlate for PbTe the published tracer data of Gomez, et al.<sup>(22)</sup> with the published junction data of Goldstein,<sup>(17)</sup> as shown in Fig. 7. The agreement again indicates that the model is appropriate and can be used in PbSe and PbTe to predict with good accuracy junction depths and profiles.

# UNCLASSIFIED

theoretical predictions<sup>(13)</sup> for the model of Fig. 11b. Such a plot is shown in Fig. 13, where the voltage intercept is 283 mV, much larger than the energy gap for PbTe at 77°K (205 meV). For p-n junctions at 77°K, the voltage intercept is actually smaller than the energy gap.<sup>(26)-(28)</sup>

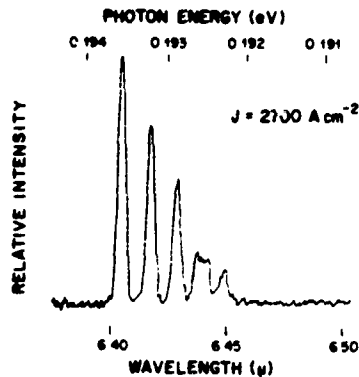


Figure 12. Laser emission spectrum for an evaporated lead barrier on p-PbTe obtained at 1.8°K.

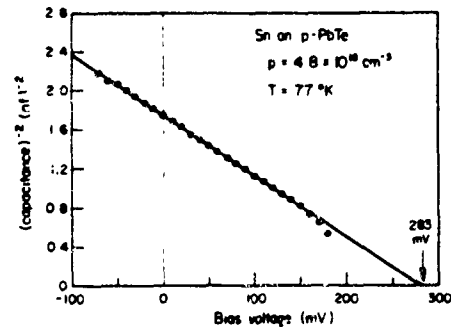


Figure 13. The capacitance-voltage characteristic for a Sn barrier on p-PbTe at 77°K.

The results just described which show that PbTe tends to obey the theory of ideal metal-semiconductor contacts are very important to the device maker in making ohmic contacts to devices or in making Schottky barrier-type devices. As a matter of fact, following publication of our work, in which the observation of photovoltaic response was reported,<sup>(12)</sup> excellent Schottky barrier-type detectors have been made in industry.<sup>(29)</sup>

## ACKNOWLEDGMENTS

The metal-semiconductor contact program was performed in collaboration with Kenneth Nill. We wish to acknowledge the major roles of our students, R. L. Guldi, R. Broderson, H. St. Onge, and F. Leonberger in the research reported here. We wish to thank A. Colozzi and J. Walsh for help in semiconductor fabrication and electronic instrumentation and A. R. Calawa and T. C. Harman for help when needed.

## QUESTION AND ANSWER SESSION

- Q. Have diffusion studies of the lead salts established the number of charge carriers associated with lattice sites?
- A. At one time we were convinced it was on a one-for-one basis, but now we are not so sure.

# UNCLASSIFIED

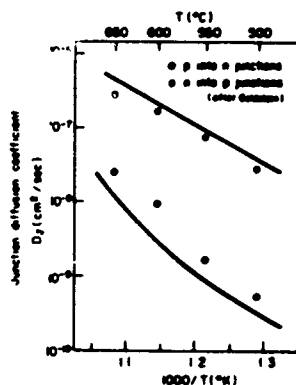


Figure 7. Comparisons of PbTe experimental junction (17) diffusion coefficients shown by the points from Goldstein (22) with prediction based on the tracer data of Gomez, et al (22) shown by the solid lines.

## HIGH ELECTRIC FIELD TRANSPORT IN THE LEAD-TIN CHALCOGENIDES

Nanosecond pulse techniques have been used to measure the velocity-field characteristics of bulk samples of PbSe, PbTe, and  $\text{Pb}_{0.83}\text{Sn}_{0.17}\text{Te}$  at 77°K and 4°K for carrier concentrations ranging from  $1 \times 10^{17} \text{ cm}^{-3}$  to  $5 \times 10^{17} \text{ cm}^{-3}$ . Because of these high carrier concentrations, sample current densities of the order of  $10^6 \text{ A cm}^{-2}$  were required to obtain data on the carrier saturation velocity and on impact ionization. To prevent sample heating, it was essential that the samples have extremely small cross sections and that current be applied in very short pulses. (6,8)

Some typical samples are shown in Fig. 8. The active lengths of the samples were the order of 1 mm, with cross-sectional dimensions of the order of 1/20 mm. The maximum current applied to these samples was about 80 A in pulses of 10 to 20 nanoseconds. The problems in short-pulse measurements were further exacerbated by the high mobilities of these materials, because of which the resistance of these samples at the cryogenic temperature of interest were of the order of one ohm. Another experimental problem was making ohmic contacts to these extremely small cross-section samples, contacts that would stay ohmic up to current densities of  $10^6 \text{ A cm}^{-2}$ . We were able to make such contacts to n-type PbSe, PbTe, and (PbSn)Te and to p-type PbSe. Unfortunately, we were unable to make contacts which remained ohmic to the required current density in p-type PbTe.



Figure 8. Samples of PbTe used for high-field studies.

# UNCLASSIFIED

The carrier velocity is plotted as a function of electric field for three n-type materials in Fig. 9. More correctly, the ordinate in this figure is the current density divided by the product of the zero-field carrier density and the electronic charge, and is equal to the carrier velocity only as long as there is no carrier multiplication, or as long as the carrier density does not change. Each of the three materials is characterized by an ohmic or linear velocity-field characteristic at low fields, followed by a clear tendency toward velocity saturation at about  $10^7$  cm/sec. Finally, at various fields, one observes either an inflection in the characteristic or an instability characterized by current and voltage oscillations at several hundred MHz.

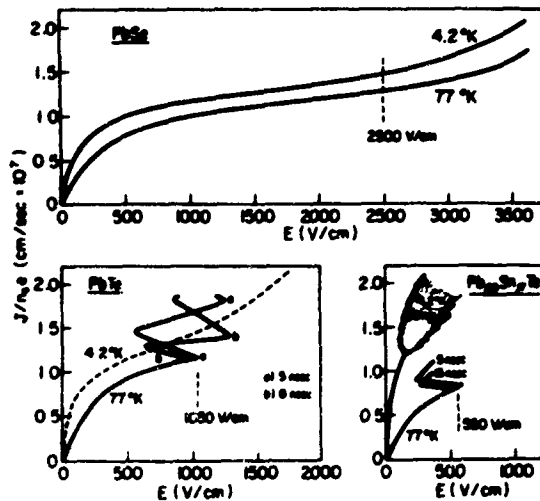


Figure 9. The apparent velocity of carriers  $J/n_0e$ , where  $J$  is current density,  $n_0$  the equilibrium carrier density, and  $e$  the electronic charge versus electric field  $E$  for n-type PbSe, PbTe, and  $Pb_{0.9}Sn_{0.1}Te$  at 4.2 and 77°K. The S-shaped negative resistance characteristics are the result of plotting data at a particular time during the pulse in the field region where instabilities are seen.

The low-field linear regions where each material can be characterized by a mobility given by the slope of the characteristic are in very good agreement with the theory of polar optical scattering of charge carriers in semiconductors. <sup>(6), (8)</sup> The experimentally determined saturation velocity of about  $10^7$  cm/sec is within a factor of two of that predicted by various theoretical approximations to the high-field case, such as that of Stratton using a displaced Maxwellian <sup>(23)</sup> or that of Dumke using a distribution function streamed along the direction of applied electric field. <sup>(24)</sup> The saturation velocity is an important parameter for the operation of high-speed detectors with wide depletion regions. In these detectors the speed of response may be limited by the time it takes the carriers traveling at the saturation velocity to traverse this space-charge region. While not shown in the figure, the saturation velocity for p-type PbSe is also about  $10^7$  cm/sec. The inflection point is also very important for detector applications because it is associated with impact ionization of carriers. When the electron-hole plasma produced by impact ionization forms, self-pinching effects occur which produce either stable or unstable characteristics. The inflection point instabilities, their physical explanation, and corroborating data using sample probes and applied dc magnetic fields, are discussed in Ref. 9. In a junction detector, impact ionization which can produce avalanche

# UNCLASSIFIED

breakdown will limit the voltage which can be used to bias the detector. It should be noted that impact ionization occurs in bulk material at electric fields above  $1000 \text{ V cm}^{-1}$  in PbSe and PbTe, significantly higher fields than the  $250 \text{ V cm}^{-1}$  which has been reported<sup>(25)</sup> for impact ionization in bulk InSb, which has a larger bandgap. It should also be noted that although the bandgap of PbSe is smaller than that of PbTe, the electric field for impact ionization is larger.

The reason for the larger electric field required for impact ionization in the Pb-Sn chalcogenides is the larger polaron coupling constant in these materials, the large interaction of the electron with the polarization modes of the crystal. The polaron coupling constant is given by

$$\alpha = \frac{e^2}{2\hbar w_0} \left( \frac{2m^* w_0}{\hbar} \right)^{\frac{1}{2}} \left( \frac{1}{\epsilon_\infty} - \frac{1}{\epsilon_s} \right) \quad (12)$$

where  $w_0$  is the longitudinal optical phonon frequency,  $\epsilon_\infty$  is the high-frequency dielectric constant, and  $\epsilon_s$  is the static dielectric constant. Because the static dielectric constant is so large in the Pb-Sn chalcogenides, the quantity  $1/\epsilon_s$  is relatively small and can be neglected, whereas in other semiconductors, it is important in reducing the value of  $\alpha$ . Listed in Table I for InSb, PbSe, and PbTe are the values of  $\alpha$  and some of the constants used in Eq. (12) to determine this parameter. Note that the polaron coupling constant  $\alpha$  is nearly an order of magnitude larger in the Pb chalcogenides than in InSb. The reason that  $\alpha$  is larger for PbSe than for PbTe is because  $\epsilon_\infty$  is smaller in PbSe than in PbTe, the differences in  $1/\epsilon_s$  not being important because the value of this quantity itself is small.

TABLE I  
CONSTANTS USED IN CALCULATION OF  
GENERATION RATE BY IMPACT IONIZATION

	<u>InSb</u>	<u>PbSe</u>	<u>PbTe</u>
$\hbar w_0$ (eV)	0.0238	0.0165	0.0136
$\epsilon_s$	17.9	280	450
$\epsilon_\infty$	15.7	25.2	36.9
$\alpha$	0.020	0.259	0.175

We have modified the theory by Dumke<sup>(24)</sup> developed to calculate the generation or impact ionization rate as a function of electric field in InSb to take into account the ellipsoidal constant energy surfaces of the Pb-Sn chalcogenides. The modified theory<sup>(10)</sup> assumes dominant polar optical scattering, nonparabolic and ellipsoidal bands, and a distribution function streamed along the direction of the applied electric field. The calculated generation rates (the number of impact ionizations per second per carrier) for the Pb-Sn chalcogenides as well as the rate calculated by Dumke for InSb are plotted in Fig. 10 as a function of electric field. Note that PbSe with larger polaron coupling constant, and hence, stronger polar optical scattering, has a lower generation rate than PbTe, although the gap of PbSe across which the ionization occurs is slightly smaller than that of PbTe. The material (PbSn)Te has approximately the same polaron coupling as PbTe, but the generation rate becomes larger as the energy gap decreases. Note the lower field at which the generation rate becomes appreciable in InSb because of the weaker polaron coupling.

# UNCLASSIFIED

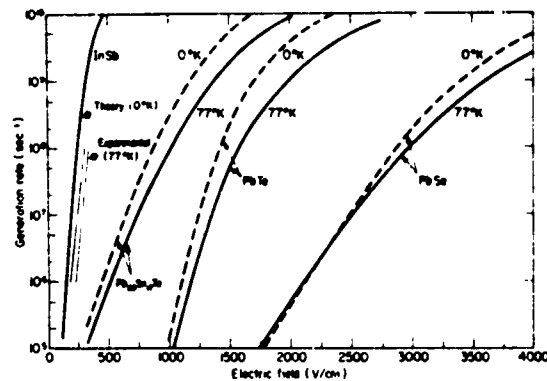


Figure 10. Calculated generation rates versus electric field for the Pb and Pb, Sn chalcogenides at 0°K and 77°K. Dumke's theory<sup>(24)</sup> for InSb is shown for comparison together with the data of McGroddy and Nathan.<sup>(25)</sup>

For the lengths of the samples such as shown in Fig. 8, which were used to obtain the experimental results in this program, a generation rate of  $10^6$  to  $10^7$  leads to observable carrier multiplication of about 10 percent, which should be adequate to produce the inflection point observed in the characteristics.<sup>(9)</sup> The experimental inflection points are compared with those predicted from the theory in Table II. Since, as can be seen in the table, the agreement between the theory and experiment is very good, one can with some confidence use the theory to calculate, for example, the avalanche breakdown limitations in photodiodes.

TABLE II  
COMPARISON OF EXPERIMENTAL INFLECTION  
POINTS WITH THOSE PREDICTED BY THEORY

		Experimental Inflection Point	Theory: $g = 10^6 - 10^7 \text{ sec}^{-1}$
PbSe	77°K	2500 V/cm (stable)	2150 ~ 2500
	4.2°K	2200 (stable)	2150 ~ 2500
PbTe	77°K	1050 (unstable)	1200 ~ 1350
	4.2°K	1000 (stable)	1100 ~ 1250
Pb <sub>0.83</sub> Sn <sub>0.17</sub> Te	77°K	550 (unstable)	500 ~ 750
	4.2°K	140 (unstable)	450 ~ 650

## METAL SEMICONDUCTOR CONTACTS TO PbTe

The metal-semiconductor contacts discussed in this section were prepared by evaporating an array of small metal pads on a freshly etched or air-cleaved surface. Prior to etching or cleaving, a large-area ohmic contact was alloyed to one side of the crystal using a gold-thallium eutectic for p-type PbTe and indium for n-type PbTe. The metal pads were about 0.004 inch in diameter as

# UNCLASSIFIED

determined by a stainless-steel evaporation mask. During evaporation the sample and evaporation mask were cooled to liquid-nitrogen temperature to prevent diffusion of the deposited metal. Furthermore, an electron-beam evaporation source was used to prevent exposure of the sample to the heat of an evaporation coil and the evaporation was done as quickly as possible. Typical evaporations were performed in a vacuum of  $10^{-6}$  to  $10^{-7}$  Torr for 5 sec, with resulting depositions of 800 to 1000 Å. These procedures were necessary to obtain reproducible results. <sup>(11)-(13)</sup> The samples of PbTe were prepared from either as grown or annealed Bridgman crystals having carrier concentrations between  $10^{17}$  and  $5 \times 10^{18} \text{ cm}^{-3}$ .

Table III is a summary of the electrical behavior of evaporated metal-semiconductor contacts for six metals on n and p PbTe. The electron affinity  $\chi$  of 4.6 eV for PbTe is the energy difference between the conduction band and the vacuum level. The work function  $\phi$  is the energy difference between the Fermi level in the metal and the vacuum level. When the sum of the electron affinity and the energy gap is smaller than the work function, the metal-semiconductor contact is rectifying for n-type and ohmic for p-type. Conversely, if the electron affinity is larger than the work function, the metal-semiconductor contact is rectifying for p-type and ohmic for n-type. If the electron affinity is nearly equal to the work function, the metal-semiconductor contact is rectifying for both n- and p-type semiconductors. This electrical behavior is exactly that predicted by the theory of the ideal metal-to-semiconductor contacts.

TABLE III  
BEHAVIOR OF EVAPORATED M-S CONTACTS  
ON n- AND p-PbTe

Metal Work Function ( $\phi_m$ ) eV		Experimental	
		Metal	Observation
$\chi < \phi_m$	5.4	Pt	Barriers on n-type Ohmic to p-type
$\chi \approx \phi_m$	4.6	Au	Barriers on n- and p-type
$\chi > \phi_m$	4.4	Sn	Barriers on p-type Ohmic to n-type
	4.2	Zn	
	4.0	Pb	
	3.8	In	

The band energy is plotted as a function of distance in Fig. 11a for an ideal metal-semiconductor contact on PbTe where  $\phi_m = 4.7 \text{ eV}$ . Because the Fermi levels in the metal and the semiconductor must be at the same energy, the bands in the semiconductor bend approaching the metal-semiconductor interface, so at this interface the energy difference from the vacuum level to the semiconductor conduction band and to the metal Fermi level is given by the electron affinity and the work function, respectively. Shown in Fig. 11a is a case where  $\chi < \phi_m < \chi + E_g$ , where  $E_g$  is



# UNCLASSIFIED

the semiconductor energy gap. For these values of  $\phi_m$ , the metal Fermi level at the interface corresponds to an energy in the forbidden gap in the semiconductor and the metal-semiconductor contact is a Schottky barrier. (It should be mentioned that most semiconductors used in devices today such as Ge, Si, and most of the III-V's do not obey the theory of ideal metal-semiconductor contacts and have interface states in the forbidden gap which tend to pin the semiconductor band at the interface to produce a band energy diagram similar to Fig. 11a nearly independent of the metal work function.)

In Fig. 11b the band energy is plotted as a function of distance for an ideal Pb evaporated contact to PbTe. The band energy diagram of Fig. 11b is very interesting because it predicts that for Pb on PbTe, one actually gets an inverted layer in the semiconductor, one does not have a Schottky barrier but one has a p-n junction. This diagram predicts that one could make a laser from such a metal-semiconductor contact, and we have done so.

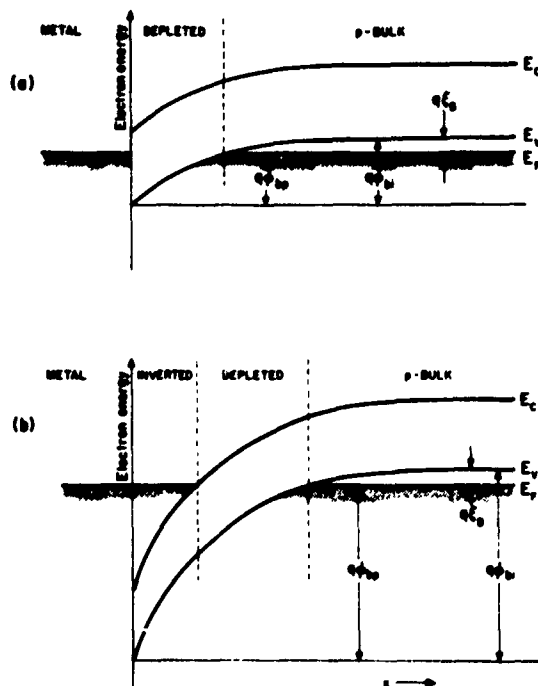


Figure 11. Barrier potential versus distance for metal-semiconductor barriers: (a) the usual Schottky barrier; (b) the inverted surface barrier.

Figure 12 shows the spectrum of the laser emission from such an evaporated Pb to PbTe device. The mode structure shown is that expected from the laser cavity, and threshold currents have been of the order of  $100 \text{ A cm}^{-2}$ , as low as one obtains typically in the best PbTe p-n junction lasers. This lasing action is proof positive that the surface is inverted, and is another indication that in PbTe the metal-semiconductor contacts obey the ideal theory. We have also demonstrated from capacitance-voltage data at  $77^\circ\text{K}$  on these metal-semiconductor devices that these devices are truly different from ordinary p-n junctions and that the inverted layer does not result from any donor-type behavior of the evaporated metal. When the capacitance  $C$  is plotted as  $C^{-2}$  versus voltage, the intercept of the resulting straight line with the voltage axis is in agreement with

# UNCLASSIFIED

## References

1. R. L. Guldi, Ph.D. Thesis, M.I.T., October 1971 (unpublished).
2. R. W. Brodersen, M.S. Thesis, M.I.T., June 1968 (unpublished); Technical Report No. 1, M.I.T. Solid State Device Research Group, October 1968 (available from DDC).
3. R. W. Brodersen, J. N. Walpole, and A. R. Calawa, J. Appl. Phys. 41, 1484 (1970).
4. J. N. Walpole and R. L. Guldi, Proceedings of the Conf. on the Physics of IV-VI Compounds and Alloys, Philadelphia, Pa. 1972 (to be published).
5. R. L. Guldi, J. N. Walpole, and R. H. Rediker (submitted to J. Appl. Phys.).
6. Hugues St. Onge, Ph.D. Thesis, M.I.T., March 1971 (unpublished); Technical Report No. 8, M.I.T. Solid State Device Research Group, April 1971 (available from DDC).
7. F. J. Leonberger, M.S. Thesis, M.I.T., May 1971 (unpublished).
8. H. St. Onge, J. N. Walpole, and R. H. Rediker, Proc. of the Tenth Int'l Conf. on the Phys. of Semiconductors, Ed. by S. P. Keller, J. C. Hansen, and F. Stern (USAEC, Oak Ridge, 1970), p. 391.
9. H. St. Onge, F. J. Leonberger, and J. N. Walpole, Proc. of the Conf. on the Phys. of IV-VI Compounds and Alloys, Philadelphia, Pa. 1972 (to be published).
10. H. St. Onge and J. N. Walpole (submitted to Phys. Rev.).
11. K. W. Nill, A. R. Calawa, T. C. Harman, and J. N. Walpole, Appl. Phys. Lett. 16, 375 (1970).
12. K. W. Nill, J. N. Walpole, A. R. Calawa, and T. C. Harman, Proc. of the Conf. on the Phys. of Semimetals and Narrow Gap Semiconductors, Ed. by D. L. Carter and R. T. Bate (Pergamon Press, New York, 1971) and J. Phys. Chem. Solids 32, Suppl. 1 (1971), p. 383.
13. J. N. Walpole and K. W. Nill, J. Appl. Phys. 42, 5609 (1971).
14. A. J. Strauss and R. F. Brebrick, J. de Phys., Suppl. C4, C4-21 (1968).
15. A. R. Calawa, T. C. Harman, M. Finn, and P. Youtz, Trans. Met. Soc. AIME 242, 374 (1968).
16. R. F. Brebrick, J. Appl. Phys. 30, 811 (1959).
17. L. Goldstein, C. R. Acad. Sc., Paris, 268B, 686 (1969).
18. Y. Ban and J. B. Wagner, J. Appl. Phys. 41, 2818 (1970).
19. L. W. Bass, J. A. Morrison and P. A. Schroeder, J. Appl. Phys. 36, 824 (1964).
20. D. L. Kendall and R. A. Huggins, J. Appl. Phys. 40, 2750 (1969).
21. M. S. Seltzer and J. B. Wagner, J. Chem. Phys. 36, 130 (1962).
22. M. P. Gomez, P. A. Stevenson, and R. A. Huggins, J. Phys. Chem. Solids 32, 325 (1971).
23. R. Stratton, Proc. Phys. Soc. (London) A246, 406 (1958).
24. W. P. Dumke, Phys. Rev. 167, 783 (1968).
25. J. C. McGroddy and M. I. Nathan, Proc. VIII Int'l Conf. on Phys. of Semiconductors, Kyoto, 1966; J. Phys. Soc. Japan 21, Suppl. 1, 437 (1966).
26. R. T. Bate, D. L. Carter, and J. S. Wrobel, Phys. Rev. Lett. 25, 159 (1970).
27. Y. Kanai and K. Shohno, Japan J. Appl. Phys. 2, 6 (1963).
28. H. M. Day and A. C. Macpherson, Proc. IEEE 51, 1362 (1963).
29. E. M. Logothetis, H. Holloway, A. J. Varga, and E. Wilkes, Appl. Phys. Lett. 19, 318 (1971).

# UNCLASSIFIED

.... This paper is UNCLASSIFIED

## STRUCTURAL, CHEMICAL AND PHOTOELECTRONIC PROPERTIES OF LEAD SULFIDE FILMS (Unclassified)

G. H. Blount, D. K. Smith, and R. T. Yamada  
Santa Barbara Research Center  
Goleta, California

### ABSTRACT (Unclassified)

The structural, chemical, and photoelectronic properties are compared for three types of chemically deposited PbS films. The film types differ in the use of an oxidant during the deposition. The films are grainy in structure and show a decrease in grain compaction as the concentration of the oxidant is increased. Average chemical composition is not significantly dependent on the use of the oxidant. Photosensitive films may be described in terms of sensitizing centers which are present only when an oxidant is used but which are not dependent solely on the presence of oxygen. The physical identification of the sensitizing centers has not been determined but may be associated with film structure.

### INTRODUCTION

It is well known that chemically deposited lead sulfide films are made the basis of useful photodetectors, provided particular chemicals are added to the deposition solution. These chemicals are usually referred to as "oxidant" in spite of the fact that their function is not really understood. A summary is given of an investigation into the mechanism of photoconductivity in chemically deposited lead sulfide films and into the role that the oxidant plays.

### MATERIALS INVESTIGATED (Table I)

Three types of chemically deposited lead sulfide films were studied: the no-oxidant type, standard type, and high-oxidant type. The standard type was made from the formulation used by SBRC to produce state-of-the-art detectors for use at about 193 K. This type normally consists of a thin film of approximately 1-micron thickness with material laid down in four successive chemical depositions. Between depositions, the films are stored in distilled water. For this study, one and two coat (1.4 and 1.2 thickness) as well as the standard four coat samples were investigated. This discussion is confined mostly to four coat films. The no-oxidant and high oxidant are variants of the standard formulation. The variation was achieved solely by varying the concentration of oxidant used in the depositions.

The oxidant concentration was increased by a factor of four above the standard amount to produce a high-oxidant material, and the concentration was reduced to zero to produce a no-oxidant variety.

# UNCLASSIFIED

## INVESTIGATIVE TECHNIQUES (Table II)

The various investigations performed are listed in this figure. The first four are directed toward the composition and structure of the film. The last three deal with the electronic properties of the material. Thus, the three types of film were compared in terms of these seven basis analyses.

## CONCLUSIONS (Table III)

Before presenting the results of the analyses of the three types of film, let us indicate the conclusions which can be drawn from the study:

1. As first, we note that the structure and electrical properties, not unsurprisingly, are typical of grainy materials with intergrain barriers.
2. Somewhat more unexpected is the conclusion that the photoconductivity can be explained in terms of sensitizing centers without reference to the barriers.
3. As a complete surprise, we must conclude that the average concentration of oxygen within the film is not controlled by the use of the oxidant. There is no significant difference in the oxygen concentration as the oxidant is varied.
4. In turn, from this we must conclude that while the sensitizing centers are dependent on the use of the oxidant, they are not due solely to the presence of oxygen.
5. Finally, there is an indication that the film structure may be important to the formation of the sensitizing centers.

## RESULTS

The following results support these conclusions. Since the data are quite extensive we are forced to be very selective in our presentation. We look first at the average chemical composition.

## CHEMICAL COMPOSITION (Table IV)

In this figure we present the average concentrations in atomic percent of the major trace elements as determined by spark source mass spectroscopy. In comparison to the doping levels typical of semiconductors, these values are all very high. As to a systematic variation with the use of the oxidant, one might imagine such a variation for some elements but not for oxygen. The material of the standard film has the PbS structure as shown by X-ray diffraction analysis. No other phase was shown. The analysis method had a sensitivity limit of about 3% by weight which would allow, of course, many minor secondary phases to go unnoticed. Also, the most prospective element for the creation of a second phase, oxygen, is present in a relatively high concentration. If oxygen were present solely as PbO, then its approximately 3 atomic percent concentration would be equivalent to about 6% by weight of a second phase. This would have been detected by X-ray diffraction analysis.

## SURFACE TOPOGRAPHY (Figure 1)

Scanning electron micrographs of the surfaces of the three types of film are shown in Figure 5. Beginning at the top of each picture one sees the film surface followed by a chemically etched edge of the film, and in the foreground the sapphire substrate is evident. The spheres scattered

## UNCLASSIFIED

over the film and the substrate are polystyrene latex particles applied to the film to aid in scale calibration. These spheres are approximately 1.2 microns in diameter.

The films are granular. The size of the grains and their compaction show a systematic variation with the use of the oxidant. A higher oxidant concentration is associated with smaller grains and a looser structure. The spacing of the grains appears to be characterized by a dimension of about  $700\text{\AA}$ .

The next figure (Figure 1a) shows the surfaces of the three types of film as seen in replica electron micrographs. The crystallinity is more apparent in these micrographs and shows very clearly the grain size decreasing with increasing oxidant.

### OXYGEN PROFILE (Figure 2)

Typical profiles of the variation of the concentration of oxygen through the depth of the film is shown in the next figure. The abscissa is the depth into the film from the free surface expressed as a fraction of the thickness of a single coat. Therefore, since the maximum value along the abscissa is 1, the profile for just the outermost coat is given. The ordinate gives the concentration of the oxygen bearing phase expressed as a fraction of all phases present. The baked and not-baked notations on the curves are with reference to a sensitization process used at SBRC. Baking did not alter the profile. The chemical formula of the oxygen phase is not known. There is a high concentration of oxygen at the free surface and also where the initial deposits of a particular coat are located. The high concentration at the film surface is thought to be due to surface adsorption of oxygen while the peak at the interface between coats is thought to be due to the preferential forming of oxides during the initial stages of the chemical deposition or perhaps the effect of surface adsorbed oxygen which might occur at the end of each coat. The pattern is repeated for the inner coats with the exception of the profile for the high oxidant cases. In the high oxidant case the oxygen concentration does not vary in the inner coats but stays constant at the value shown at the right of the graph. Silicon concentration varies in a manner similar to that of oxygen but does not rise to a high value at the free surface.

The profiles, although interesting, appear to play no essential role in photoconductivity.

### $D^*$ AS A FUNCTION OF TEMPERATURE (Figure 3)

The electrical properties of the films are now discussed. First it can be seen how  $D^*$  for the three materials varies as a function of temperature. It is clear that as a detector, the no-oxidant film is very much less effective than the other types. The bulk of the differences in  $D^*$  is due to differences in response; the noise characteristics are apparently quite similar for all three types.

The fact that the curve for the no-oxidant film is distinctly different than the curves for the oxidant types indicates a fundamental difference. That is, the difference in the films does not seem to be a matter of degree but of kind.

## UNCLASSIFIED

### SPECTRA (Figure 4)

The suggestion of the difference of kind is also seen in the response and absorption spectra. In this graph the absorption curves are at the top, and response on the bottom. The absorption data are for room temperature conditions; the response data are for a temperature of 193°K and for a chopping frequency of 1100 Hz. The response spectra of the standard and high-oxidant films are similar to each other and also quite different than that of the no-oxidant film. The oxidant materials maintain their response out to high photon energies but the response of the no-oxidant type drops off with photon energy. The low energy cutoffs of the absorption spectral also single out the no-oxidant material as being distinct. The no-oxidant material alone has a sharp low energy cutoff.

In the no-oxidant spectra, a difference in the absorption and response cutoff energies is especially noticeable. A partial explanation for this difference may be found in the temperature dependence of the band gap of PbS. The band gap energy shifts from 0.41 eV to about 0.36 eV when PbS is cooled from room temperature to 193°K. But these values for the band gap energies do not match the cutoff energies nor is their difference as large as needed.

Redfield and Wittke<sup>1</sup> have discussed the response spectra of heavily doped but nearly compensated material. Our materials would seem to fit such a case. They are heavily doped with many trace elements and yet their free carrier densities are far less than what would be expected from the contribution of any one dopant. The typical response spectrum as presented by Redfield and Wittke is similar to that of the no-oxidant film. Local potential variations arising out of the random distribution of dopants are assumed to be responsible for the spectrum shape. The potential variations produce a tailing of the band edges into the forbidden gap, and hence, soften the cutoff of the absorption. There is also a reduction in mobility and an increase in the relaxation time. Photoconductivity is enhanced by the separation of carrier types through the trapping effect of the potential variations. The more energetic carriers will be less affected by the potential variations, and thus life time will decrease as the photon energy of the excitation is increased.

The absorption spectra of the oxidant type films show a soft cut-off which might be associated with potential wells. On the other hand, the response spectrum of the no-oxidant material seems generally to fit what is expected for compensated material at high doping levels. However, the low-energy cutoff is not smaller than the band gap of PbS as one would expect from a tailing of the band edges. This discrepancy may indicate that the band gap of the material has been widened by the influence of oxygen. Perhaps the film is a PbSO system having a band gap which represents an interpolation between that of PbS and PbO. Such a blending of properties is not uncommon when it is possible to form the mixed system.

An important result is that the magnitude of the absorption coefficient is roughly independent of the use of an oxidant while the magnitude of the photoreponse is not. Apparently, the major

---

<sup>1</sup>D. Redfield and J. P. Wittke, "Energy Band Tails and Photoconductivity," Proc. of the Third International Conference on Photoconductivity, Stanford, August 12-15, 1969. Edited by E. M. Pell, Pergamon Press 1971, pp. 29-33.

## UNCLASSIFIED

differences in detector characteristics of the three film types are to be explained in terms of free carrier lifetime. This is consistent with a model of photoconductivity that is based on sensitizing centers which are present only in the oxidant materials.

The noticeable differences in the cutoff points of the response curves for the three types of films suggest, however, that significant physical differences exist in the film types. The only known physical differences are those of structure; a loose structure is effected by the use of an oxidant. In this regard it is interesting to note that very thin films of the standard material showed  $D^*$  values comparable to what would be expected by a scaling of thicker films. These thin films were so thin that islands were formed by the individual grains resulting in a high resistance of the films. Apparently, there is little danger of making the films with too loose a structure.

### SPECTRA (Figure 4a)

The next figure shows the same data presented from a device point of view plotting responsivity and absorption versus wavelength.

### CARRIER DENSITIES AND HALL MOBILITIES AS A FUNCTION OF TEMPERATURE (Figure 5)

Figure 5 shows the behavior of carrier density and mobility as a function of reciprocal temperature as determined by Hall measurements. The materials are all p-type as indicated by the carrier density symbol. There are two distinct regions for both the mobility and carrier density curves. Exciting the films raises the curves as shown by the dashed lines. However, the no-oxidant film shows very little change upon photoexcitation, and the dashed curves represent both the light and dark conditions for the no-oxidant film. The activation energies for the standard film when in the dark in the high-temperature region is 0.14 eV for carrier density and 0.09 eV for mobility.

### DECAY TIME AS A FUNCTION OF TEMPERATURE (Figure 6)

The decay time of photoconductivity for the standard film is shown in Figure 6. These data are given as a function of temperature with excitation intensity as a varied parameter. The excitation was from a tungsten incandescent lamp and a light value of 1.00 corresponds to 100 mwatt/cm<sup>2</sup> at the detector.

It is clear that photoconductivity is quenched at the higher temperatures. The activation energy for quenching is about 0.23 eV. If these results are interpreted in terms of sensitizing centers, then the sensitizing centers must lie about 0.23 eV below the conduction band.

The dashed curves, which are included for comparison, indicate calculated lifetimes for 2.6- and 2.3-micron radiation. As to be expected, the lifetime curves also show thermal quenching.

## UNCLASSIFIED

### BAND PICTURE OF A MODEL FOR PbS (Figure 7)

The electronic and photoelectronic data led Professor Bube to propose the model for the photoconductivity of lead sulfide as shown in Figure 7. The energy levels for two cases are shown. In the upper diagram it is assumed that the barriers are wide and all carriers must go over them if conduction is to take place. In the lower diagram, the barriers are considered to be thinner and tunneling may occur. Photoexcitation lowers the Fermi level, and thus increases the effective conductivity of the barriers in proportion to the increased number of carriers in the grains between the barriers. The barrier height determines the dark conductivity activation energy as suggested many years ago by Petritz. The acceptors determine the low-temperature behavior of the carrier density.

### OXYGEN ADSORPTION (Figure 8)

In our final figure we show the effects of oxygen adsorption on the conductivity of the standard material. Both light and dark conductivity are shown for two cases of exposure to oxygen. In one case, the upper curve which is dashed, the sample was continuously exposed to 100 mwatt/cm<sup>2</sup> radiation from a tungsten lamp. Dark measurements were made by temporarily turning off the lamp. In the second case, the lower solid curve, the sample was in the dark except to make a light measurement in which case the tungsten lamp was turned on. It is obvious that the illumination accelerates oxygen adsorption. This figure represents but a small portion of the data taken on oxygen adsorption.

Some of the other important results are as follows. (Table V)

1. The effects are reversible.
2. The initial conductivity state as determined by heat treating effects the sensitivity to oxygen adsorption.
3. Of the three films, the standard film is the least sensitive to oxygen adsorption.
4. Thinner films, that is, films of one or two coats, are more sensitive to oxygen adsorption than four coat films.
5. Oxygen adsorption during monochromatic illumination has a spectrum which follows the optical absorption spectrum.
6. The no-oxidant material cannot be made sensitive by either oxygen adsorption or desorption.

### CONCLUSION (Table III)

Although the investigation has been officially completed, the data are continuing to provide new insights. As of now, these conclusions represent the major findings of the program.



# UNCLASSIFIED

TABLE I. TYPES OF P6S FILMS INVESTIGATED (U)  
(Unclassified)

NO-OXIDANT	DEPOSITED WITHOUT THE USE OF AN OXIDANT 1, 2, AND 4 COATS
STANDARD	OXIDANT USED AT THE USUAL CONCENTRATION 1, 2, AND 4 COATS
HIGH-OXIDANT	OXIDANT USED AT A CONCENTRATION 4 TIMES THE USUAL 1, 2, AND 4 COATS

TABLE II. TABLE OF INVESTIGATIVE TECHNIQUES (U)  
(Unclassified)

## ANALYSES

COMPOSITION AND STRUCTURE	METHOD
1. TRACE IMPURITIES	SPARK SOURCE MASS SPECTROSCOPY A. J. SOCHA, BELL AND HOWELL RESEARCH LABORATORIES
2. CRYSTAL STRUCTURE	X-RAY DIFFRACTION AND FLUOR- ESCENCE R. D. SLOAN AND W. A. GARDNER SLOAN RESEARCH INDUSTRIES
3. SURFACE TOPOGRAPHY	REPLICA AND SCANNING ELECTRON MICROSCOPY R. D. SLOAN AND W. A. GARDNER SLOAN RESEARCH INDUSTRIES M. H. RITCHIE NAVAL WEAPONS CENTER, CHINA LAKE
4. DEPTH PROFILES AND TRACE IMPURITIES	SPUTTER-ION SOURCE MASS SPECTROSCOPY F. G. SATKIEWICZ GCA TECHNOLOGY DIVISION
ELECTRONIC PROPERTIES	METHOD
5. ABSORPTION AND RESPONSE SPECTRA	OPTICAL SPECTROSCOPY P. J. SCHREIBER SANTA BARBARA RESEARCH CENTER
6. PHOTOELECTRONIC PROPERTIES	HALL AND THERMOELECTRIC MEAS- UREMENTS AS A FUNCTION OF EXCITATION AND TEMPERATURE
7. OXYGEN ADSORPTION AND HEAT TREATMENT EFFECTS	R. H. BUBE, S. ESPEVIK AND CHEN-HO WU STANFORD UNIVERSITY

# UNCLASSIFIED

TABLE III. LIST OF CONCLUSIONS (U)  
(Unclassified)

1. STRUCTURE AND ELECTRICAL PROPERTIES ARE TYPICAL OF GRAINY MATERIALS WITH INTERGRAIN BARRIERS.
2. PHOTSENSITIVITY MAY BE EXPLAINED IN TERMS OF SENSITIZING CENTERS WITHOUT REFERENCE TO THE BARRIERS.
3. AVERAGE CONCENTRATION OF OXYGEN WITHIN THE FILM IS NOT CONTROLLED BY THE USE OF THE OXIDANT.
4. THE SENSITIZING CENTERS ARE NOT DUE SOLELY TO THE PRESENCE OF OXYGEN.
5. STRUCTURE MAY BE IMPORTANT TO THE FORMATION OF SENSITIZING CENTERS.

TABLE IV. CHEMICAL COMPOSITION (U)  
(Unclassified)

AVERAGE CONCENTRATIONS IN ATOMIC PERCENT OF  
MAJOR TRACE ELEMENTS IN PbS FILM

FILM TYPE	MAJOR TRACE ELEMENTS					
	C	Ca	H	N	O	Si
NO-OXIDANT	0.92	0.020	0.52	0.92	2.9	0.38
STANDARD	0.76	0.013	0.44	0.44	2.9	0.68
HIGH-OXIDANT	0.44	0.56	0.36	0.56	2.1	0.68

UNCLASSIFIED



No-Oxidant Type



Standard ITO Type



High-Oxidant Type

FIGURE 1. SURFACE TOPOGRAPHY. Scanning electron micrographs of PbS films. Surface and edge features are viewed at  $45^\circ$  with latex spheres included as a scale reference. (Sloan Research Industries) (U) (Unclassified)



No-Oxidant Type



Standard Type



High-Oxidant Type

FIGURE 1a. REPLICA ELECTRON MICROGRAPHS. Three types of PbS film at moderate magnification showing gross surface features. (Sloan Research Industries) (U) (Unclassified)

UNCLASSIFIED

UNCLASSIFIED

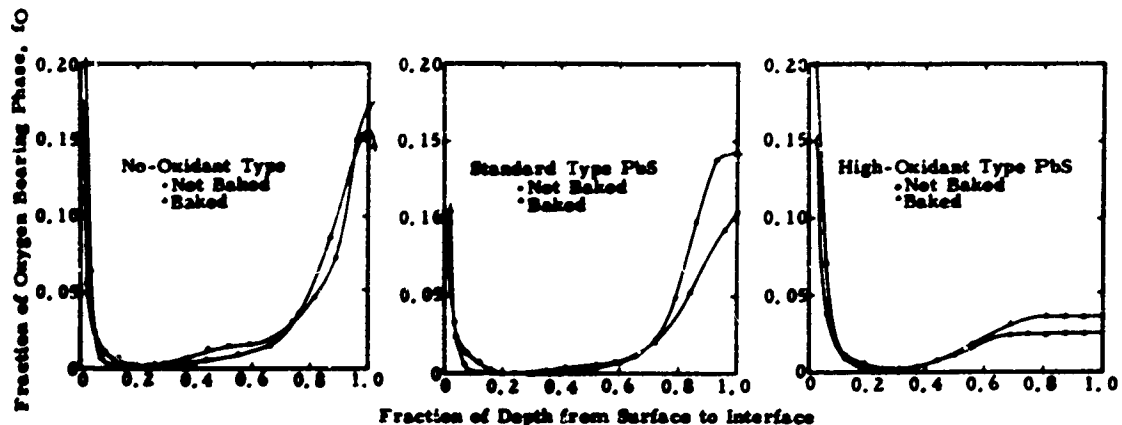


FIGURE 2. OXYGEN PROFILE. Profiles of oxygen distribution in the no-oxidant, standard, and high-oxidant type materials by ion probe analysis based on the  $Pb^+/S_2^+$  intensities. (GCA Technology Division) (U) (Unclassified)

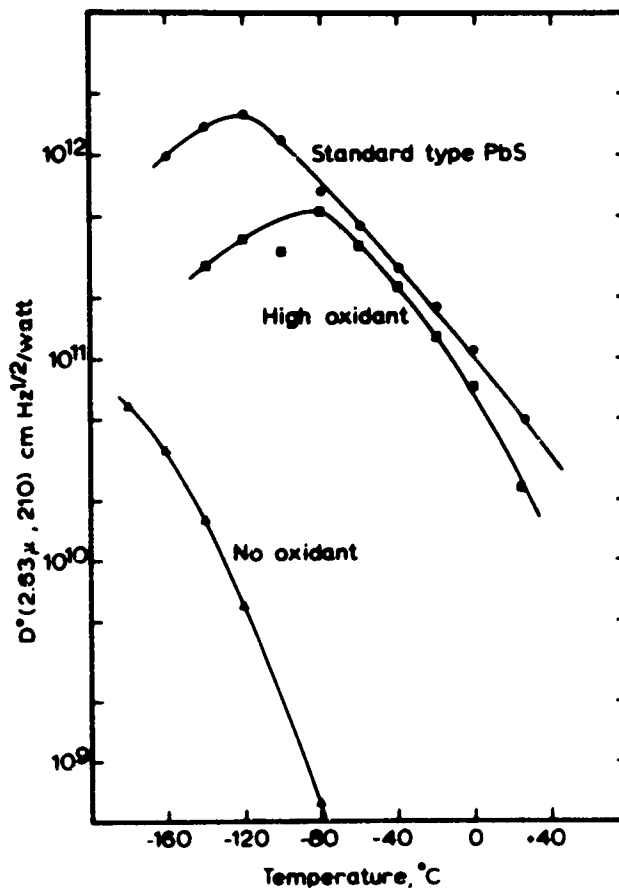


FIGURE 3.  $D^*$  VERSUS TEMPERATURE. Detectivity versus temperature under cold background conditions for the standard, the no-oxidant, and the high-oxidant PbS films. (U) (Unclassified)

UNCLASSIFIED

UNCLASSIFIED

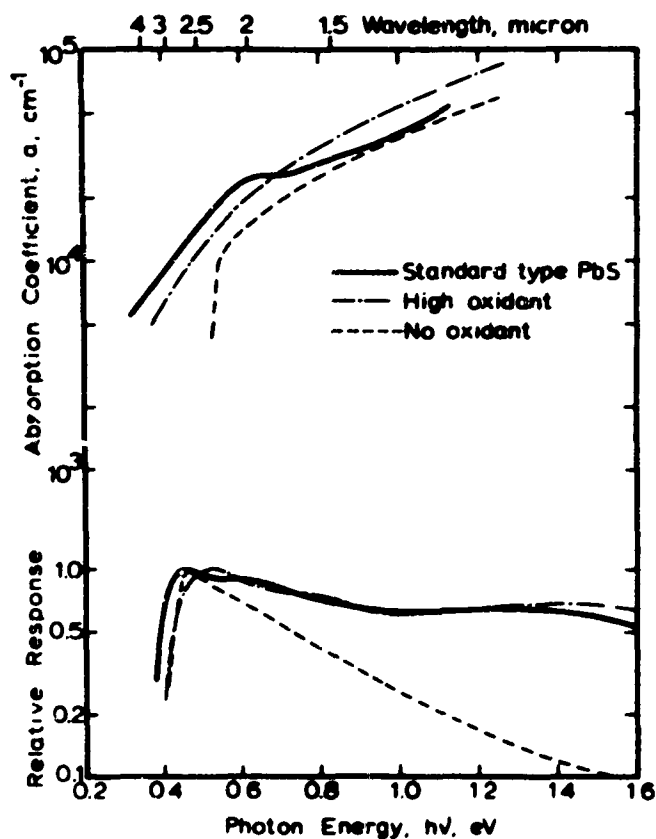


FIGURE 4. SPECTRA. Spectral response and optical absorption as a function of photon energy (on an equal energy basis). (U)  
(Unclassified)

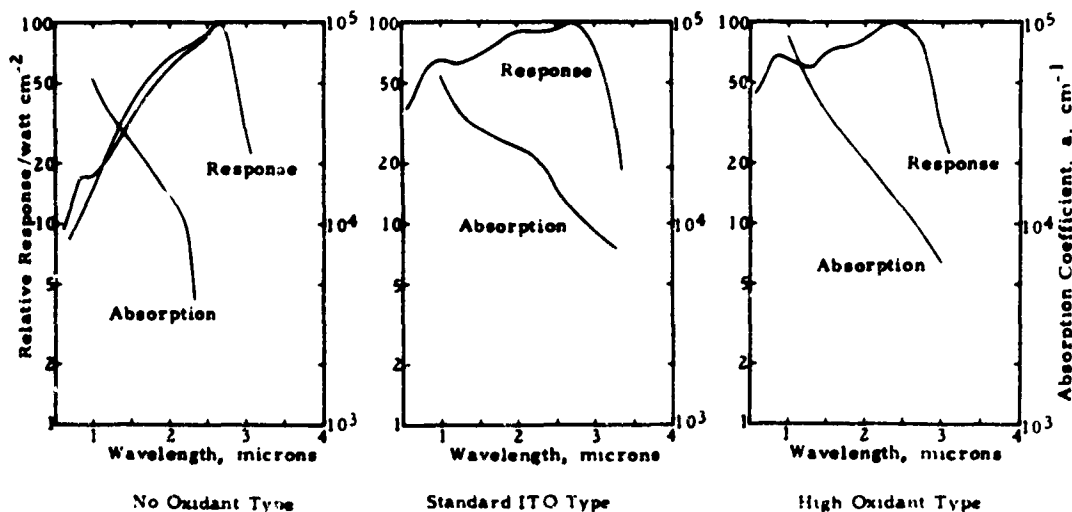


FIGURE 4a. SPECTRA AS A FUNCTION OF WAVELENGTH. Spectral response and optical absorption as a function of wavelength (on an equal energy basis). The spectral response is given for  $-80^\circ\text{C}$  and 1100 Hz normalized to peak response. The optical absorption is given for  $+25^\circ\text{C}$ . (U)  
(Unclassified)

UNCLASSIFIED

UNCLASSIFIED

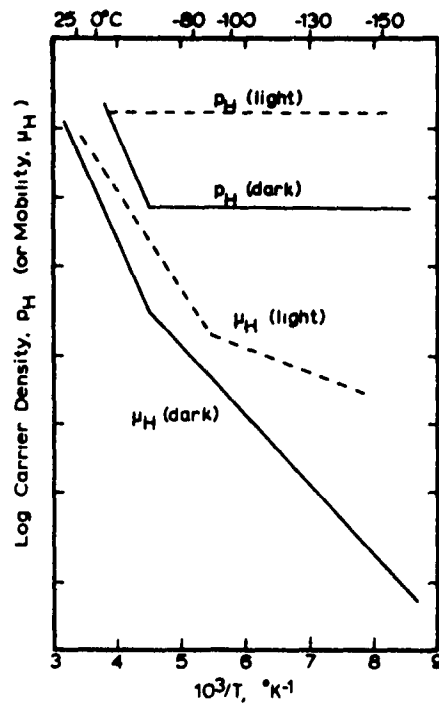


FIGURE 5.  $p_H$  AND  $\mu_H$  VERSUS  $1/T$ . Typical behavior of the temperature dependencies of carrier density and Hall mobility for photosensitive PbS films. (U)  
(Unclassified)

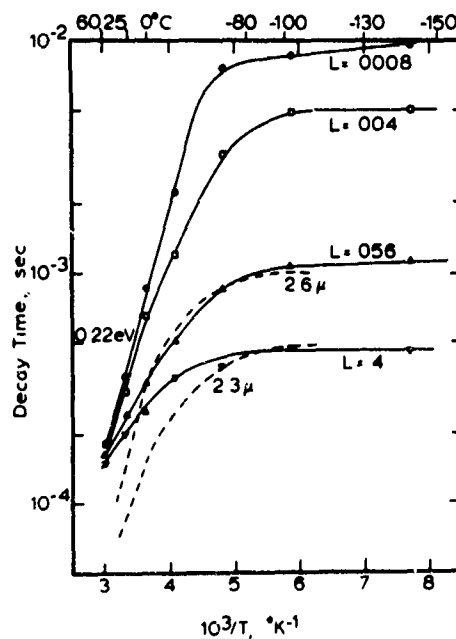
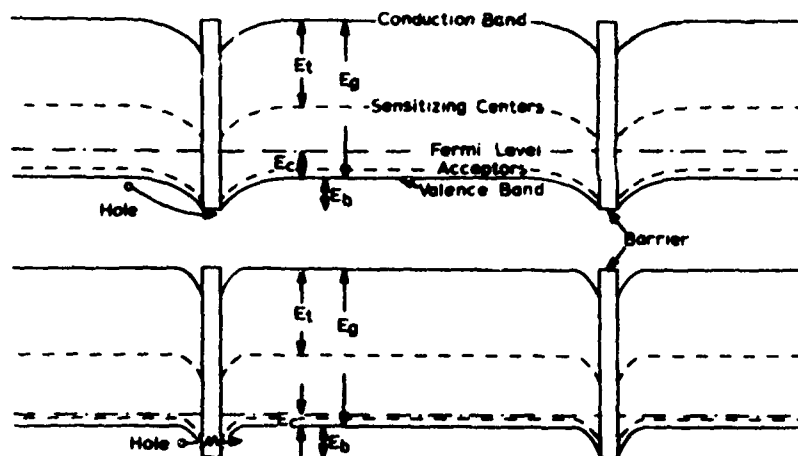


FIGURE 6. DECAY TIME VERSUS  $1/T$ . Temperature dependence of the measured decay time of photoconductivity for the standard film. Different values of excitation intensity are given by  $L$  in units of  $100 \text{ mw/cm}^2$ . Dashed curves indicate the calculated lifetimes from data for excitation by  $2.6\text{-}\mu\text{m}$  and  $2.3\text{-}\mu\text{m}$  radiation. (Stanford University) (U)  
(Unclassified)

UNCLASSIFIED

# UNCLASSIFIED

(a) Large Depletion Layer Widths



(b) Small Depletion Layer Widths

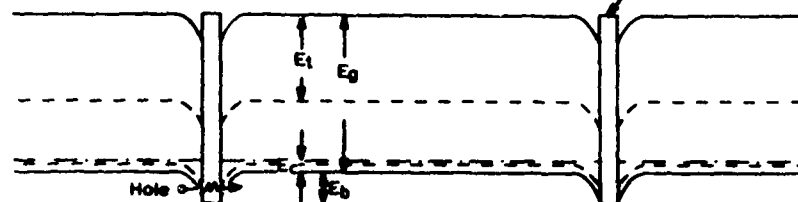


FIGURE 7. BAND PICTURE OF MODEL. Energy levels in PbS photoconductors as proposed by Bube and co-workers. a) For large depletion layer widths associated with intergrain barriers, and b) for small depletion layer widths.  $E_t$  is the energy required to empty a sensitizing center,  $E_c$  is the height of the Fermi level above the valence band,  $E_g$  is the bandgap, and  $E_b$  is the intergrain barrier height. (Stanford University) (U)

(Unclassified)

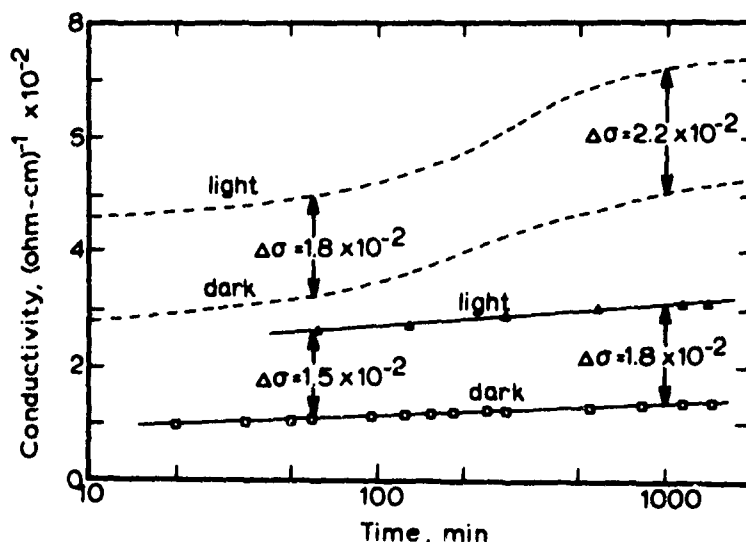


FIGURE 8. OXYGEN ADSORPTION. Variation of light and dark conductivity with time after exposure to air for the standard four-coat PbS film. Dashed curve is for data taken after a previous fix for 66 hours at  $72^\circ\text{C}$  at  $2 \times 10^{-2}$  Torr; measured under photoexcitation with occasional reading of dark conductivity. Solid curve is after a fix for 88 hours at  $78^\circ\text{C}$  at less than  $10^{-3}$  Torr; measured under dark conditions with occasional photoexcitation. All data were taken at room temperature and the excitation, which was from a tungsten lamp, provided about  $100 \text{ mw/cm}^2$  at the sample. (Stanford University) (U)

(Unclassified)

# UNCLASSIFIED

TABLE V. OTHER IMPORTANT RESULTS (U)  
(Unclassified)

1. THE EFFECTS ARE REVERSIBLE.
2. THE INITIAL CONDUCTIVITY STATE AS DETERMINED BY HEAT TREATING EFFECTS THE SENSITIVITY TO OXYGEN ADSORPTION.
3. OF THE THREE FILMS, THE STANDARD FILM IS THE LEAST SENSITIVE TO OXYGEN ADSORPTION.
4. THINNER FILMS, THAT IS, FILMS OF ONE OR TWO COATS, ARE MORE SENSITIVE TO OXYGEN ADSORPTION THAT FOUR COAT FILMS.
5. OXYGEN ADSORPTION DURING MONOCHROMATIC ILLUMINATION HAS A SPECTRUM WHICH FOLLOWS THE OPTICAL ABSORPTION SPECTRUM.
6. THE NO-OXIDANT MATERIAL CANNOT BE MADE SENSITIVE BY EITHER OXYGEN ADSORPTION OR DESORPTION.



# UNCLASSIFIED

.... This paper is UNCLASSIFIED

## OPTICAL MEASUREMENTS ON PbSnTe (Unclassified)

A. Lockwood and H. Levinstein  
Syracuse University  
Syracuse, N.Y.

### ABSTRACT (Unclassified)

The temperature dependence of the  $\text{Pb}_{1-x}\text{Sn}_x\text{Te}$  energy gap has been determined by optical transmission measurements. The measured samples have compositions of 9, 12, 16, 17, and 25 per cent SnTe and carrier concentrations ranging from  $9.0 \times 10^{15} \text{ cm}^{-3}$  to  $2.0 \times 10^{19} \text{ cm}^{-3}$ . For low carrier concentration samples, the variation of the energy gap is in good agreement with pseudopotential calculations for PbTe. However, some samples exhibit a negative  $dE/dT$  at temperatures less than approximately 30 K. For samples with high carrier concentrations, greater than approximately  $5.0 \times 10^{18} \text{ cm}^{-3}$ , the measured gap is shifted (Burstein-Moss effect) to lower wavelengths.

This paper will deal with the determination of the  $\text{Pb}_{1-x}\text{Sn}_x\text{Te}$  energy gap as a function of temperature. Numerous measurements of the  $\text{Pb}_{1-x}\text{Sn}_x\text{Te}$  energy gap have already been made at various temperatures and compositions. These previous measurements have included determinations from photovoltaic cutoffs (1), laser emission wavelength (2-5), transmission (6-9), and, in the case of pure SnTe, tunneling experiments (10). Dixon and Bis (11) summarized a large number of these measurements, and this summary is presented in figure 1. For values of  $x$  less than approximately 0.35, the temperature coefficient of the energy gap is seen to be positive, but for SnTe it is negative. This is in apparent agreement with the band inversion model proposed by Dimmock et al. (3).

This model is represented schematically, for a temperature of 12 K, in figure 2. According to this model, the valence and conduction bands of PbTe are  $L_6^+$  and  $L_6^-$  states respectively. As the percentage of SnTe is increased in the alloy,  $E_g$  decreases as the states approach, and becomes zero at some intermediate composition. As the tin content is increased further, the states interchange, with the  $L_6^-$  now the valence band and the  $L_6^+$  the conduction band.

This model implies that, for a composition between 0.35 and 0.60, as the temperature is decreased from room temperature toward 0 K, the gap should decrease, go to zero at some intermediate temperature, and then increase as the temperature is decreased further. This behavior can be represented in figure 1 as a vertical transition from the 300 K curve to the 12 K curve for  $0.35 < x < 0.60$ . However, for compositions greater than approximately 35 per cent SnTe the alloys are largely nonstoichiometric (metal deficient), and with hole concentrations much in excess of  $10^{19} \text{ cm}^{-3}$ , the absorption is prohibitively high for transmission measurements on bulk material.

Band inversion has not been observed directly in  $\text{Pb}_{1-x}\text{Sn}_x\text{Te}$  alloys. It has however, been observed by Strauss (12) in the PbSnSe system, which has essentially the same band structure as PbSnTe. The band inversion model is also supported by measurements of electrical resistivity as a function of temperature (11). These resistivity measurements show a distinct break in an otherwise linear dependence upon temperature. The temperatures of these breaks are in agreement with band crossing temperatures predicted on the basis of the band inversion model.

# UNCLASSIFIED

Although the range  $0.35 < X < 0.60$  is especially interesting, crystals previously grown were for compositions of less than 30 per cent SnTe. Available material was then a restriction on our measurements. We have measured the energy gap as a function of temperature for more than ten samples of various compositions and carrier concentrations. Figure 3 shows the results of one of our experiments.

The sample is a single crystal section from a zone levelled ingot grown and annealed at Syracuse. The polished crystal was mounted on an aluminum aperture in a variable temperature cryostat. The aluminum substrate has almost the same temperature coefficient of expansion as the Pb-Sn-Te alloy (13), and therefore eliminates any strain effects in the sample. Figure 3 shows that the energy gap as a function of temperature is non-linear; for temperatures greater than approximately 50 K there is a slight negative curvature; and, for temperatures less than approximately 30 K there is almost no change in the band gap. These results are in contrast to those of Tauber and Cadoff (9) who observed a linear variation of the energy gap for temperatures below 350 K (for  $X=0.07$  and  $0.15$ ).

For non-degenerate semiconductors, most of the variation in the energy gap with temperature is believed to come from two mechanisms: overall crystal expansion or contraction (i.e. a variation in the lattice constant with temperature), and the thermal motion of the ion cores (Debye-Waller effect) (14). The non-linearity seen below approximately 30 K probably arises from a non-linearity of the expansion coefficient in this temperature region. For temperatures less than approximately 80 K, the coefficient of thermal expansion of PbTe becomes non-linear, approaching zero as the temperature decreases (15). For very low temperatures the lattice expansion effectively dominates the temperature dependence of the energy levels since the Debye-Waller displacements are small (16). The temperature dependence of the band gap then follows that of the expansion coefficient. The Debye-Waller effect becomes non-negligible before the thermal expansion coefficient becomes linear and imparts the curvature to the 50 to 300 K region.

Figure 4 shows a lower composition, n-type sample. This sample is from an annealed section of a Czochralski grown crystal obtained from Bell and Howell. The variation of  $dE/dT$  is qualitatively the same as seen in the p-type, lower carrier concentration sample. The effect of the thermal expansion coefficient at low temperatures as seen in the transmission data of figures 3 and 4 has been confirmed by an experiment by Norton et al. (5) on a  $Pb_{1-x}Sn_xTe$  diode laser (figure 5).

Varshni (14) has proposed a relation for the variation of the energy gap with temperature. The equation given by Varshni is presented in figure 6 with a corresponding least-squares fit to a set of our data. This model is based on the well founded assumptions that the thermal expansion coefficient is linear down to some relatively low temperature, and that the Debye-Waller effect is the major contributor at high temperatures. These assumptions lead to

$$\begin{aligned}\Delta E_g &= T^2 \text{ for } T \ll \theta_D \\ \Delta E_g &= T \text{ for } T \gg \theta_D\end{aligned}$$

where  $\theta_D$  is the Debye temperature. Although  $E_g = E_0 + \alpha T^2 / (\theta + T)$  satisfactorily represents experimental data for Si, Ge, GaAs, InP, and others, the values of the  $\theta$  parameter do not correlate very well with measured Debye temperatures, being only within a factor of 2.5 for those semiconductors fit by Varshni. For PbTe, reported values of  $\theta_D$  vary from 115 K, at 180 K (17), to 177 K, at 0 K (15). For SnTe,  $\theta_D$  varies from 130 K, at 80 K (18), to 141 K, at < 1 K (19). Assuming similar values of  $\theta_D$  for  $Pb_{1-x}Sn_xTe$ , the value of 11.0 determined by the fitting process is off by more than an order of magnitude. Other samples fit to Varshni's relation give  $\theta$  parameters ranging from 6 to 133. Varshni's  $\theta$  parameter then does not correlate at all with the Debye temperature as it should. More powerful calculations of the temperature dependence of the energy gap are therefore necessary.

## UNCLASSIFIED

A recent calculation of the temperature dependence of the band gap for PbTe has been done by Tsang and Cohen (20). This calculation involves a modified empirical pseudopotential technique. In figure 7, the results of Tsang and Cohen's pseudopotential calculation have been translated along the energy axis to coincide with our data from figure 6. This is done to show the agreement of the respective  $dE/dT$ 's. The high temperature region is in excellent agreement with the calculated  $dE/dT$  for PbTe. The calculation also indicates a small deviation from linearity at low temperature.

Figure 8 compares our measured values of  $dE/dT$  for several compositions with the corresponding values of Tsang and Cohen. On this basis it appears that for greater than 10 per cent SnTe,  $dE/dT$  increases with increasing SnTe in the alloy.

Several samples that we have measured do not show the expected temperature dependence that has so far been discussed. These results are shown collectively in figure 9. For temperatures less than approximately 30 K these samples exhibit a negative  $dE/dT$ . The compositions of these samples are 9, 16, and 25 per cent SnTe with carrier concentrations of  $-3.3 \times 10^{17}$ ,  $+9.0 \times 10^{15}$ , and  $+4.6 \times 10^{16} \text{ cm}^{-3}$  respectively. For the three n-type samples we have measured with compositions of 9 per cent SnTe, only the one with a carrier concentration of  $-3.3 \times 10^{17} \text{ cm}^{-3}$  has had a change in sign of  $dE/dT$ . The other 9 per cent samples have had lower ( $-4.9 \times 10^{16} \text{ cm}^{-3}$ ) and higher ( $-4.0 \times 10^{18} \text{ cm}^{-3}$ ) carrier concentrations. On the basis of these three samples with  $X=0.09$ , we conclude that this low temperature "dip" is not a function of carrier concentration. Two of the 9 per cent SnTe samples are shown in figure 10 for comparison, the third sample (RT8, shown in figure 4) is almost coincident with RT6, and, for clarity, is not included. Since we have also measured samples of 16 and 17 per cent SnTe that show no "dip", we conclude that the sign reversal of  $dE/dT$  is probably also independent of composition. The behavior of these samples is then possibly due to either an impurity effect or large inhomogeneities. Whether the reversal in sign of  $dE/dT$  is a manifestation of band inversion is open to considerable speculation.

We have very recently observed a second unusual temperature dependence of the band gap in the PbSnTe alloy system. These transmission measurements have been made on unannealed material, polished and etched to thicknesses of less than 50  $\mu\text{m}$ . In figure 11 we compare two samples cut from the same slice of zone levelled material; one annealed down to a carrier concentration of  $+4.6 \times 10^{16} \text{ cm}^{-3}$ , the other unannealed ( $+1.6 \times 10^{19} \text{ cm}^{-3}$ ). The large shift of the measured optical gap of the unannealed material is due to the Burstein-Moss effect. A second, similar comparison is shown in figure 12 where energy is plotted against temperature for an unannealed sample of  $\text{Pb}_{0.83}\text{Sn}_{0.17}\text{Te}$ . The variation of the long wavelength cutoff of a photovoltaic detector fabricated from the same slice of vapor grown material (21) is also plotted in figure 12. Again a large Burstein-Moss shift is observed for the unannealed material.

Hall measurements as a function of temperature are currently being performed on all the samples we have measured optically. Magneto-optical experiments are planned for the future. It is hoped that a correlation of the optical and electrical data will result in a better understanding of the basic properties of the PbSnTe alloy system.

We would like to thank the Air Force Avionics Laboratory at Wright Patterson Air Force Base, Ohio for supporting our work, and in particular, our project monitor, T. Pickenpaugh.

# UNCLASSIFIED

## REFERENCES

1. I. Melngailis and A. R. Calawa, Appl. Phys. Letters 9, 304 (1966).
2. J. F. Butler, A. R. Calawa, R. J. Phelan, Jr., T. C. Harman, A. J. Strauss, and R. H. Rediker, Appl. Phys. Letters 5, 75 (1964).
3. J. O. Dimmock, I. Melngailis, and A. J. Strauss, Phys. Rev. Letters 26, 1193 (1966).
4. J. F. Butler, A. R. Calawa, and T. C. Harman, Appl. Phys. Letters 9, 427 (1966).
5. P. Norton, P. Chia, T. Braggins, and H. Levinstein, Appl. Phys. Letters 18, 158 (1971).
6. P. M. Nikolic, Brit. J. Appl. Phys. 16, 1075 (1965).
7. R. N. Tauber, A. A. Machonis, and I. B. Cadoff, J. Appl. Phys. 37, 4855 (1966).
8. P. M. Nikolic, Brit. J. Appl. Phys. 18, 897 (1967).
9. R. N. Tauber and I. B. Cadoff, J. Appl. Phys. 38, 3714 (1967).
10. L. Esaki and P. J. Stiles, Phys. Rev. Letters 16, 1108 (1966).
11. J. R. Dixon and R. F. Bis, Phys. Rev. 176, 942 (1968).
12. A. J. Strauss, Phys. Rev. 157, 608 (1967).
13. C. M. Chapman, J. W. Moody, G. Kramer, and J. F. Miller, Investigation of PbTe-SnTe single-crystal material for use in detectors of 8 to 14-micron radiation, Fourth Interim Technical Report, NVL Contract DA-44-009-AMC-1724(E), p. 6 (July 21, 1967).
14. Y. P. Varshni, Physica 34, 149 (1967).
15. B. Houston, R. E. Strakna, and H. S. Bilson, J. Appl. Phys. 39, 3913 (1968).
16. Y. W. Tsang, private communication.
17. D. H. Parkinson and J. E. Quarrington, Phys. Soc. Proc. A67, 569 (1954).
18. P. V. Gul'tayayev and A. V. Petrov, Soviet Phys. - Solid State 1, 330 (1959).
19. L. Finegold, J. K. Hulm, R. Mazelsky, N. E. Phillips, and B. B. Triplett, in Low Temperature Calorimetry Conference, 1966 Proceedings (Ser. A, VI. Physica. Ed. by O. V. Lounasmaa), p. 129.
20. Y. W. Tsang and M. L. Cohn, Phys. Rev. B 3, 1254 (1971).
21. Both unannealed material and detector were obtained from Paul Chia, Barnes Engineering.

UNCLASSIFIED

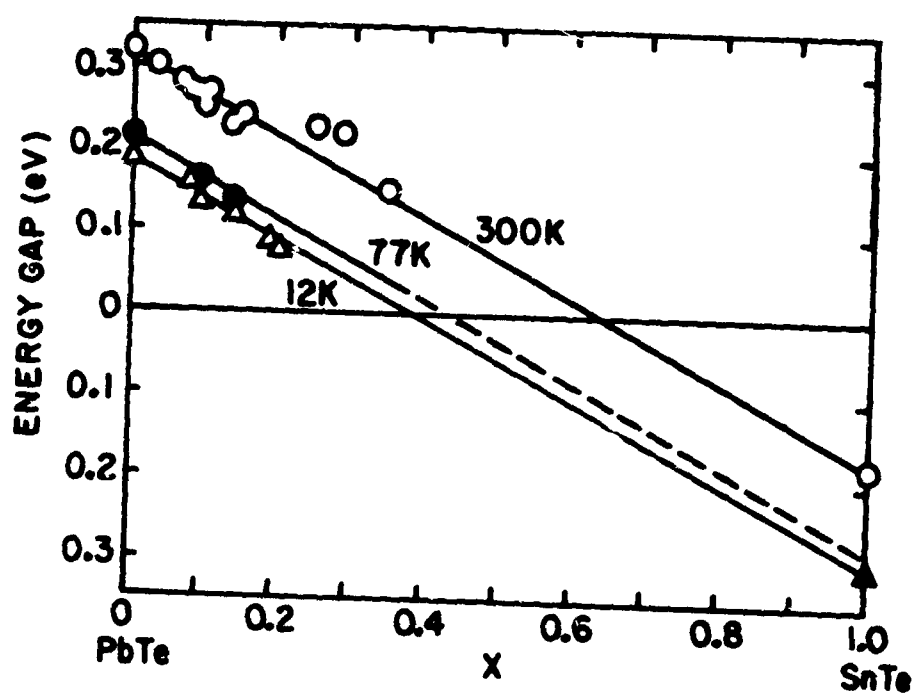


FIGURE 2

UNCLASSIFIED

UNCLASSIFIED

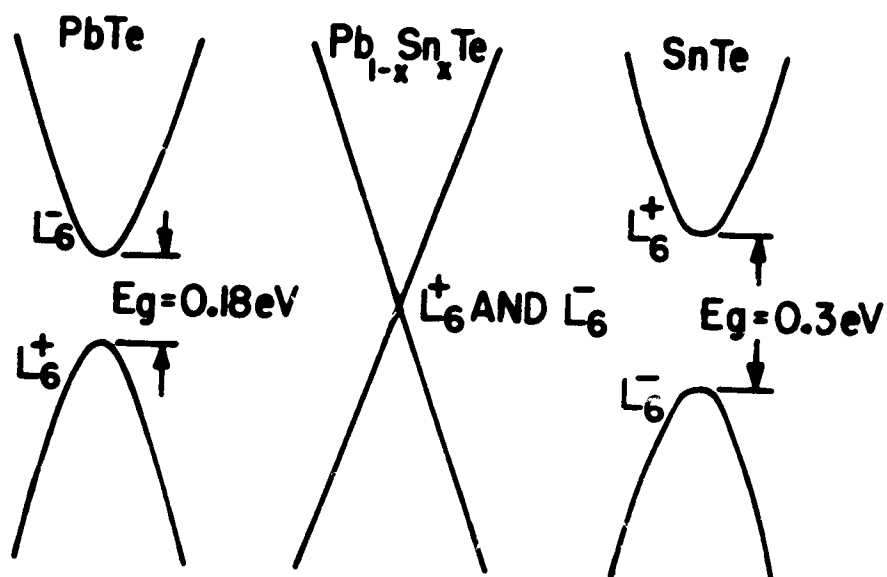


FIGURE 1.

UNCLASSIFIED

UNCLASSIFIED

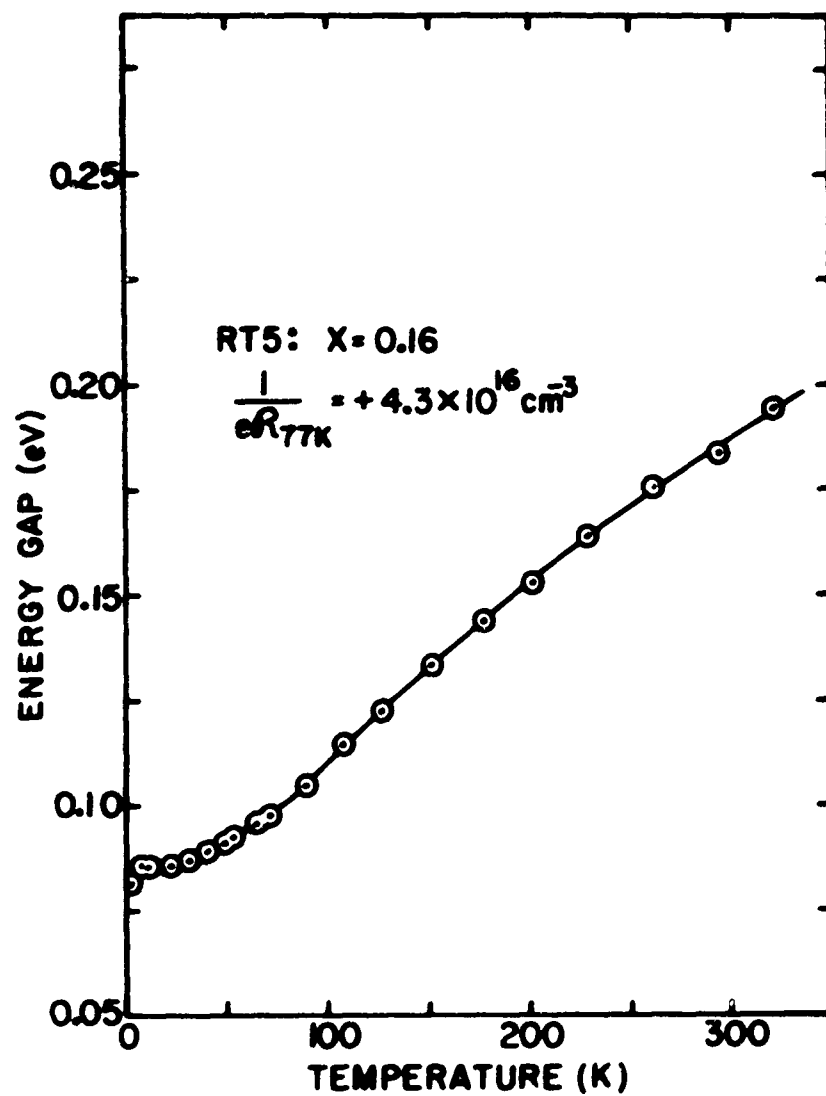


FIGURE 3

UNCLASSIFIED

UNCLASSIFIED

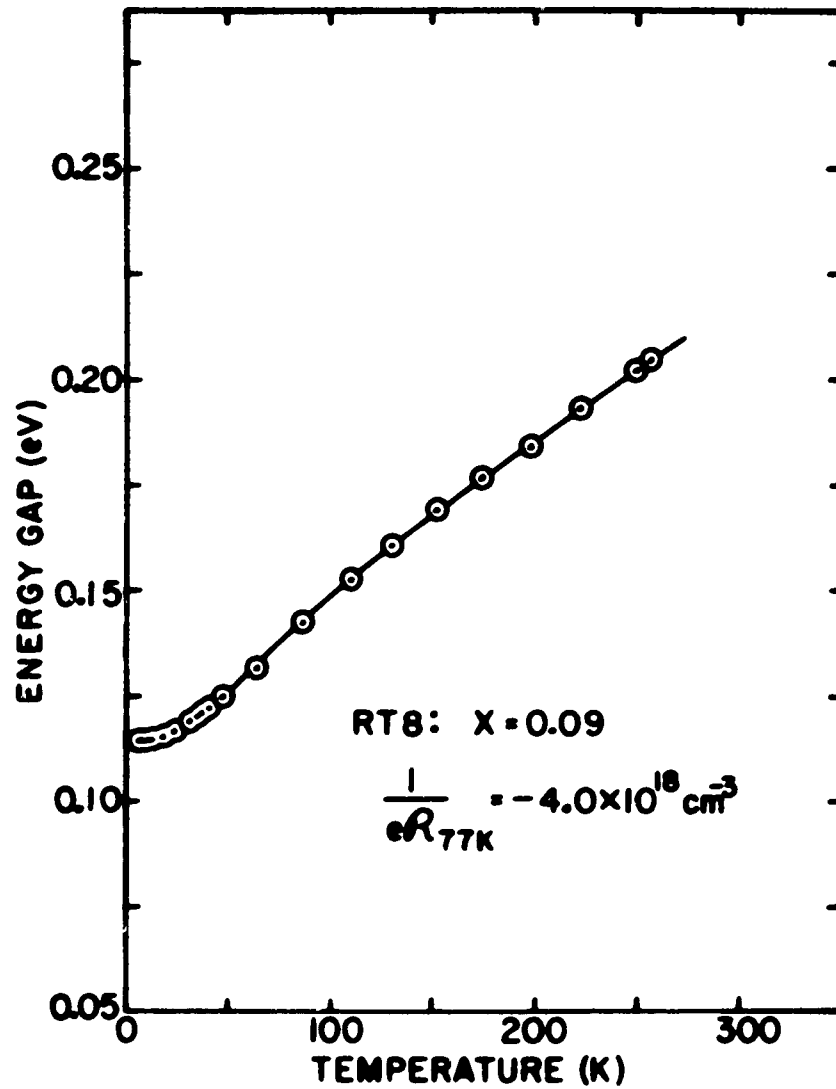


FIGURE 1

UNCLASSIFIED



UNCLASSIFIED

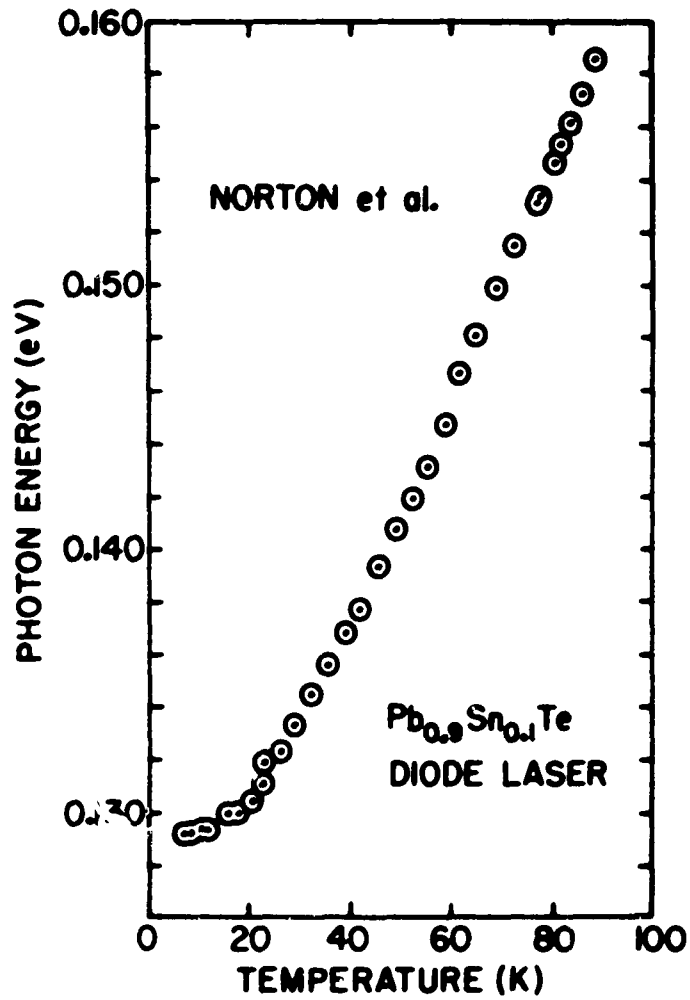


FIGURE 1

UNCLASSIFIED

UNCLASSIFIED

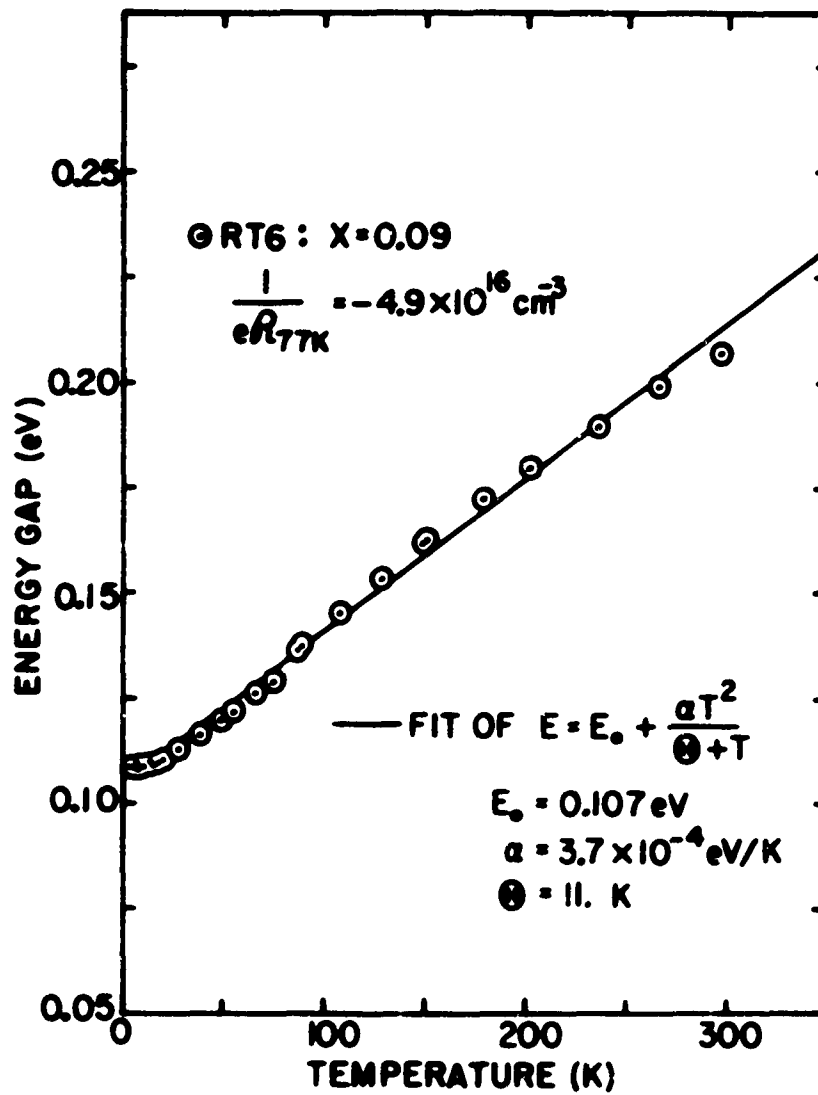


FIGURE 5

UNCLASSIFIED

UNCLASSIFIED

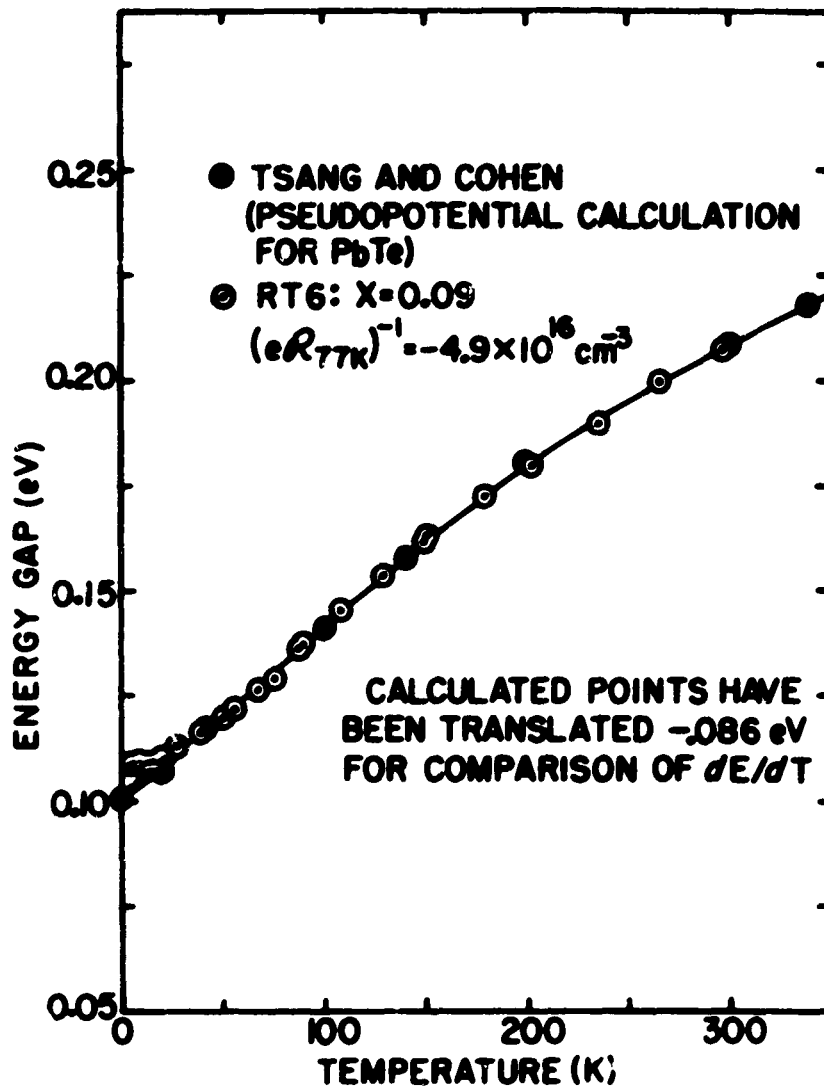


FIGURE 1

UNCLASSIFIED

UNCLASSIFIED

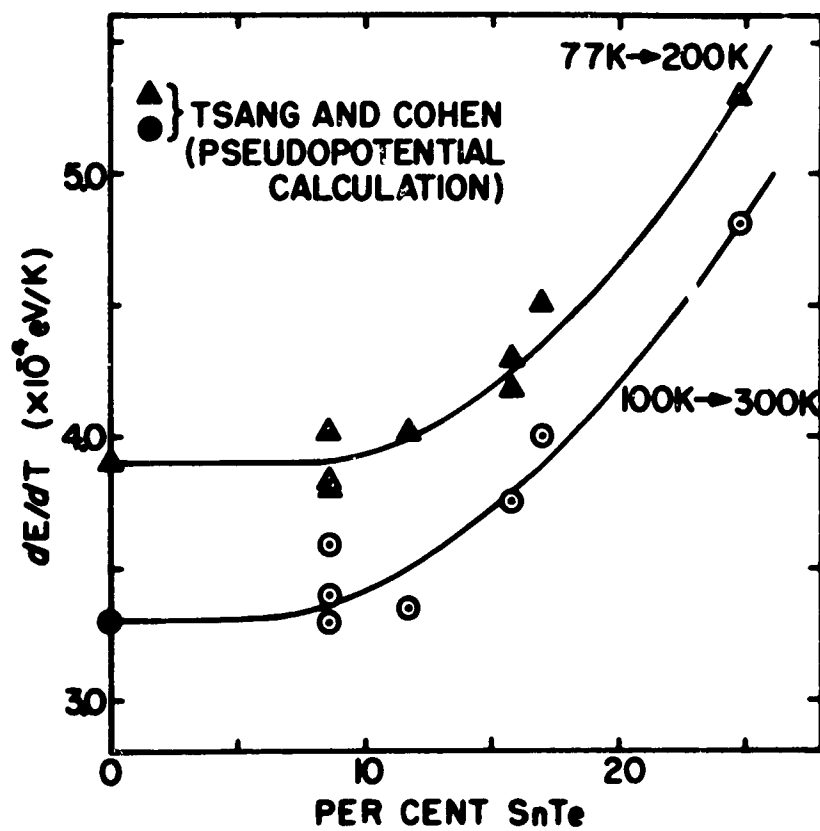


FIGURE 4

UNCLASSIFIED

UNCLASSIFIED

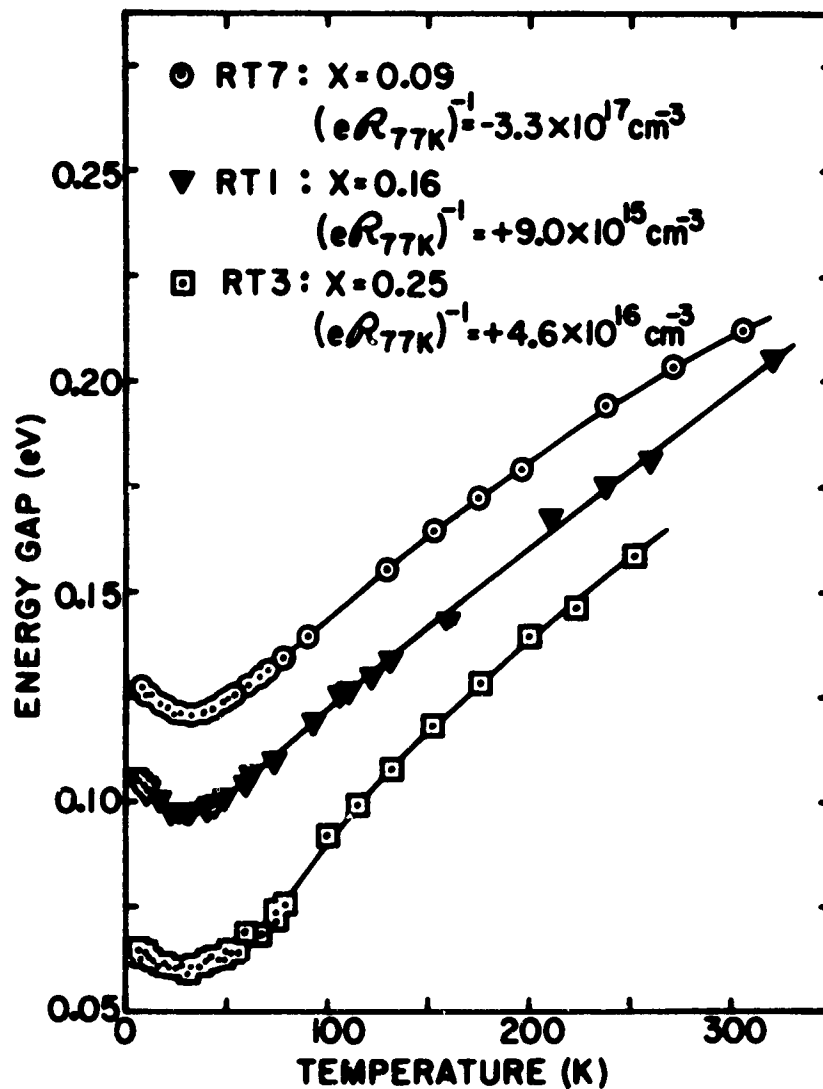


FIGURE 9

UNCLASSIFIED

UNCLASSIFIED

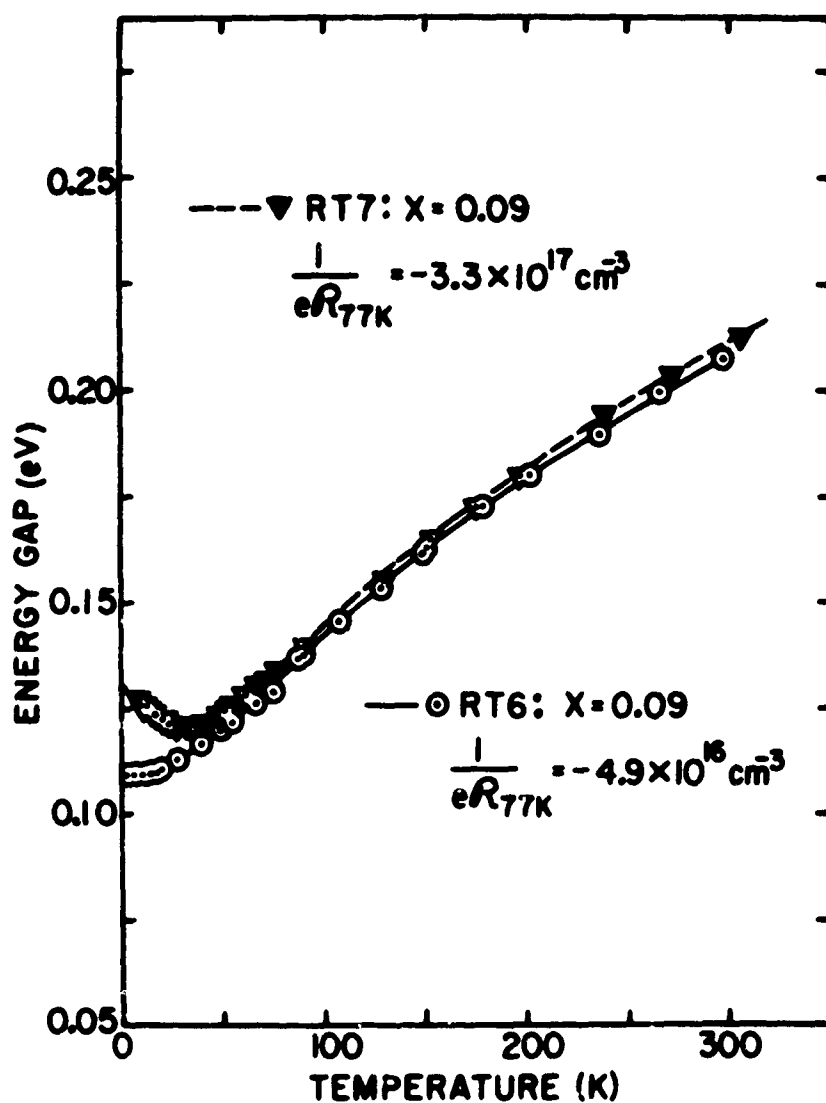


FIGURE 11

UNCLASSIFIED

UNCLASSIFIED

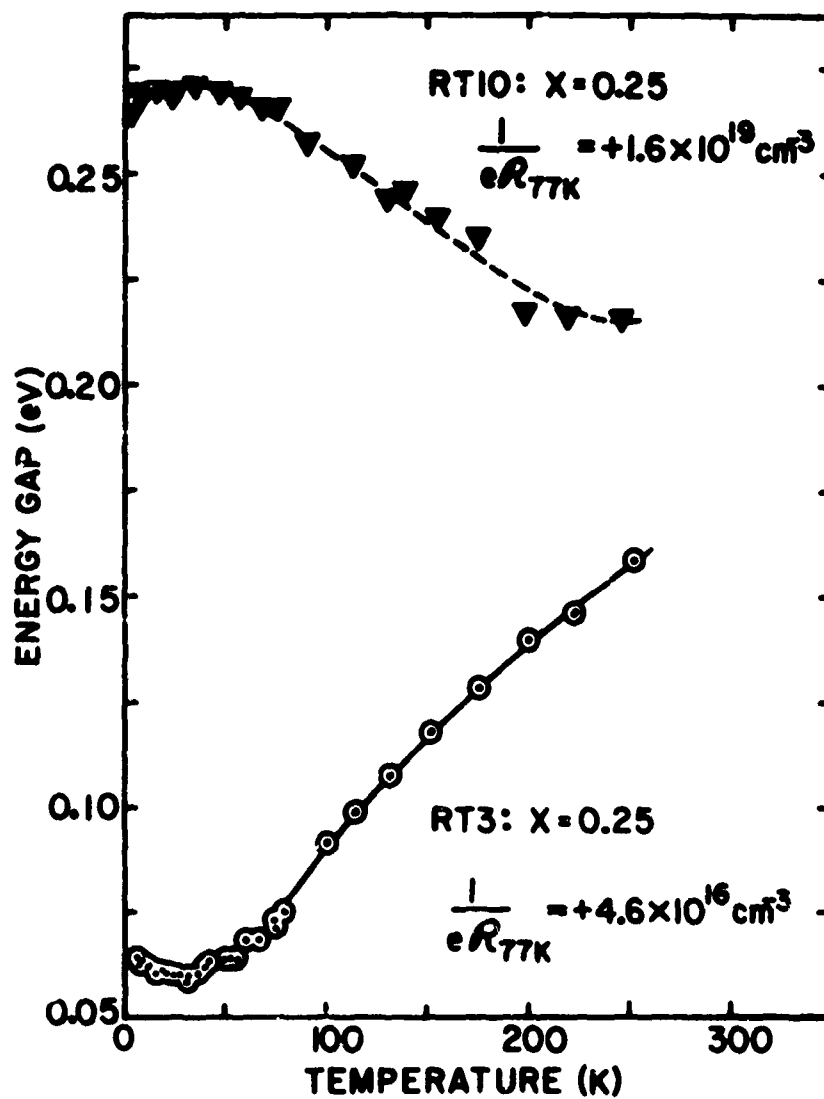


FIGURE 11

UNCLASSIFIED

UNCLASSIFIED

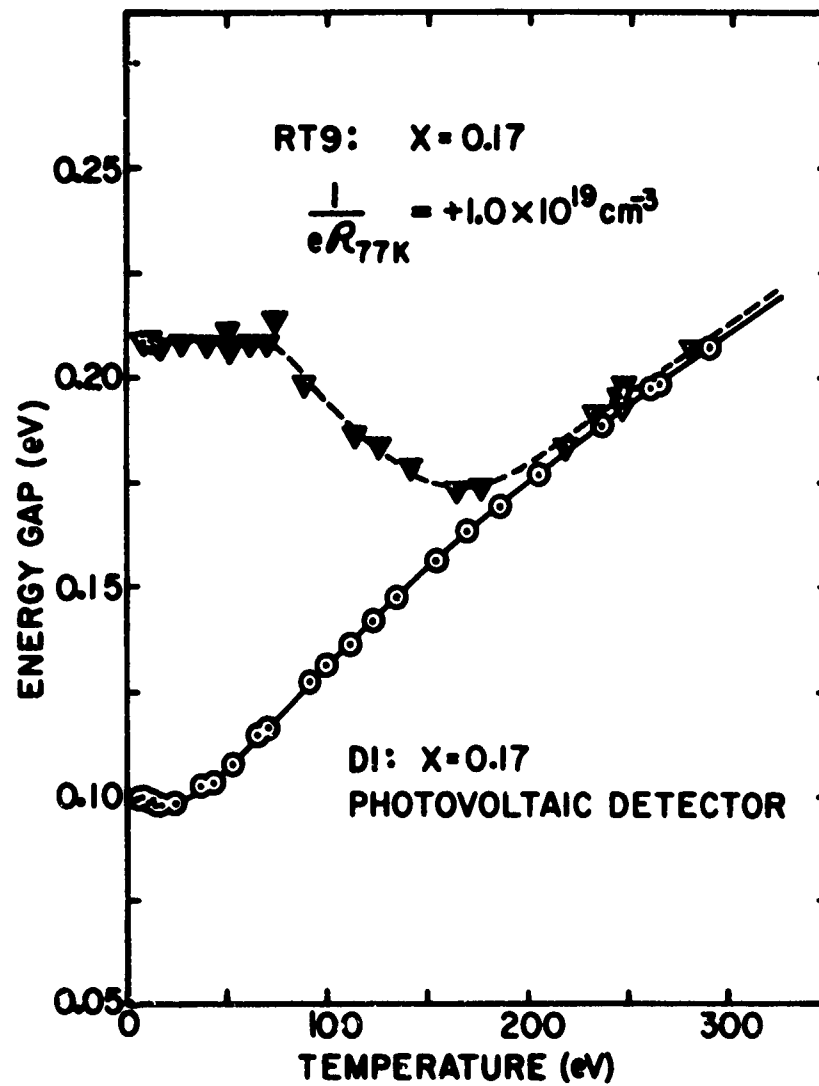


FIGURE 12

UNCLASSIFIED



# UNCLASSIFIED

.... This paper is UNCLASSIFIED

## Auger Spectrometer Surface Studies of InSb After Detector Fabrication Procedures (Unclassified)

Dr. Randolph E. Longshore  
Night Vision Laboratory  
U. S. Army Electronics Command  
Fort Belvoir, Virginia 22060

### ABSTRACT

The surface of indium antimonide was studied after various processing steps that are used in the fabrication of infrared photodiodes. An Auger Spectrometer was used for these surface studies. Data is presented of the surface contamination and stoichiometry resulting from etching, passivation, and diffusion treatments.

---

The performance of infrared detectors is very sensitive to the condition of its surface. Therefore, for optimum performance it is necessary to use fabrication procedures which will leave surfaces with the proper physical, chemical, and electrical properties. In this paper, a technique is described for characterizing the surface of InSb with an Auger Spectrometer. Data is given of the surface contaminants and surface stoichiometry after various fabrication treatments.

The mechanism of the Auger process is described by figure 1, which shows a simplified diagram of the energy levels within an atom. If the atom is bombarded with a sufficiently energetic electron beam, an electron can be removed from the K level through a collision. Then an electron from the  $L_2$  level, for example, will drop down to fill the lower K level since a more energetically favorable atomic state will be produced. In the transition from the  $L_2$  to the K level, the electron will release an energy equal to the difference in the energies of the  $L_2$  and K levels. This energy may be transferred to another electron, in level  $L_3$  for example, and allow it to leave the material. This electron is called the Auger electron and it is labeled with standard x-ray notation by the sequence of events leading to its ejection from the material, i.e. the  $K L_2 L_3$  electron in this example. Since the Auger electron energy is determined by the energies of levels within the atoms, each element, except hydrogen and helium, will have a characteristic spectrum of Auger electrons and therefore may be identified. Furthermore, the Auger electrons have energies of the order of several hundred eV and only the electrons within a few atomic layers of the surface can be ejected from the material. This property allows one to look at only the surface layer of the sample. Quantitative data can be

## UNCLASSIFIED

obtained from the Auger electron energy spectrum since the number of Auger electrons from an element will be proportional to the number of atoms of the element which are involved in the process. Calculations indicate that a surface concentration of  $10^{10}$  atoms/cm<sup>2</sup> can be detected with the cylindrical Auger electron analyzer.

A cylindrical Auger electron spectrometer made by Physical Electronics Industries was used to examine the surface of indium antimonide. Two types of data are presented from this surface study. The first type indicates the impurities found on the indium antimonide surface after various fabrication processes. The other gives the variations in the indium and antimony concentration on the indium antimonide surface after several different treatments.

As a reference sample for these surface studies, an Auger spectrum of cleaned indium antimonide was taken. The sample was cleaned by ion-sputtering in a  $5 \times 10^{-9}$  torr vacuum and the spectrum was immediately recorded. The resulting Auger spectrum is shown in figure 2, the derivative of the electron energy distribution is plotted versus the electron energy in eV. The doublet peaks near 400 eV correspond to indium and those near 450 eV are the antimony peaks. The smaller peaks are also attributed to indium and antimony.<sup>2</sup> No other elements are shown except for an argon peak. The argon was introduced as sputter gas during the ion-cleaning, and some of the argon atoms were implanted into the surface.

The starting samples for the detector fabrication were 40 mil thick indium antimonide wafers that had been polished on the "B" side by Cominco. The Auger spectrum of this surface is shown in figure 3. Since this spectrum was taken at high sensitivity, the prominent peaks between 300 and 500 eV were too large to lie within the scale of the figure. Several impurities are indicated. These include sulfur, chlorine, and carbon with small amounts of fluorine and sodium. The peaks near 100 eV are believed to be arsenic peaks. Data taken with electron energies above 1000 eV also indicated the presence of arsenic on the surface in large concentrations. From an examination of the indium surface concentration, it is believed that the polished surface is contaminated with indium arsenide.

In continuing the study of fabrication techniques, the indium antimonide surface was examined after two different passivation processes. One wafer was immersed in the H-100 solution described by Henneke.<sup>3</sup> The Auger spectrum of the H-100 sample is shown in figure 4. Three elements are prominent, potassium, indium, and oxygen. The size of the antimony peak indicates a low antimony concentration. This surface appears to consist of an indium oxide plus potassium or some compound of potassium. Potassium is part of the H-100 formula as potassium hydroxide and some form of potassium was deposited on the sample surface during the passivation treatment.

The second passivation technique is described by Minamoto and Allen<sup>4</sup> in which an indium antimonide sample is anodized in a 0.1N potassium hydroxide solution. The resulting Auger spectrum is shown in figure 5. In this case, the surface consists of indium and oxygen, with small concentrations of antimony. This surface layer appears to be composed of an indium oxide plus small amounts of antimony or antimony oxide, or some combination of these materials.

## UNCLASSIFIED

Auger spectra were taken of the indium antimonide surface after etching in different solutions and after cadmium diffusion. The etches used are: 20% Bromine in methanol,<sup>5</sup> Lactic Acid: Nitric Acid: Hydrofluoric Acid in the ratio 50:5:2,<sup>6</sup> and a modified CP4 solution referred to as CP4B.<sup>7</sup> The cadmium diffusion was carried out in a pyrex ampoule with an antimony shot to supply an antimony backpressure.<sup>7</sup> A summary of these data is shown in Table I. The impurities are listed in order of decreasing surface concentration. There were some variations in these concentrations over the indium antimonide surface and Table I indicates an average trend of the impurity concentrations.

Carbon and oxygen are found to be the most common major impurities on all surfaces examined. These elements are mainly due to absorption of oxygen and carbon dioxide. Exceptions to this are cases where oxygen occurs from the passivation treatments. Another source of carbon is from organic solvents used in cleaning which contain hydro-carbons. Sulfur and chlorine are also common impurities but these elements occur in lower concentrations than the oxygen and carbon. There are two possible sources of chlorine. Sodium chloride from handling the sample is one possibility since sodium is also observed in some cases. Also, trichloroethylene used in wafer cleaning is another source of chlorine contamination. Contamination from the stainless steel sample holder could contribute such impurities as sulfur, carbon, and chlorine. In most cases these elements were found to be real surface contaminants and not bulk contaminants since they were removed by sputtering away approximately 100 Å of surface material. Exceptions to this were of course, oxygen on the passivated surfaces and iron on the antimony doping sample which is used to supply an antimony backpressure during cadmium diffusions. Apparently, iron is a bulk impurity in the antimony sample.

Further comparisons between samples were carried out by considering the Auger peak heights which are proportional to the concentration of the corresponding element. Considerable amounts of carbon and chlorine were found on the surface of the cadmium diffused sample relative to the other samples. The sample etched in CP4B and the anodized sample had the cleanest surface. However, the oxygen and carbon concentration on the chemically etched samples were approximately the same. Unfortunately, several elements could not be detected on the indium antimonide surface due to the position of the antimony and indium peaks. The primary peaks of nitrogen, tellurium, and cadmium occur close to either antimony or indium peaks and are not measurable if they exist in low concentrations on the surface.

The second type of data, concerning the indium and antimony concentration was measured along with sputter cleaned indium and antimony as reference samples. A summary of this data is given in Table II. The fractions given in Table II are rounded off to two places. The ratios given in Table II are more accurate and are calculated directly from the peak heights from the Auger spectra. For the indium antimonide standard, the fraction of indium and antimony are slightly less than the 0.5 values expected. This difference is either due to errors in the measurements or to the presence of small amounts of impurities on the surface. The ratio of indium to antimony is equal to one as expected. The polished sample is found to be indium rich, possibly due to the presence of indium arsenide on the surface.

## UNCLASSIFIED

In comparing the chemically treated samples, the bromine-methanol and lactic-nitric-hydrofluoric etched samples are found to have approximately equal amounts of indium and antimony. However, the CP4B etched sample is found to be antimony rich. The H-100 treated and anodized samples are found to be indium rich. The ratio value for the anodized layer is in good agreement with Dewald's data<sup>4</sup> for the first 20 Å of an anodized layer. The last sample, after a cadmium diffusion is found to be slightly indium rich. This is possibly due to the out diffusion of Sb from the surface. Although an antimony back pressure was used during the diffusion, temperature variations in the diffusion cycle may have caused some out diffusion of the antimony.

In terms of detector fabrication, these findings indicate that either the bromine-methanol or the lactic-nitric-hydrofluoric etch should be used since they produce a stoichiometric surface. In comparing the two passivation techniques, the H-100 treatment leaves potassium on the surface which could possibly cause trouble in later parts of the detector processing. It is also found that the polishing process greatly contaminates the indium antimonide surface and special care should be used to keep the polishing technique clean and in cleaning the wafer after polishing. An examination of a polished surface after being etched in the 20% bromine-methanol solution for one minute appeared to remove the surface contamination and leave a stoichiometric surface.

## UNCLASSIFIED

### Literature Cited

1. Chuan C. Chang, Surface Science 25, 1971 pp 53-79.
2. R.C. Oswald and R.E. Weber, Technical Report AFAL-TR-70-12, February 1970.  
and  
J.T. Grant and T.W. Haas, Joul Vacuum Sci and Tech 8, 1971 pp94.
3. H.L. Henneke, Joul Appl Phys 36, September 1965 pp 2967.
4. M.T. Minamoto and C.M. Allen, Solid State Elec. 5, July-August 62, pp 263
5. A.N. Saxena, Appl Phys Letts 7 1 September 1965, pp 113.
6. C.J. Axt and C.G. Rogers Joul Appl Phys 41, 1970 pp 3423-3428.
7. C.H. Sutcliffe et al, Technical Doc Rpt No ASD-TDR-63-393 (AD# 403-352) Nov 1962.
8. J.F. Dewald, Joul Electro Chem Soc 104, 1957 pp 244.

UNCLASSIFIED



### BASIC AUGER PROCESS

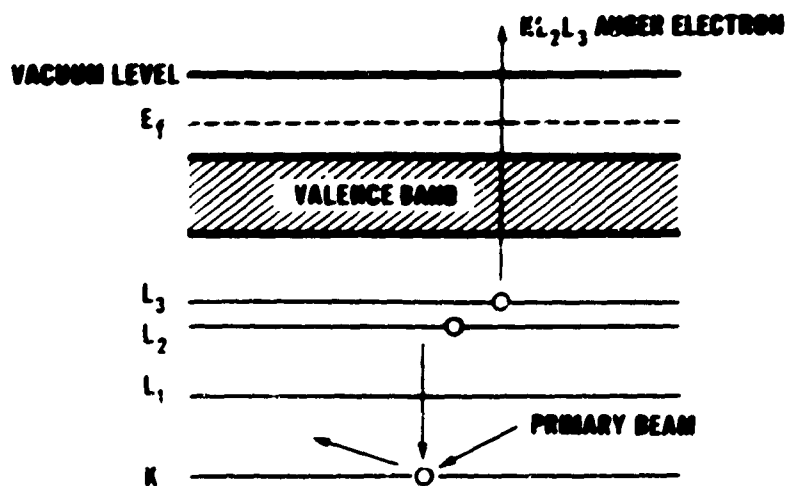


Figure 1



### InSb AUGER SPECTRUM

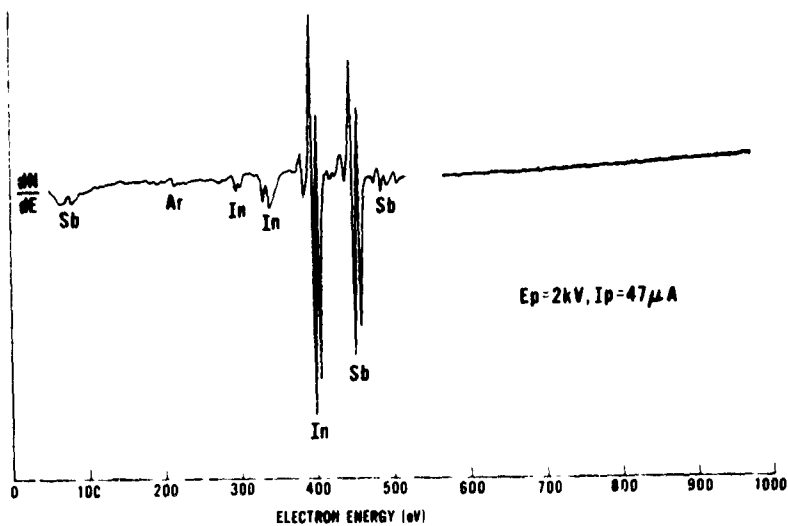


Figure 2

UNCLASSIFIED

UNCLASSIFIED

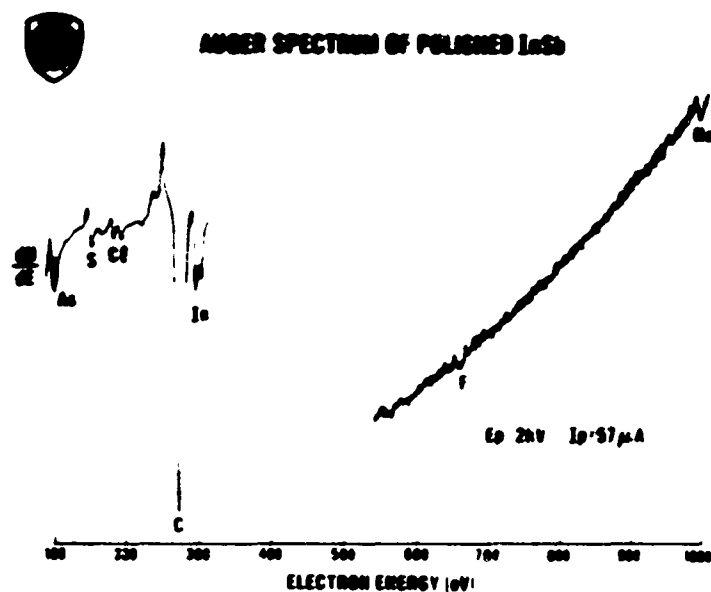


Figure 3

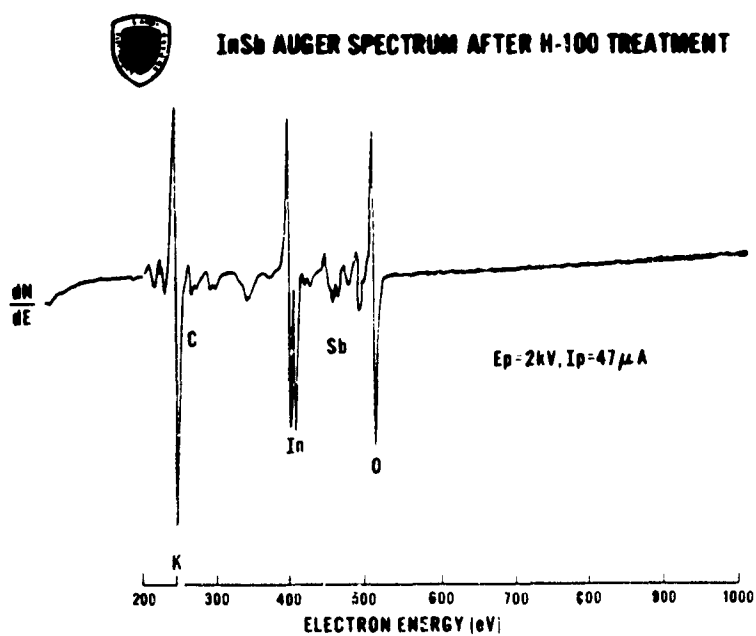


Figure 4

UNCLASSIFIED

UNCLASSIFIED

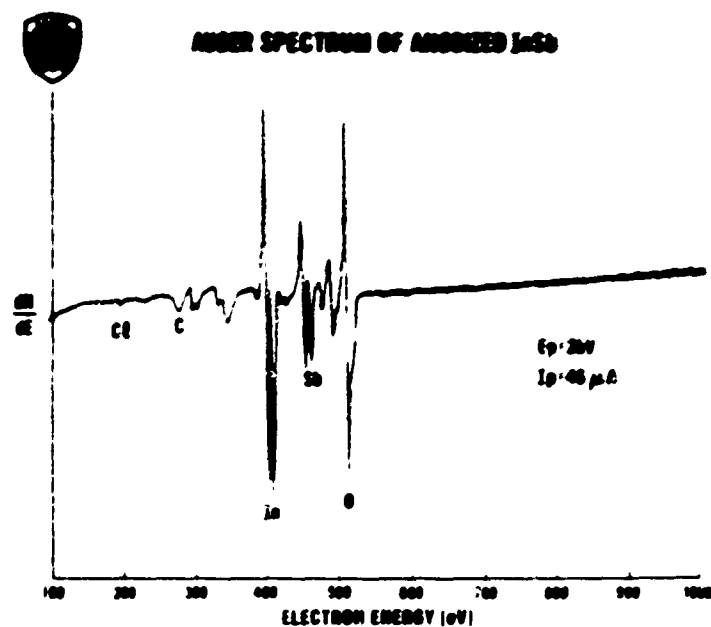


Figure 5

**ELEMENTS FOUND ON InSb SURFACE**

InSb SAMPLE	0 SIDE POLISHED	ETCHED IN 20% Br <sub>2</sub> → METHANOL	ETCHED IN 50 LACTIC ACID 5NH <sub>4</sub> OH 2HF	ETCHED IN CP4 B	H 100 TREATMENT	ANODIZED IN 0 IN KOH	AFTER C <sub>60</sub> DIFFUSION	SA DOPING SAMPLE	C <sub>60</sub> DOPING SAMPLE
MAJOR IMPURITIES	O	O	O	O	K	O	C	O	C
	C	C	S	C	O	C	Cl	C	O
	As	S	C		C		O		S Cl
MINOR IMPURITIES	S	Cl	Cl	S	Cl	Cl	S	Na	Na
	Cl			Cl	Na			Fe	Mg
	F								
	Na								

Table I



UNCLASSIFIED



**IN AND Sb CONCENTRATIONS ON InSb SURFACES**



SAMPLE	In Sb RATIO	In	Sb
InSb STANDARD	1	0.40	0.40
POLISHED InSb	2.76	0.32	0.11
InSb ETCHED IN 20% Br+MBTHAROL	0.97	0.17	0.18
InSb ETCHED IN 50 LACTIC 5 HNO <sub>3</sub> 2HF	1	0.21	0.21
InSb ETCHED IN CP40	0.87	0.17	0.20
InSb TREATED H-100	5.17	—	—
InSb ANODIZED IN KOH	2.20	—	—
InSb AFTER Cd DIFFUSION	1.36	—	—

Table II

Reverse page blank

UNCLASSIFIED

# UNCLASSIFIED

This paper is UNCLASSIFIED

## Results of a Study of the Interaction between Lithium and Several Deep Acceptor Impurities in Germanium" (Unclassified)

Paul LoVecchio\*, Kevin Riley and Henry Levinstein  
Syracuse University  
Syracuse, New York

### ABSTRACT

Impurity pairing in germanium has been investigated for its potential to produce a new family of extrinsic germanium infrared detectors. The impurity pairs studied were formed by the interaction of the donor lithium with each of the deep multivalent acceptors Zn, Hg, Au, Ni, and Mn. The location within the forbidden energy gap and the concentration of these resulting paired states were determined by resistance versus temperature, Hall and photoconductive spectral response measurements. An investigation of the interaction of lithium with the impurities Ni and Mn was made possible by the development of a technique employing an In-Li alloy as the medium from which lithium diffusion proceeded into the doped germanium.

As a result of this study, it has been found that the lithium, deep acceptor impurity interaction in germanium is sufficiently strong to produce an impurity pair stable at room temperature. Hall and resistance versus temperature measurement have led to thermal activation energies of  $11.0 \pm .4$  meV,  $32 \pm 1$  meV, and  $100 \pm 10$  meV for the impurity pairs Zn-Li, Hg-Li, and Mn-Li respectively. These energies for the Zn-Li and Hg-Li are in substantial agreement with the values reported by Morin and Reiss<sup>(1)</sup> for Zn-Li and Williams and Breazeale<sup>(2)</sup> for Hg-Li. The 100 meV Mn-Li level, however, has not previously been reported and represents a new and possibly useful member of the extrinsic germanium infrared detector family. Photoconductive thresholds of 12-39 micrometers associated with the Mn-Li and Hg-Li impurity pairs respectively are in good agreement with the thermal activation energies observed. Preliminary results of the interaction of lithium with Au and Ni impurities in germanium are also presented.

\*P. LoVecchio is presently employed at Night Vision Laboratory.

This paper presents the results of our study on impurity pairing in germanium. In particular we were interested in pairing of the donor lithium with various multivalent acceptor impurities. Our goal was to use this pairing to produce a new extrinsic germanium detector sensitive in the 8 to 14 micrometer region.

First, it would be best to briefly describe pairing and indicate how it differs from the more common compensation. Two impurity atoms are considered paired if they are situated close enough to each other within the host lattice

## UNCLASSIFIED

(germanium in this case) to alter their energy levels within the forbidden gap.  
For the impurities lithium and zinc in germanium this distance has been found<sup>(1)</sup>  
to be of the order of one lattice constant. This is to be contrasted with  
compensation where a distance of at least several lattice constants separates the  
donor and acceptor impurity atoms. This distance is sufficient to minimize the  
impurity interaction and cause no energy levels to be altered.

In the course of our experiments we looked at the interaction between lithium  
and the acceptor impurities Zn, Hg, Au, Ni and Mn. The location of these acceptor  
energy levels created within germanium's forbidden gap, when there is no inter-  
action with lithium, is well known<sup>(2,3,4)</sup> and shown in Figure 1.

If we now take a sample of germanium doped with one of these acceptor  
impurities and into it diffuse an equal concentration of lithium, where the sample  
is prevented from converting to n-type, it has been found that the position of the  
active acceptor level becomes more shallow, or shifts toward the valence band. In  
fact, more accurately, the two acceptor levels associated with the divalent  
impurity no longer exist at all upon such pairing with lithium. Figure 2 shows  
the effect which pairing with lithium was found to have on the energy levels of  
Zn<sup>(1)</sup> and Hg<sup>(5)</sup> in germanium. As can be seen there appears to be some relationship  
between the depth of the original acceptor levels and the depth of the final lithium  
paired level. This caught our eye and since we knew we were aiming for a final  
paired level in the neighborhood of 0.1 eV, we choose the very deep acceptors Mn,  
Ni and Au to pair with lithium.

Diffusing lithium into Ge:Au we were able to prove that Au and Li do indeed  
pair in germanium, with the Li not merely compensating the Au. This was proven  
by measuring the electron Hall mobility in Ge:Au which had been converted to p-type  
after Li diffusion. The large magnitude of the mobility at low temperatures  
( $10^5 \text{ cm}^2 \text{ volt}^{-1} \text{ sec}^{-1}$  at 8 Kelvin) indicated very little ionized impurity scattering  
was occurring, which would not have been the case if the Li were compensating the  
Au acceptors ( $10^{15}$  Au atoms/cc).

However, even at the lowest temperatures of lithium diffusion ( $165^\circ\text{C}$ ) the  
samples consistently converted to n-type, which prevented us from measuring the

## UNCLASSIFIED

location of the Au-Li paired acceptor level. We then moved on to the impurities Ni and Mn.

With the choice of these impurities, however, a problem arose. To diffuse lithium into the bulk of a Mn or Ni doped germanium sample the conventional procedure is to alloy a thin coating of pure lithium to the surface of the germanium sample at about 400°C and then diffuse lithium from this alloy region into the bulk of the germanium. The problem arises when you subject a piece of Mn or Ni doped germanium to temperatures of 400°C for as little as 30 seconds. This is enough to make the Mn or Ni levels no longer active and cause them to be replaced by a relatively shallow .05 ev level. This phenomenon had been studied previously by Penning (6) and Tyler (7) and was referred to as impurity precipitation.

To get around this problem we developed the technique shown in Figure 3 for lithium diffusion which allows the doped germanium sample never to be heated to temperatures higher than that at which lithium diffusion is taking place, or about 200°C. The heart of this technique is the In-Li alloy, containing 0.4 weight % Li in In. At the diffusion temperatures used the Indium has a very low diffusion coefficient in germanium allowing only insignificant Indium diffusion into the sample. However, the Li diffuses in quite readily at these temperatures. The particular alloy composition we choose had a melting point of 155°C and therefore could be used for low temperature lithium diffusion.

To test the effectiveness of this method we used it on samples of Zn and Hg doped germanium since some of the results of lithium pairing with these impurities were already known as has been mentioned. Our results, using the In-Li alloy were in good agreement with those previously reported and gave us confidence in our method.

Figure 4 shows the results of photoconductive spectral response measurements made on two samples of lithium diffused Ge:Hg. Also included is one of their controls. You can see the shift in the threshold from 12 to 39 micrometers in very good agreement with results of our Hall measurements. Looking a little more closely at the threshold of the Hg:Li pair we noticed the electric field dependence shown in Figure 5. Further study will be needed to determine the cause of this

## UNCLASSIFIED

behavior.

At this time I'd like to point out that we never noticed any significant dissociation of these pairs when stored at room temperature. They appear quite stable.

We then used this In-Li alloy method on Ge:Ni but with disappointing results. We could see no significant change in the activation energy after using the alloy, but the acceptor density did decrease by a factor of two or more after each diffusion indicating lithium was getting in. Control samples immersed in pure indium showed no such decrease. Either the lithium was compensating the Ni or pairing to produce a level identical with that of the lowest Ni level. In either case, it was obvious that we weren't going to get a .1eV level from Li diffusion into Ge:Ni; so we looked at the results of Li diffusion into Ge:Mn using, once again, our In-Li alloy.

Here, to our great satisfaction, we got the results we were after. The Ge:Mn used for this experiment contained approximately  $10^{15}$  Mn atoms/cc and had a thermal activation energy of .16 eV before Li diffusion. Immersion in the In-Li alloy for 3 days at 200°C consistently reduced this activation energy to  $.10 \pm .01$  eV. This shift in the thermal activation energy was accompanied by the change in the photoconductive spectral response of one of the samples shown in Figure 6. You can note the enhanced sensitivity due to the Mn-Li acceptor pairs in the 8 to 12 micrometer region. The peak response at 5 micrometers indicates the presence of some free Mn still unpaired with Li. To reduce the amount of unpaired Mn we Li diffused at a higher temperature to introduce more Li into the sample. Figure 7 shows the results of this diffusion. At 6 Kelvins the response by the Mn-Li pairs appears to be more significant, but unpaired Mn is still playing a large role. The response at 77 Kelvin shows that indeed free unpaired Mn is present since charge carriers from the .10eV Mn-Li state have already been thermally excited and wouldn't be optically active at this temperature.

From these results with the Mn-Li pair we feel we have found a new extrinsic level in germanium capable of giving a peak response in the 10 to 12 micrometer region. A further study of this level will now be needed to determine the full

## UNCLASSIFIED

extent of its potential use for infrared detectors.

In summary, Figure 8 gives the results found so far for Li pairing in germanium.

UNCLASSIFIED

### ENERGY LEVEL DIAGRAM FOR IMPURITY ATOMS IN GERMANIUM

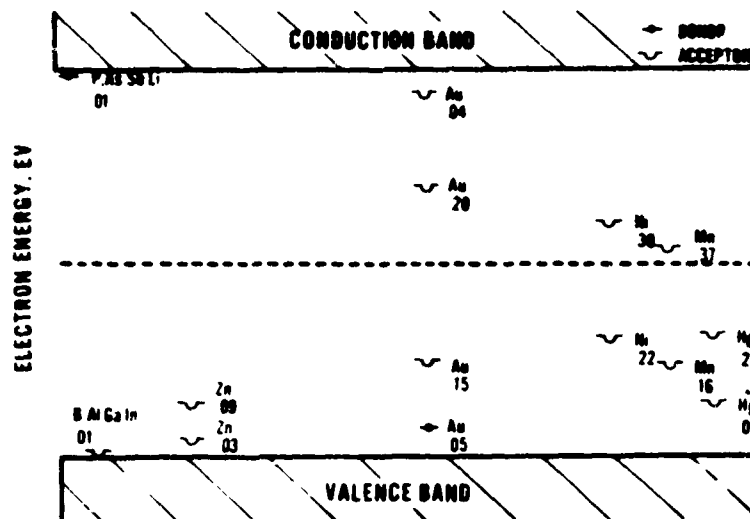


Figure 1 - Position of impurity levels with no lithium interaction.

### EFFECT OF LITHIUM PAIRING

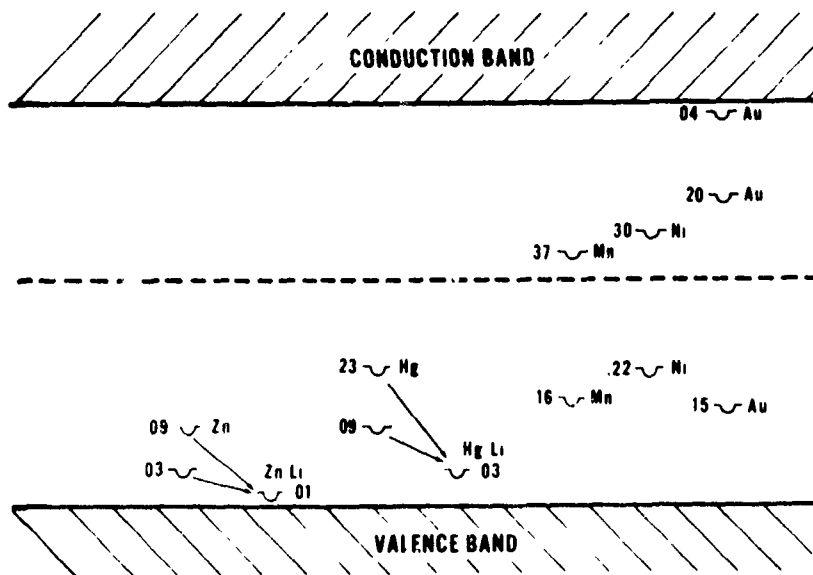


Figure 2 - Effect on Zn and Hg impurity levels when paired with lithium.

UNCLASSIFIED

UNCLASSIFIED

### LITHIUM DIFFUSION TECHNIQUE

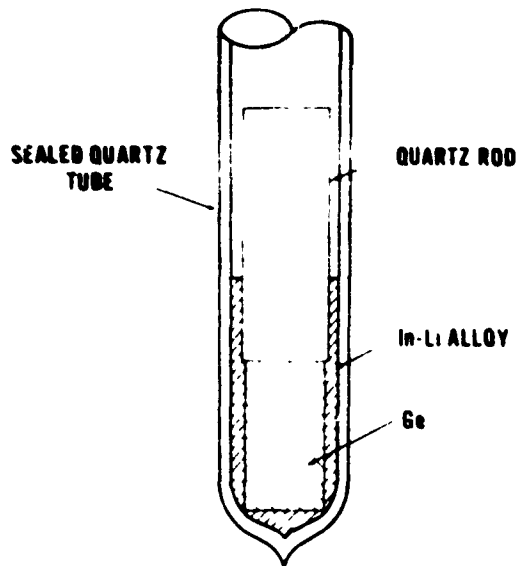


Figure 3 - In-Li alloy technique used for lithium diffusion into doped germanium.

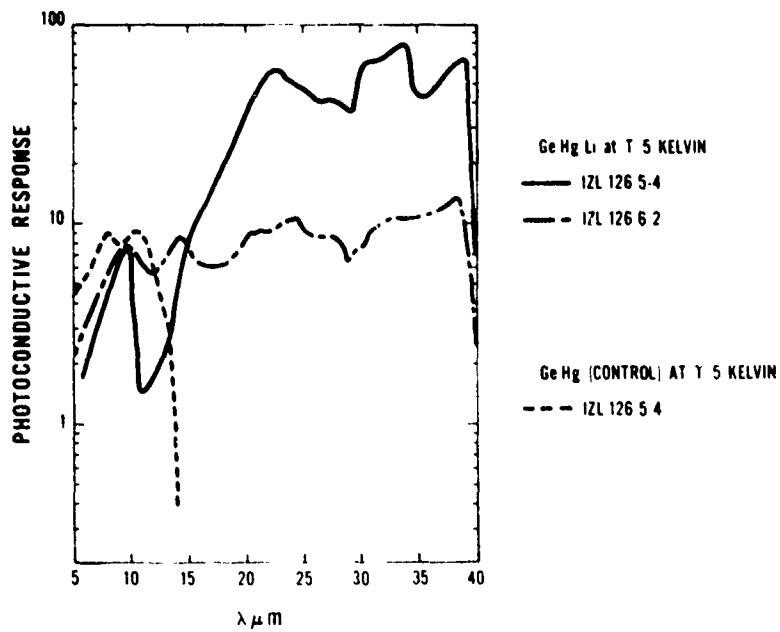


Figure 4 - Effect of lithium diffusion on spectral response of Ge:Hq.

UNCLASSIFIED



UNCLASSIFIED

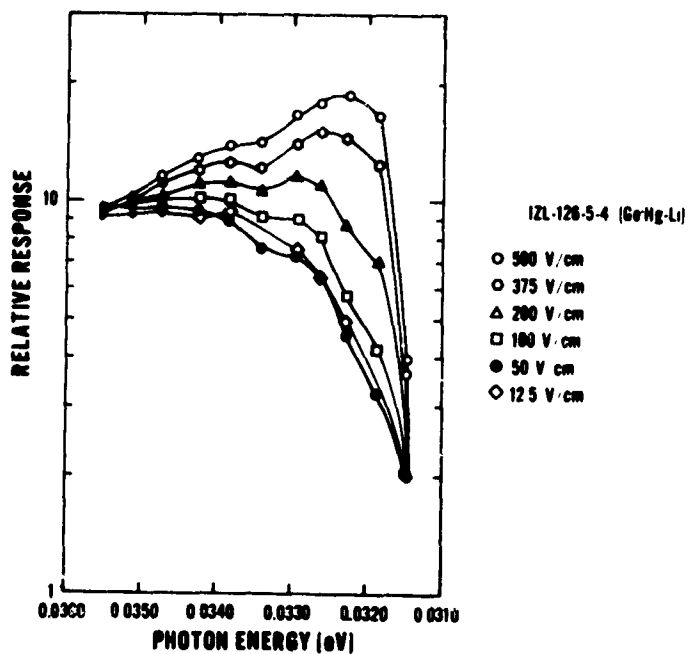


Figure 5 - Electric field dependence of photoconductive threshold observed in Ge:Hg-Li.

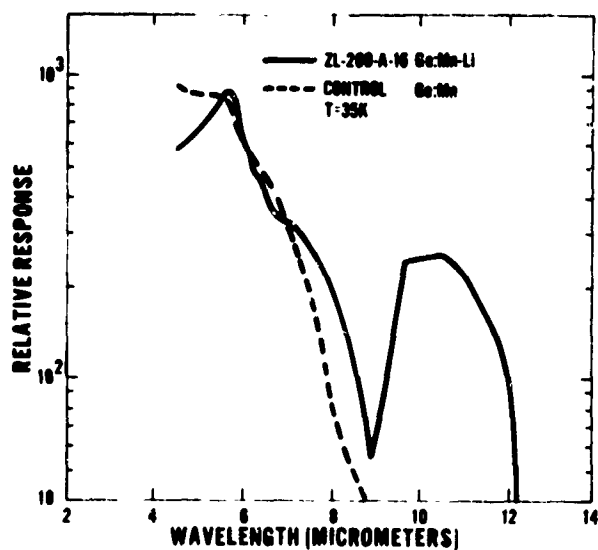


Figure 6 - Enhanced sensitivity in 8 to 14 micrometer region produced by lithium diffusion into Ge:Mn.

UNCLASSIFIED

UNCLASSIFIED

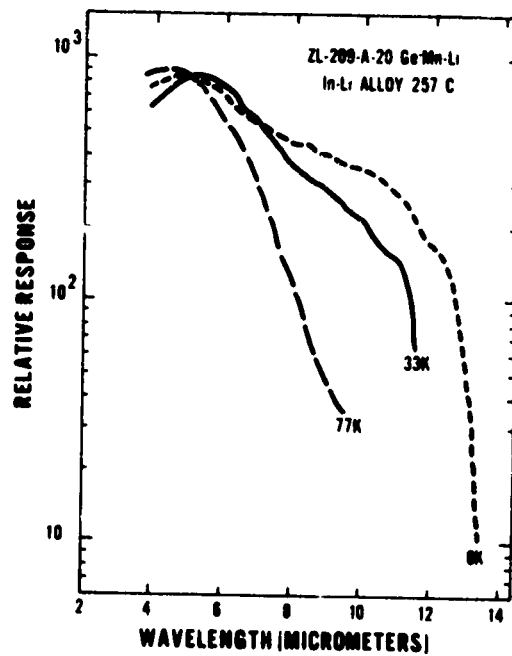


Figure 7 - Results of higher lithium diffusion temperature than that shown in Figure 6.

### SUMMARY OF PAIRING RESULTS

ACCEPTOR IMPURITY (A)	LOWEST UNPAIRED(A <sup>-</sup> ) eV	PAIRED E=L <sub>1</sub> <sup>+</sup> eV
Zn	.032	.010 ± .0005
Hg	.092	.032 ± .001
Ni	.22	? .22
Au	.14	YES
Mn	.16	.10 ± .01

Figure 8

# UNCLASSIFIED

## REFERENCES

1. F.J. Morin and H. Reiss, Phys. Rev. 105, No. 2, p. 384 (1957).
2. W.W. Tyler, Proc. of Third Int. Conf. on Semiconductors, (1958).
3. E.M. Conwell, Proc. of the IRE 46, p. 1281 (1958).
4. S.R. Borrello and H. Levinstein, J. Appl. Physics, 33, p. 2947 (1962).
5. R.L. Williams and B.H. Breazeale, Phys. Rev. Lett. 18, no. 25, p. 1129 (1967).
6. P. Penning, Philips Res. Repts., 13, pp. 17-36 (1958).
7. W.W. Tyler, Advances in Semiconductor Science, Proc. of Third Int. Conf. on Semiconductors, p. 61, Pergamon Press, (1958).

# UNCLASSIFIED

.... This paper is UNCLASSIFIED

## RECOMBINATION CROSS-SECTION FOR HOLES IN Ge:Hg AND ELECTRONS IN N-TYPE Si (Unclassified)

P. Norton, T. Braggins and H. Levinstein  
Department of Physics  
Syracuse University  
Syracuse, New York

### ABSTRACT (Unclassified)

The recombination cross section for mercury-doped germanium has been measured between 4-40 K, in the limit of low electric fields. It was found to be identical to the cross-section of copper-doped germanium. Trapping by residual copper impurities in the mercury-doped samples was accounted for by quantitatively determining the density of these centers from carrier concentration and mobility analysis. The recombination cross-section of phosphorous-doped Si was measured in the low field limit, between 3-20 K. The temperature dependence agrees well with the quantum mechanical theory for recombination in silicon, but the measured cross-section is more than an order of magnitude larger than the calculated value.

### 1. MERCURY-DOPED GERMANIUM

Measurement of the recombination cross-section for holes in mercury-doped germanium is complicated by the presence of residual copper impurities which act as trapping centers.<sup>(1-3)</sup> Because the diffusion coefficient of copper is large in germanium at temperatures near the melting point, copper can easily enter the crystal when doping with mercury. Although the total concentration of copper may be more than three orders of magnitude less than the concentration of mercury, copper may still strongly influence the carrier lifetime. Determination of the recombination properties of copper and shallow impurities, studied in earlier work,<sup>(2,4)</sup> makes it possible to understand quantitatively the lifetime behavior shown by mercury-doped germanium. Figure 1. shows the energy levels of shallow acceptors, copper and mercury. Since the energy level of mercury, like copper, is deeper than the optical phonon energy, the recombination properties of singly ionized copper and mercury impurities are expected to be similar.

Figure 2. shows the results of compensating the mercury level in copper-contaminated, mercury-doped germanium. Donor impurities must be added to fill completely the lowest copper level near .04 eV, and fill partially the mercury level at .09 eV. At low temperatures and weak illumination, holes excited into the valence band can recombine on the compensated mercury centers, or become trapped on compensated copper centers. (At low enough temperatures, shallow acceptors may also act as trapping centers, but we shall ignore this additional complication.) Unless very fast response times are required, typical compensation of detector material will produce between  $10^{12}$

# UNCLASSIFIED

and  $10^{13}$  compensated mercury atoms per cubic centimeter. Since the number of contaminating copper centers is about equal to this level of compensation, at least in material we have measured, the number of copper traps is comparable in magnitude to the number of mercury recombination centers.

In order to understand the behavior of a given sample, we must be able to determine the number of compensated mercury atoms, and the number of contaminating copper centers. This is possible by analyzing both the temperature dependence of the carrier concentration and the mobility, as measured from the Hall effect. Analysis of the first of these gives the density of compensated mercury centers. In the case of ionized impurity scattering, which contributes to the total scattering lifetime from which we determine the carrier mobility, both ionized mercury and copper centers will contribute. Thus a complete analysis of the carrier mobility allows us to determine the combined density of compensated copper and mercury centers. This has been carried out for two mercury-doped samples, one of which was grown in our laboratory, sample A, and one of which was supplied by a manufacturer of these detectors, sample B. Details of the analysis technique have been reported in earlier work.<sup>(4)</sup> Figure 3. shows the results of this analysis. We see that sample A has about  $6 \times 10^{12}/\text{cm}^3$  of copper, while sample B has  $1.4 \times 10^{13}$  copper impurities per cubic centimeter. In both cases the density of compensated copper is clearly non-negligible compared with the density of compensated mercury centers.

RESULTS OF CARRIER CONCENTRATION AND MOBILITY ANALYSIS		
SAMPLE	A	B
$n(T)$	$7.0 \times 10^{12}$	$2.4 \times 10^{12}$
$\mu(T)$	$1.3 \times 10^{13}$	$1.6 \times 10^{13}$

Figure 3. COMPENSATION ANALYSIS. Carrier concentration analysis gives density of compensated mercury centers. Mobility analysis gives density of compensated mercury and copper impurities. Subtraction gives concentration of copper traps. Values are given in density per cubic centimeter.

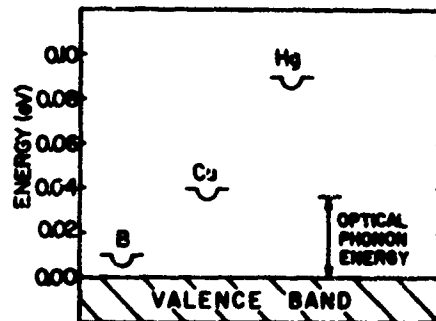


Figure 1. IMPURITY LEVELS IN GERMANIUM.

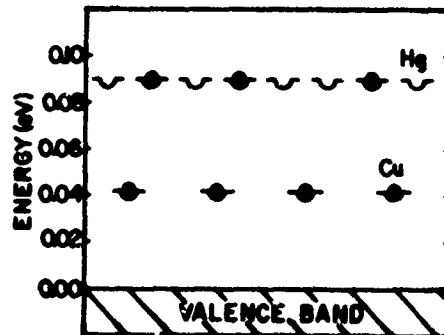


Figure 2. COMPENSATED MERCURY-DOPED Ge. Compensating donor electrons completely fill residual copper acceptors.

To see the actual effects of these relatively large number of trapping centers on the response time, photoconductive decay measurements are shown in Figures 4-7. for temperatures between 4.9 and 57 K. At the lowest temperature, thermal ionization of the copper traps is impossible, and holes trapped on these centers must be photoionized to reenter the valence band. Hence, a secondary response time, with a time constant characteristic of the thermal trap-release time cannot be observed. At temperatures above 20 K, thermal release of copper traps, and subsequent capture by mercury recombination centers (or another trap) gives a two time constant decay. Detailed equations describing the kinetics of this have been given elsewhere.<sup>(2,5)</sup>

# UNCLASSIFIED

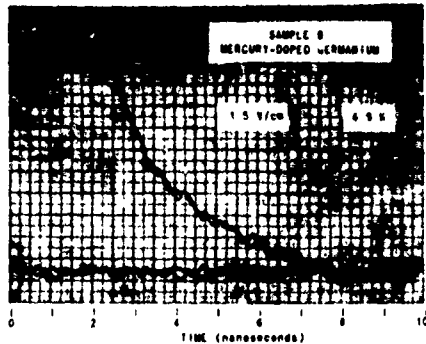


Figure 4. PHOTOCONDUCTIVE SIGNAL DECAY.

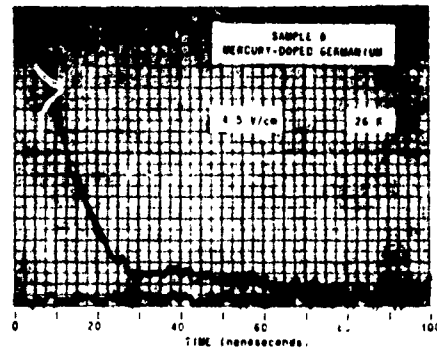


Figure 5. PHOTOCONDUCTIVE SIGNAL DECAY.

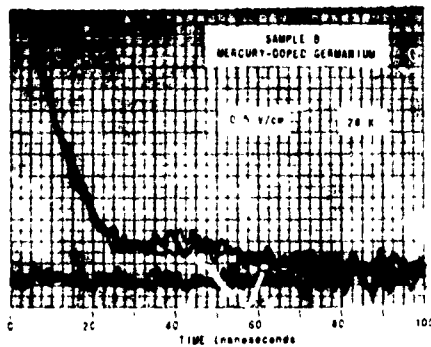


Figure 6. PHOTOCONDUCTIVE SIGNAL DECAY.

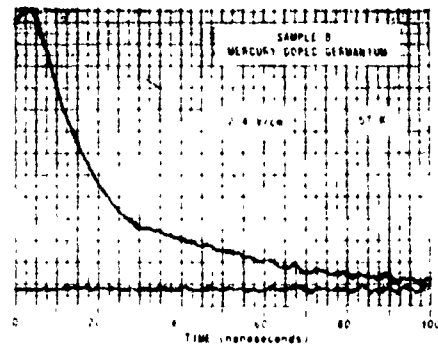


Figure 7. PHOTOCONDUCTIVE SIGNAL DECAY.

Photo-Hall measurements were made on samples A and B to determine the temperature dependence of the average carrier lifetime over the temperature region below 40 K. To understand these steady-state measurements, we distinguish two separate temperature regions. First, below 20 K the generation of carriers is entirely optical, and takes place from neutral mercury and copper centers. Since the number of neutral copper centers is much smaller than the number of neutral mercury centers, we can ignore optical generation from neutral copper. However, both mercury and copper centers which are singly ionized will provide recombination centers (the distinction between copper being a trap or recombination center is ignored since only the spectral sensitivity will distinguish how holes can be removed from these impurities below 20 K.) The second region, above 30 K, has a generation term due to optical generation of neutral mercury and thermal generation of neutral copper. Again the neutral copper density will be negligible and will be ignored. Recombination in this region will only occur through singly ionized mercury centers, since holes captured on copper centers will be rapidly reionized due to thermal excitation. The generation and recombination terms for these two cases are summarized in Figure 8., and the results are displayed for the case of a photo-Hall measurement in Figure 9., where  $p=Gi$  is assumed to be valid. The region between 20 and 30 K will be a transition between these two cases. Figures 10. and 11. show the results of the photo-Hall measurement for samples A and B. The inflection in the photo-Hall slope between 20 and 30 K can be seen in both cases. The thermal activation temperature dependence is shown for copper (dashed line) and mercury (solid line), along with the results of direct photoconductive decay measurements.

# UNCLASSIFIED

TEMP.	<20 K	30-40 K	$p = 6\gamma$	
GEN.	$G_{op}(N_{Hg}^0 + N_{Cu}^0)$	$G_{op}N_{Hg}^0 + G_{th}N_{Cu}^0$	$p = \frac{G_{th}N_{Hg}^0}{v\sigma(N_{Hg} + N_{Cu})}$	T <20 K
RECOMB.	$[v\sigma(N_{Hg} + N_{Cu})]^{-1}$	$(v\sigma N_{Hg})^{-1}$	$p = \frac{G_{th}N_{Hg}^0}{v\sigma N_{Hg}}$	T 30-40 K

Figure 8. GENERATION AND RECOMBINATION EQUATIONS. Carrier generation and recombination terms are shown for mercury-doped germanium for two temperature regions.

Figure 9. RESULTING CARRIER CONCENTRATION BASED ON EQUATIONS IN FIG. 8. AND THE APPROXIMATIONS GIVEN IN TEXT.

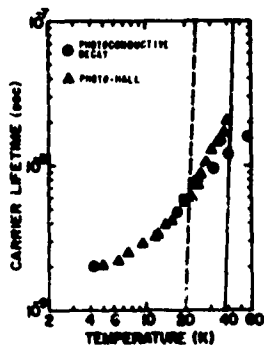


Figure 10. MEASUREMENTS ON SAMPLE A. Photo-Hall data has been normalized to photoconductive decay data below 20 K.

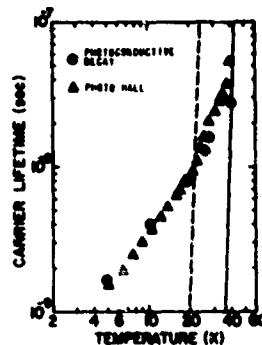


Figure 11. MEASUREMENTS ON SAMPLE B. Photo-Hall data has been normalized to photoconductive decay data below 20 K.

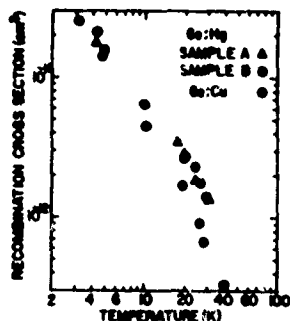


Figure 12. RECOMBINATION CROSS-SECTIONS. Results of two mercury-doped, copper contaminated samples, A and B, compared with germanium doped only with copper. The agreement below 20 K indicates that the recombination cross-section for mercury is identical to that of copper.

How do we separate the cross sections of the copper traps from those of the mercury recombination centers under these conditions? To do this we will use a rather obvious guess and check it against our data. As we have pointed out, both copper and mercury have ground state energies deep enough to permit recombination to occur via optical as well as acoustic phonon emission. On this basis we will guess that the recombination cross sections of both mercury and copper are identical. This is reasonable since the excited state energy levels, through which acoustic phonon assisted capture takes place, are identical for both impurities, and the optical phonon cross sections are also very likely identical. Below 20 K, recombination is effectively occurring at both

# UNCLASSIFIED

singly ionized copper and mercury. Therefore, we take the total ionized density of copper and mercury as the density of recombination centers, and compute the cross-sections from the measured decay below 20 K, using:  $\sigma = [\langle v \rangle \tau (N_{Cu}^- + N_{Hg}^-)]^{-1}$ . These are displayed for both samples in Figure 12, and compared to the cross-section of germanium doped only with copper. As can be seen, there is good agreement for both samples below 20 K. Since the results lie very close to the cross-section of copper alone, we conclude that the cross-section of mercury must be very nearly identical to that of copper.

## 2. N-TYPE SILICON

Results of our measurements of the cross-section of n-type silicon are preliminary at this time, since only one phosphorous-doped sample has been measured. However, it is unlikely that we are more than a factor of two from a correct estimate on the basis of this one measurement and the current interest in extrinsic silicon detectors prompted this early report. Hall measurements were first made to determine the carrier concentration and mobility between 18 and 150 K, using magnetic fields between 10 and 20 kilogauss. The lowest product of mobility times field strength was  $8 \times 10^7$  cm<sup>2</sup>gauss/Volt sec., which is close to the high field limit. This is uncertain justification for setting the Hall factor equal to unity, and this is the principal source of possible error in the following results. (The Hall factor for low fields may vary as much as 30% from unity, but this error should be much smaller at the fields we have used.) A computer program was used to analyze the temperature dependence of the carrier concentration, giving the best least squares fit to the expression:

$$\frac{n(n+N_a)}{N_d - N_a - n} = \frac{N_c \exp(-E_d/kT)}{2+6e^{-D/kT} + 4e^{-(d+D)/kT} + e^{-E_d/kT} (24e^{+A/kT} + 35e^{+B/kT} + 24e^{+C/kT})}$$

where  $n$  is the carrier concentration,  $N_d$ ,  $N_a$  and  $N_c$  are the densities of donors, acceptors and states in the conduction band, and  $E_d$  is the lowest ground state energy.  $N_c$  is  $5.29 \times 10^{15} T^{3/2} \text{ cm}^{-3}$ , including electron spin and valley degeneracy. The lowest ground state is two-fold degenerate, and is split off from the six-fold degenerate state and the four-fold degenerate state by  $D$  and  $d+D$  electron volts respectively. (6) Also included in the above expression are three groupings of excited states, lying  $A$ ,  $B$  and  $C$  electron volts below the conduction band edge. (7) We have used an average energy for each group and multiplied this by the total degeneracy of the group. Table I. lists these values. With this expression we have fit the measured values of  $n$  to determine  $N_d$ ,  $N_a$  and  $E_d$ . Two fits were made, one which included a single data point taken at 300 K, and another using only the low temperature data. Table II. shows the results of these fits. To compute the cross-section we used an average value of  $5 \times 10^{12}/\text{cc}$  for the acceptor concentration, which is equal to the concentration of recombination centers for low temperatures and weak illumination.

TABLE I. ENERGY SPACINGS FOR PHOSPHOROUS-DOPED SILICON. (Ref. 6 and 7)

symbol	energy(meV)
D	11.85
d+D	13.20
A	10.2
B	5.8
C	2.9

Photo-Hall measurements were made to determine the temperature dependence of the carrier lifetime, and these were normalized to direct measurements of the photoconductive signal decay, measured at 10.6 and 19.6 K. Figure 13. shows the results of these measurements. As can be seen, the lifetime seems to follow a simple power law up to about 20 K where thermal generation begins to dominate. When converted into a cross-section,



# UNCLASSIFIED

TABLE II. PARAMETERS DETERMINED FROM COMPUTER FITTING THE CARRIER CONCENTRATION AS A FUNCTION OF TEMPERATURE IN A PHOSPHOROUS-DOPED SILICON SAMPLE.

$N_d (\text{cm}^{-3})$	$N_a (\text{cm}^{-3})$	$E_d (\text{eV})$	comment
$1.1 \times 10^{16}$	$4.4 \times 10^{12}$	.0462	All data taken below 150 K.
$9.9 \times 10^{15}$	$6.1 \times 10^{12}$	.0453	Same, plus single data point at 300 K.

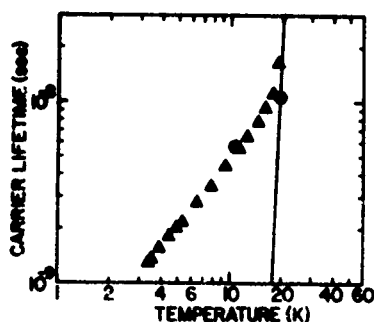


Figure 13. PHOTO-HALL AND PHOTOCONDUCTIVE DECAY MEASUREMENTS ON Si:P. Photo-Hall data, triangular points, have been normalized to photoconductive decay measurements, circles.

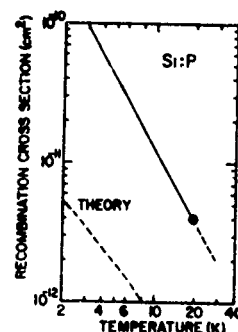


Figure 14. RECOMBINATION CROSS-SECTION FOR ELECTRONS IN PHOSPHOROUS-DOPED SILICON. Data represented by solid upper line, theory of Brown and Rodriguez (ref. 11) shown below.

as shown in Figure 14., we find the cross-section to be given by:  $4 \times 10^{-12} (\frac{T}{20 \text{ K}})^{-1.7} \text{ cm}^2$ . A value of  $0.3 m_0$  was used for the effective mass in calculating the average thermal electron velocity. These results can be compared with copper and mercury-doped germanium, which have cross-sections of about  $2.5 \times 10^{-12} \text{ cm}^2$  at 20 K.

Several remarks are in order on this experiment. Our measured response times were taken in the limit of low electric fields, so that carrier heating did not result from the applied field, and comparison with theory could be made. At 10 K, the response time began to increase with bias above about 5 volts per centimeter. At lower temperatures we could not reach the low field limit, but the time constant showed an electric field dependence between  $E^{1/2}$  and  $E^1$ . It might be expected to increase more rapidly with field strength at higher fields, as found by Koenig, Brown and Schillinger<sup>(8)</sup> for n-type shallow-impurity germanium.

Other measurements of the cross-section for n-type silicon have been made by Levitt and Honig<sup>(9)</sup>, Loewenstein and Honig<sup>(10)</sup>, and Leadon and Naber<sup>(11)</sup>. The results of Levitt and Honig on phosphorous-doped silicon gave a cross-section of  $2 \times 10^{-12} (\frac{T}{20 \text{ K}})^{-1/2}$ . This implies a carrier lifetime which is independent of temperature, and is in disagreement with the theoretical temperature dependence given by Brown and Rodriguez<sup>(12)</sup> for silicon. It is our belief that the measurements of Levitt and Honig were made on non-thermal carriers, and therefore the true temperature dependence of thermal carriers was not determined. Carrier thermalization should occur in silicon in about  $5 \times 10^{-10}$  seconds at 4 K, assuming energy loss via acoustic phonon emission. If our cross-sections are correct, and if the acceptor concentrations measured by Levitt and Honig are

## UNCLASSIFIED

used, then all of their samples have carrier lifetimes at 4 K which are shorter than the time required for carriers to thermalize. In p-type germanium it has been shown that this situation leads to carrier lifetimes which are independent of temperature.<sup>(4)</sup> Various other attempts have been made to explain the unexpected temperature dependence found by Levitt and Honig, including variations in the Hall factor,<sup>(13)</sup> impurity-hopping conductivity,<sup>(14)</sup> and capture by neutral impurities.<sup>(15)</sup> We feel that the basic recombination theory is correct in concept, since it has already been shown to give reasonable agreement with the temperature dependence of shallow, n-type impurities in germanium.<sup>(8,12)</sup> We have shown this theory, taken from Brown and Rodriguez, in Figure 14, for comparison with our results. There is considerable disagreement between theory and experiment in the order of magnitude,<sup>(16)</sup> but at the highest temperatures for which the calculation was carried out (10 K) we find good agreement between our results and the predicted temperature dependence of  $T^{-1.6}$  for the cross-section. The exclusion of excited states above the seventh order is the most likely cause of the weaker temperature dependence of the theoretical curve below 10 K.

### 3. CONCLUSIONS

The recombination cross-section of mercury-doped germanium is identical to that of copper-doped germanium, and is given by the expression:  $2.5 \times 10^{-12} \left(\frac{T}{20 \text{ K}}\right)^{-n} \text{ cm}^2$ , where  $n$  will vary with compensation, as in the case of copper-doped germanium, between about 1.0 and 1.6. As far as further work is concerned, it appears there should be an intense crystal growing effort to first eliminate the copper contamination, and second, to make reproducible the introduction of compensation levels below  $10^{12}/\text{cc}$ . This has been shown to be feasible by the work already accomplished in producing ultra-pure germanium crystals for gamma ray detection which has been in progress for several years.

Recombination cross-sections for n-type shallow donors in silicon show larger values than had been reported in earlier experiments or theory. As with germanium, responsivity can be greatly enhanced by reducing the level of compensation in these materials.

### References

1. Theoretical Studies of the Long Time-Constant Effect in Mercury-Doped Germanium, by Cecil C. Rousseau, Texas Instruments, Inc., August 29, 1963.
2. J. Stannard, Doctoral Dissertation, Syracuse University (1968).
3. T. Kaneda, H. Sei, T. Yamaoka and Y. Ueda, Japan. J. Appl. Phys. 10, 1475 (1971).
4. P. Norton, Doctoral Dissertation, Syracuse University (1970); and P. Norton and H. Levinstein, Phys. Rev., to be published, June 1972.
5. S. M. Ryvkin, Photoelectric Effects in Semiconductors, Consultants Bureau, New York, (1964).
6. R. L. Aggarwal and A. K. Ramdas, Phys. Rev. 137, A602 (1965).
7. W. Kohn, Solid State Physics, Vol. 4, p.257 (ed. by F. Seitz and D. Turnbull), Academic Press, New York (1957).
8. S. H. Koenig, R. D. Brown and W. Schillinger, Phys. Rev. 128, 1668 (1962).
9. R. S. Levitt and A. Honig, J. Phys. Chem. Solids, 22, 269 (1961).
10. M. Loewenstein and A. Honig, Phys. Rev. 144, 781 (1966).
11. R. Leadon and J. A. Naber, J. Appl. Phys. 40, 2633 (1969).
12. R. A. Brown and S. Rodriguez, Phys. Rev. 153, 890 (1967).
13. J. R. Barker and C. J. Hearn, Phys. Letters 26A, 551 (1968).
14. R. A. Brown, Phys. Rev. 148, 974 (1966).

## UNCLASSIFIED

15. R. A. Brown and M. L. Burns, Phys. Letters 32A, 513 (1970).
16. It should be noted that the experimental results of Koenig et. al. (ref. 8) on shallow donors in germanium lie a factor of 5 above the theory of ref. 11. This theory predicts a larger cross-section for silicon donors, than for donors in in germanium, which is what we have found. It is felt that this theory, which was deliberately minimized, is likely to be in poorer agreement for silicon than for germanium because the binding energies of donors in silicon are about four times larger than donors in germanium. At any given temperature therefore, one should have to account for higher excited states in the case of silicon. Since only seven excited states were considered for both silicon and germanium, this would underestimate the cross-sections more in the case of silicon, than in germanium.

### QUESTION AND ANSWER SESSION

- Q. Have you seen any evidence for field effects on the recombination coefficient?
- A. Yes, when you do increase the field, the carrier lifetime gets longer in general; with copper, it tended to go as the  $1/2$  power of the electric field above a certain point. In silicon, it may have been a little steeper than that.

# UNCLASSIFIED

.... This paper is UNCLASSIFIED

## PLZT AND SBN PYROELECTRIC DETECTORS (U) (Unclassified)

S. T. Liu and O. N. Tufte  
Honeywell Corporate Research Center  
500 Washington Avenue South  
Hopkins, Minnesota 55343

### ABSTRACT

The material parameters of importance in pyroelectric detectors have been evaluated in  $\text{Pb}_{1-x}\text{La}_x(\text{Zr}_{0.65}\text{Ti}_{0.35})_{1-0.25x}\text{O}_3$  (PLZT) ferroelectric ceramics for  $x = 0.02$  to  $0.08$  and in single crystal  $\text{Sr}_{1-x}\text{Ba}_x\text{Nb}_2\text{O}_6$  (SBN) for  $x = 0.5$ . The noise sources in PLZT and SBN detectors have been evaluated and good agreement between the material parameters, noise measurements and detector performance for these two systems has been obtained. Significant reduction in the dielectric loss in  $x = 0.5$  SBN has enabled us to achieve a  $D^*$  of  $8.5 \times 10^8 \text{ cm(Hz)}^{1/2}/\text{W}$  at  $10\text{Hz}$ . A unique relationship between the pyroelectric coefficient, specific heat, density, and dielectric constant has been observed in the materials investigated and it is shown that this same relation is followed by a wide variety of ferroelectrics.

### INTRODUCTION

Recently, there has been an increasing interest in pyroelectric infrared detectors due to their unique characteristics of large responsivity, fast response, broad spectral sensitivity and room temperature operation. New materials, and improvements in existing materials are continually being investigated in an effort to improve the detector performance.

This paper reports measurements of the material parameters of importance for pyroelectric detectors for the  $\text{Pb}_{1-x}\text{La}_x(\text{Zr}_{0.65}\text{Ti}_{0.35})_{1-0.25x}\text{O}_3$  (PLZT)<sup>(1)</sup> ferroelectric ceramic materials having  $x = .02$  to  $.08$  and  $\text{Sr}_{1-x}\text{Ba}_x\text{Nb}_2\text{O}_6$  (SBN)<sup>(2)</sup> single crystals having  $x = 0.5$ . Pyroelectric detector samples have also been fabricated from these materials and the detector performance analyzed. The detector noise is shown to be thermal noise due to dielectric loss in the materials and this sets the practical performance limits for these materials.

### PRINCIPLES OF OPERATION

A pyroelectric detector is in essence an ac bolometer which differs from conventional bolometers in that it responds to the rate of change of temperature. The principle of operation of this device has been discussed extensively<sup>(2-5)</sup> and it suffices to summarize as follows:

#### (1) Signal

The steady state current generated in a pyroelectric detector when irradiated with an incident power,  $P(t) = P_0 + P_1 \exp(j\omega t)$ , is given by<sup>(4)</sup>

$$i = \frac{\eta p A P_1}{H} \frac{\omega \tau}{(1 + \omega^2 \tau^2)^{1/2}} = r_i (\eta P_1) \quad (1)$$

# UNCLASSIFIED

where

p = pyroelectric coefficient  
 H = heat capacity = cpdA  
 c = specific heat  
 ρ = density  
 d = thickness of the element  
 A = area of the element  
 G = thermal conductance  
 η = emissivity of the top surface electrode  
 τ = H/G  
 ω = angular frequency

and  $r_1$  is the current responsivity defined as

$$r_1 = \frac{i}{P_1} = \frac{\eta p}{c\rho} \frac{1}{d} \frac{\omega\tau}{(1+\omega^2\tau^2)^{1/2}} \quad (2)$$

Across the RC detector circuit, the voltage developed is

$$v = i \frac{R}{(1+\omega^2 R^2 C^2)^{1/2}} \quad (3)$$

It is easy to show that if  $(\omega\tau)^2 \gg 1$  and  $\omega^2 R^2 C^2 \gg 1$ , eq.(3) reduces to

$$v_{rms} \approx \xi \frac{\eta p_1}{2\sqrt{2}A} \frac{1}{\omega} \quad (3a)$$

where

$$\xi = \frac{p}{c\rho\epsilon\epsilon_c} \quad (4)$$

ε = the dielectric constant.

The voltage responsivity is defined as

$$R = \frac{v}{P_1} = \xi \eta \frac{1}{\omega A} \quad (5)$$

## (2) Noise

Several noise sources are possible in pyroelectric detectors; namely, radiation noise, temperature fluctuation noise, thermal noise of the detector, and noises of the amplifier. The contributions of these noise sources have been discussed in detail by Putley<sup>(4)</sup> and by van der Ziel and Liu.<sup>(5)</sup> Since radiation noise is negligible, the total noise current at a spot frequency is

$$\bar{i}_n^2 = 4kT \left\{ |r_1|^2 T_G + g_d + g_c + \frac{q}{2kT} (I_{g1} + I_{g2}) + R_n |Y_t|^2 \right\} \quad (6)$$

where

k = Boltzmann constant  
 T = absolute temperature  
 g<sub>d</sub> = detector conductance

# UNCLASSIFIED

$g_c$  = load conductance  
 $q$  = electronic charge  
 $I_{g1}, I_{g2}$  = FET gate currents  
 $R_n$  = equivalent noise resistance of the FET  
 $Y_t$  = the total circuit admittance

It can be described in terms of an equivalent noise conductance,  $g_n$ ; that is

$$g_n = |r_1|^2 |Y_t| + g_d + g_c + \frac{q}{2kT} (I_{g1} + I_{g2}) + R_n |Y_t|^2 \quad (6a)$$

The noise voltage is then

$$\overline{(V_N^2)}^{1/2} = (4kTg_n)^{1/2} \frac{R}{(1 + \omega^2 R^2 C^2)^{1/2}} \quad (7)$$

## (3) Noise equivalent power (NEP) and detectivity ( $D^*$ )

The signal-to-noise ratio of a pyroelectric detector for a system bandwidth  $\Delta f$  is given by

$$\frac{S}{N} = \frac{V_{rms}}{\overline{(V_N^2)}^{1/2}} = \frac{r_1(\omega) \eta P_1'}{\overline{(i_n^2)}^{1/2}} \quad (8)$$

The equivalent noise power (NEP) is defined as the value of  $P_1' = \frac{P_1}{2\Delta f}$  for which  $S/N = 1$  at a bandwidth of 1Hz. This yields

$$NEP = \frac{\overline{(i_n^2)}^{1/2}}{|r_1(\omega)| \eta} \quad (9)$$

The detectivity ( $D^*$ ) for thermal noise limited detectors is given as

$$D^* = A^{1/2}/NEP = \frac{\eta p}{cpd^{1/2}} \frac{1}{(4kT\omega\epsilon\epsilon_0 \tan\delta)^{1/2}} \quad (9a)$$

## EXPERIMENTAL PROCEDURE

The hot-pressed rhombohedral (PLZT)X/65/35 ceramics used in this study were prepared by Honeywell Ceramics Center, and the SBN crystals were grown and annealed by Dr. R. Maciolek of this laboratory. Samples approximately 80 $\mu$ m thick were prepared for this study by conventional lapping and polishing methods. Surface strain caused by polishing was relieved by annealing in air at 650°C for 20 minutes for PLZT. Aluminum/gold contacts were vacuum deposited onto both sample surfaces and the top electrode was blackened with thin black paint to make  $n \sim 1$ . The samples were poled by applying a dc electric field of 20 KV/cm in PLZT and 15 KV/cm in SBN samples for several hours. The dielectric constant and the dielectric loss were measured with a GR1620 capacitive bridge from 20 Hz to 100 KHz.

# UNCLASSIFIED

Absolute measurements of the pyroelectric material parameter  $\xi = \frac{P}{c\rho\epsilon_0}$  were made by two methods. The first method utilized sinusoidally modulated radiation from a calibrated 500°K blackbody source. Sinusoidal modulation is achieved with a mechanical chopper having an aperture diameter to tooth width ratio of 0.87.<sup>(7)</sup> The signal from the sample was measured with a low noise, high impedance amplifier. The peak irradiance in this case was  $P_1/A = 24.0 \mu\text{watts/cm}^2$  and the irradiance calibration was checked with a calibrated 5  $\mu\text{m}$  peak wavelength response  $\text{Hg}_{1-x}\text{Cd}_x\text{Te}$  detector. The pyroelectric material parameter  $\xi$  was then calculated directly from Eq. 3a. The thermal time constants for the detectors used in these experiments are sufficiently long that Eq. 3a can be used directly at the measurement frequency of 100 Hz used in these experiments. The second method utilized a pulse modulation technique.<sup>(8)</sup> In this case, the chopper and the aperture were arranged to give a trapezoidal pulse having an equivalent rectangular pulse width ( $T_1$ ) of 0.8 ms and a repetition rate of 30 pulses/sec. A peak irradiance of  $220 \mu\text{watt/cm}^2$  was used in these experiments. The peak response voltage,  $v_o$ , of the detector was measured and the material parameter was calculated from  $v_o = \xi T_1 P_1/A$ .

The frequency dependence of the pyroelectric detector signal was measured with a variable speed chopper. The detector noise was measured with a high impedance, low noise amplifier and a wave analyzer.

## RESULTS AND DISCUSSION

A comparison of the output waveforms obtained by the sinusoidal modulation method (100 Hz) and the pulse modulation method are shown in Figure 1. These results were obtained with a SBN ( $x = 0.5$ ) detector and the same amplifier gain is used in each case. The calculated material parameter obtained by the sinusoidal modulation method is  $920 \text{ cm}^2/\text{coul}$  compared with a value of  $900 \text{ cm}^2/\text{coul}$  for the pulse modulation method. Good agreement between the two methods was obtained on all detectors measured.

The measured pyroelectric material parameters for PLZT detector samples having lanthanum concentrations from  $x = 0.02$  to  $0.08$  are shown in Table I. Also shown are the measured dielectric constant and loss tangent values. The pyroelectric coefficients were calculated from using the measured values of dielectric constant, density, and the specific heat. The specific heat of  $c = 0.33 \text{ joule/gm}^\circ\text{C}$  was measured for a sample of  $x = 0.65$  and was assumed to be the same for other compositions. The pyroelectric coefficients for the higher  $x$  value PLZT ceramics are the largest that have been reported in ceramic ferroelectrics.

The measured values of the pyroelectric material parameters, dielectric constant and dielectric loss tangent for a group of SBN detector samples having a composition of  $x = 0.5$  are given in Table II. The detectors within each group were made from different portions of the same SBN single crystal so that a measure of the uniformity in the pyroelectric material properties both within a crystal and between crystals having nominally the same composition can be seen from these results. The pyroelectric coefficients were again calculated using values for  $c = 0.4 \text{ joule/gm}^\circ\text{C}$  and  $\rho = 5.33 \text{ gm/cm}^3$ .

The frequency dependence of the signal voltage, noise voltage and detectivity for a PLZT ( $x = 0.065$ ) detector is shown in Fig. 2. The signal is proportional to  $1/f$  for frequencies above 10 Hz indicating a slow thermal time constant for the detector. The noise is thermal noise and

# UNCLASSIFIED

is directly proportional to the dielectric loss. The magnitude of the calculated noise, given by  $(\frac{\sigma}{\epsilon})^{1/2} = (4kT\omega C \tan \delta)^{1/2}$ , agrees very well with the measured detector noise. The frequency independence of  $\tan \delta$ , which in terms of material parameters is equal to  $\frac{\sigma}{\omega \epsilon \epsilon_0}$ , is caused by the fact that the conductivity,  $\sigma$ , in PLZT is proportional to frequency. This is a common phenomena in ferroelectric and dielectric materials and results in the thermal noise only decreasing as  $1/f^{1/2}$  in pyroelectric detectors. The detectivity under this condition is given in Eq. (9a). And the detectivity also decreases as  $1/f^{1/2}$  as shown in Fig. 2. The detectivity given in Fig. 2 are typical of results attainable with properly poled PLZT ceramics having a thickness of 100  $\mu\text{m}$ .

Similar results on the frequency dependence of the signal, noise, and  $D^*$  for a SBN detector having a composition  $x \approx 0.5$  are given in Fig. 3. Thermal noise is also dominant in SBN detectors and the frequency dependence of the noise and the detectivity are similar to the PLZT detectors. The dielectric loss in the SBN material has been substantially reduced and this makes possible the high  $D^*$  values shown in Fig. 3. The  $D^*$  value in SBN at 10 Hz is as good as the best TGS detector that has been reported<sup>(9)</sup> and is within a factor of three (estimated) of the recently reported result of ATGS.<sup>(10)</sup> Self-depoling effects have not been observed in either SBN ( $x \approx 0.5$ ) or PLZT ( $x = 0.065$ ) detectors.

The pyroelectric material parameter  $\xi$  is an important quantity in the evaluation of ferroelectric materials for pyroelectric detector applications. The voltage responsivity,  $\mathcal{R}$ , of the detector is directly proportional to  $\xi$  and the value of  $\xi$  can be measured directly by either of the previously discussed methods. We have found empirically that  $\xi$  is closely related to the dielectric constant of the ferroelectric material and that this relationship is approximately the same for all classes of pyroelectric materials that have been investigated. This relationship is shown in Fig. 4 where the log of  $\xi$  is plotted against the log of  $\epsilon$  for the PLZT and SBN systems along with a number of other pyroelectric detector materials. The line in Fig. 4 is a close fit to the data points and the line follows the relation

$$\xi = 2.8 \times 10^4 / \epsilon^{0.6} \quad (10)$$

The PLZT samples having low lanthanum concentrations ( $x < 0.04$ ) fall slightly below this line but this is attributed to the difficulty in completely poling the samples. The empirical relation between  $\xi$  and  $\epsilon$  that occurs even between different types of ferroelectric materials (such as TGS and PLZT) is rather surprising and suggests that a fundamental relationship may exist between these parameters. In selecting new ferroelectric materials for pyroelectric detector application, Eq. (10) can be used to predict the voltage responsivity attainable on the basis of only the dielectric constant.

## CONCLUSION

We have measured the pyroelectric material parameter  $\xi$  in SBN and PLZT materials utilizing both sinusoidally modulated and pulse modulated blackbody radiation and have shown that the two methods give the same results. We have measured the material parameters of importance for pyroelectric detectors in SBN ( $x \approx 0.5$ ) and PLZT ( $x = 0.02$  to  $0.08$ ) and have shown that the thermal noise is dominant in PLZT and SBN detectors. The dielectric loss tangent has been substantially reduced in SBN ( $x \approx 0.5$ ) material to the point that detectivity values of  $D^*(500, 10, 1) = 8.5 \times 10^8 \text{ cm(Hz)}^{1/2}/\text{watt}$  have been obtained. The performance of PLZT ( $x = 0.065$ ) detectors is limited by



## UNCLASSIFIED

thermal noise due to the relatively high dielectric loss in the present material. However, detectivity values of  $D^*(500,10,1)$  of  $3 \times 10^8 \text{ cm(Hz)}^{1/2}/\text{watt}$  have been attained and improved performance is possible. Since these materials are ceramics, good uniformity can be obtained over large areas and the materials can easily be fabricated into detectors.

We have also shown that the pyroelectric material parameter  $\xi$  is uniquely related to the dielectric constant in all ferroelectric materials and this relationship should be useful for predicting the voltage responsivity for detectors made from new pyroelectric materials.

### REFERENCES

1. S. T. Liu, J. D. Heaps, and O. N. Tufte, "The Pyroelectric Properties of the Lanthanum-doped Ferroelectric PLZT Ceramics," presented at 1971 IEEE Symposium on Applications of Ferroelectrics at Yorktown Heights, New York.
2. A. M. Glass, "Investigation of the Electrical Properties of  $\text{Sr}_{1-x}\text{Ba}_x\text{Mn}_2\text{O}_6$  with Special Reference to Pyroelectric Detection," J. Appl. Phys. 40, 4699-4713 (1969).
3. A. M. Glass and R. L. Abrams, "Pyroelectric Detection of Infrared Radiation," Proc. of the Special Meeting on Unconventional Infrared Detectors, 59-70 (1971).
4. E. H. Putley, "Pyroelectric Detectors in Semiconductors and Semimetals, edited by R. K. Willardson and A. C. Beer (Academic Press, N. Y. 1970). Vol. 5.
5. G. A. Burdick and R. T. Arnold, "Theoretical Expression for the Noise Equivalent Power of Pyroelectric Detectors," J. Appl. Phys. 37, 3223-3226, (1966).
6. A. van der Ziel and S. T. Liu, "Noise Sources in Pyroelectric Radiation Detectors," Physica (to be published).
7. R. B. McQuistan, "On an Approximation to Sinusoidal Modulation," J. Opt. Soc. Am. 48, 63-66 (1958).
8. A. Shanlov and M. Simhony, "Peak Voltage of the Pyroelectric Response to Short Infrared Laser Pulses," Appl. Phys. Lett. 18, 6-7 (1972); A. G. Chynoweth, "Dynamic Method for Measuring the Pyroelectric Effect with Special Reference to Barium Titanate," JAP 27, 78-84 (1956).
9. H. Beerman, "Improvement in the Pyroelectric IR Radiation Detector," Ferroelectrics 2, 123-128 (1971).
10. P. J. Lock, "Doped TGS for Pyroelectric Applications," Appl. Phys. Lett. 19, 390-391 (1971).
11. E. Yamaka, T. Hayashi, and M. Matsumoto, " $\text{PbTiO}_3$  Pyroelectric Infrared Detector," Infrared Phys. 11, 247-248 (1971).

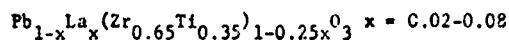
### QUESTION AND ANSWER SESSION

- Q. What was the temperature of operation and is performance temperature dependent?
- A. Operating temperature was  $25^\circ\text{C}$  (i.e. room temperature) and I'm led to believe that performance is not temperature dependent.

# UNCLASSIFIED

TABLE I

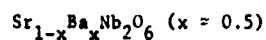
MEASURED PYROELECTRIC MATERIAL PARAMETERS:



DETECTORS	$\epsilon$	$\tan\delta$	$\xi \left( \frac{\text{cm}^2}{\text{coul}} \right)$	$p \left( \frac{\text{coul}}{\text{cm}^2 \cdot ^\circ\text{C}} \right)$
$x = 0.02$	600	0.02	282	$3.9 \times 10^{-8}$
$x = 0.04$	680	0.015	330	$5.2 \times 10^{-8}$
$x = 0.065$	1400	0.018	340	$10.0 \times 10^{-8}$
$x = 0.07$	1860	0.01	330	$13.0 \times 10^{-8}$
$x = 0.075$	3200	0.02	210	$15.3 \times 10^{-8}$
$x = 0.08$	3800	0.02	195	$17.0 \times 10^{-8}$

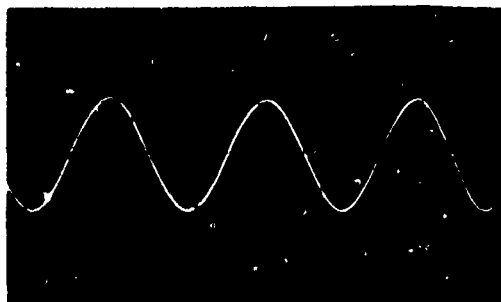
TABLE II

MEASURED PYROELECTRIC MATERIAL PARAMETERS:

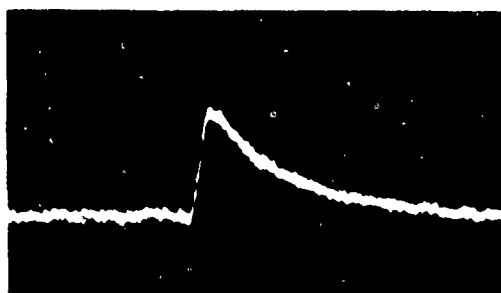


DETECTORS	$\epsilon$	$\tan\delta$	$\xi \left( \frac{\text{cm}^2}{\text{coul}} \right)$	$p \left( \frac{\text{coul}}{\text{cm}^2 \cdot ^\circ\text{C}} \right)$
925-1	448	.015	845	$7.5 \times 10^{-8}$
925-2	456	.024	860	$7.76 \times 10^{-8}$
925-3	458	.007	860	$7.8 \times 10^{-8}$
1020-3	449	.005	845	$7.5 \times 10^{-8}$
1020-4	438	.003	890	$7.7 \times 10^{-8}$
1125-6a	400	.010	875	$6.93 \times 10^{-8}$
1125-6b	390	.0036	850	$6.53 \times 10^{-8}$
1230-1	396	.0033	940	$7.50 \times 10^{-8}$
208-3	390	.005	960	$7.40 \times 10^{-8}$
308-2	402	.004	940	$7.48 \times 10^{-8}$
308-4	390	.003	970	$7.48 \times 10^{-8}$

UNCLASSIFIED



(a)



(b)

Fig. 1. Response of a SBN detector to (a) sinusoidally modulated blackbody radiation (filtered and amplified 100x further); (b) pulse-modulated blackbody radiation (wide band).

Scales Horizontal: 4 ms/major division  
(a) Vertical: 200 mV/major division  
(b) Vertical: 10 mV/major division

UNCLASSIFIED

UNCLASSIFIED

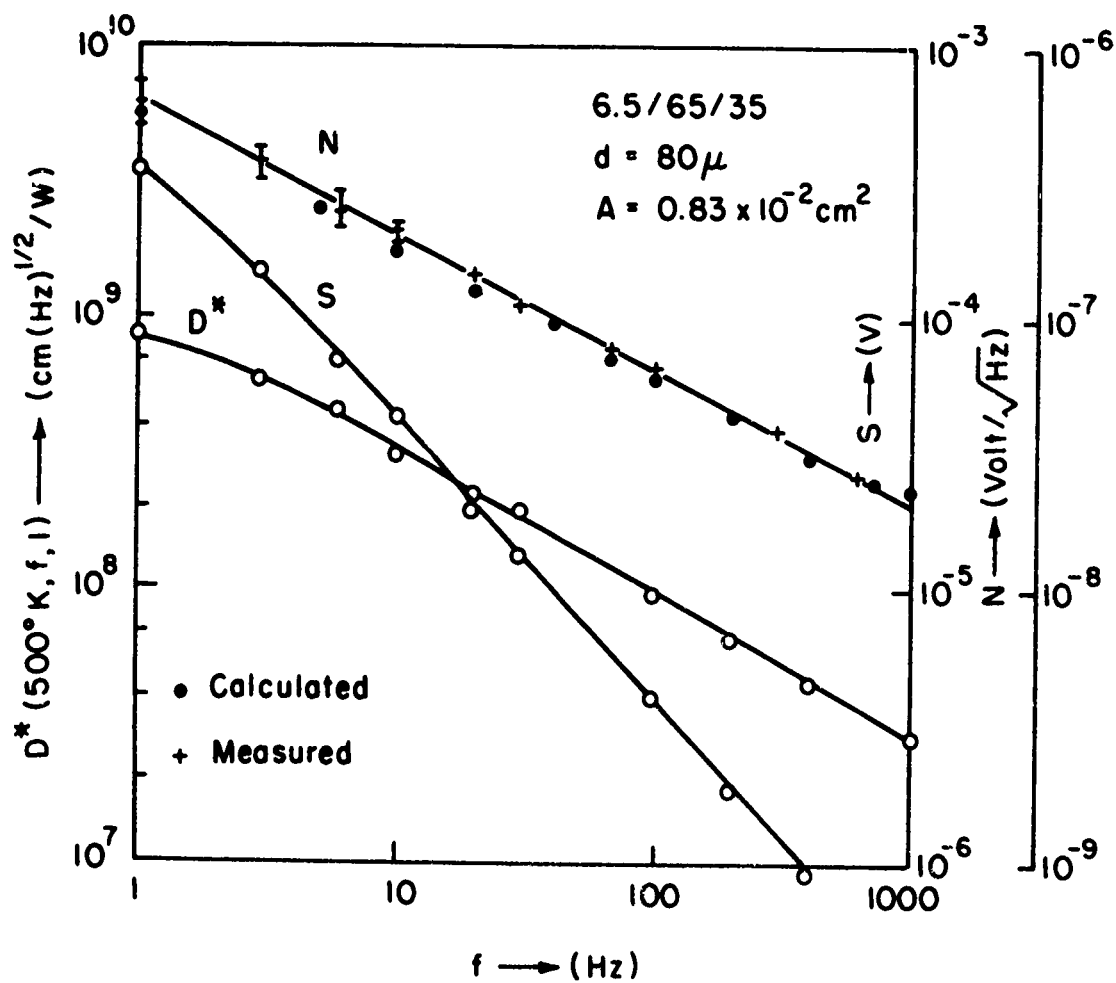


Fig. 2. Performance of a PLZT Detector.

UNCLASSIFIED

UNCLASSIFIED

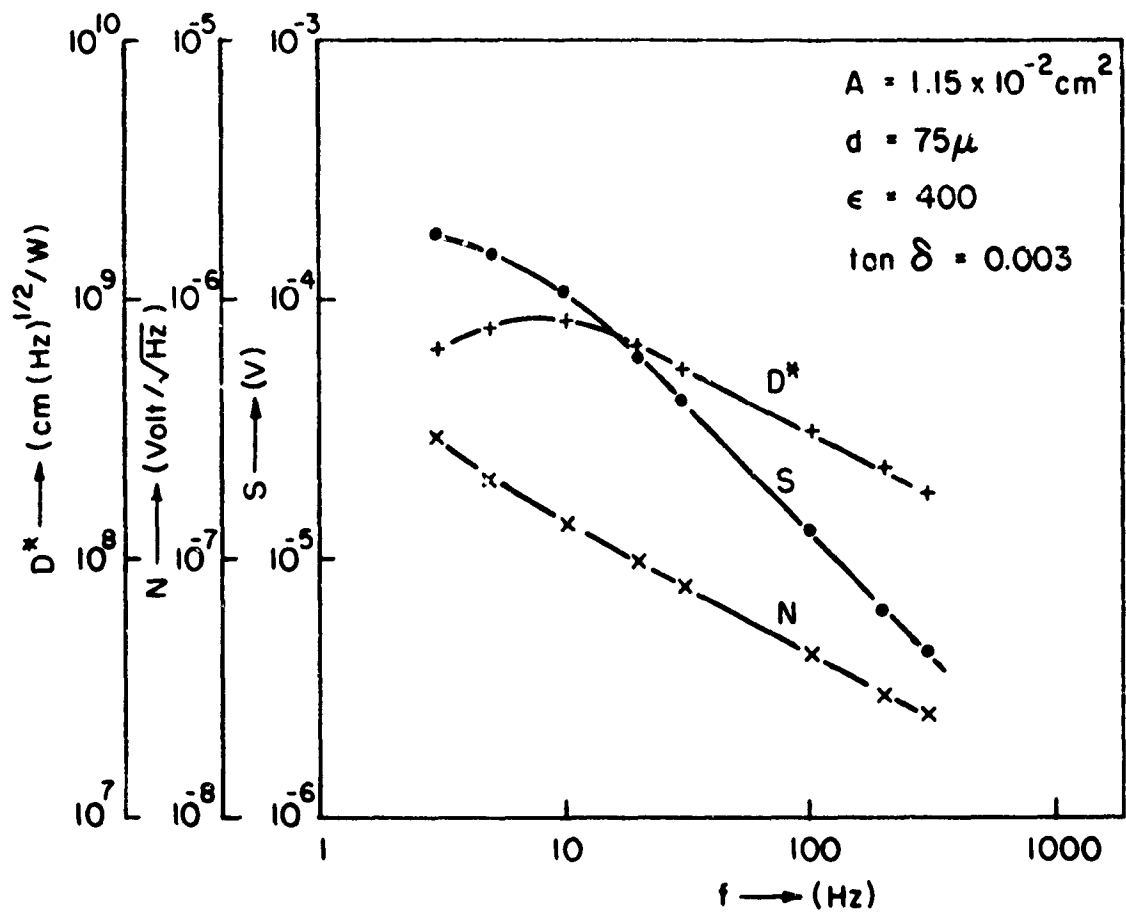


Fig. 3. Performance of a SBN Detector.

UNCLASSIFIED

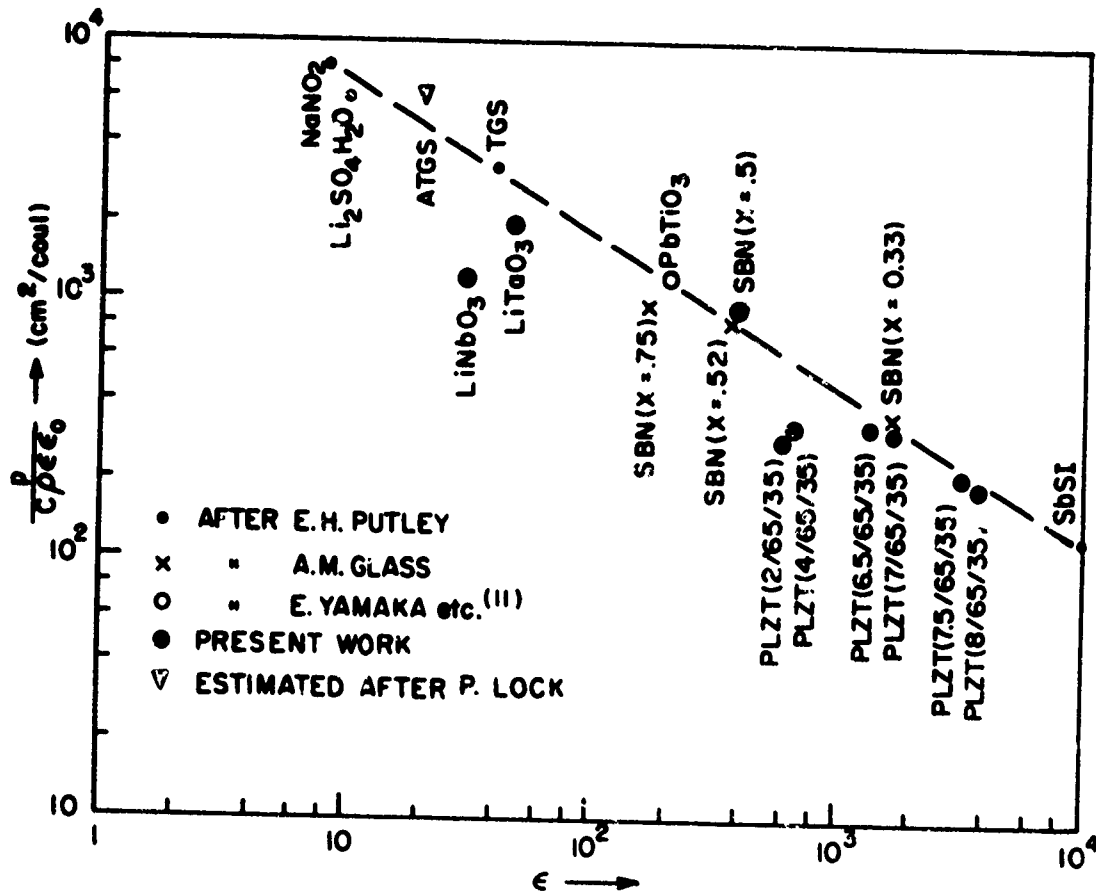


Fig. 4. Material Parameter vs Dielectric Constant.

Reverse page blank

# UNCLASSIFIED

.... This paper is UNCLASSIFIED

## POLYMERIC PYROELECTRIC DETECTOR<sup>†</sup> (Unclassified)

J. Cohen, C. F. Vezzetti, and S. Edelman  
National Bureau of Standards  
Washington, D. C. 20234

### ABSTRACT (Unclassified)

Polymers have a number of advantages over conventional pyroelectric materials such as triglycine sulphate crystals; for example, they are not hygroscopic, retain their polarization for long times, and are simple and inexpensive to fabricate into detectors. We have been experimenting mainly with films of polyvinylidene fluoride, and to a lesser extent, polyvinylfluoride. These experiments will be described.

---

Polyvinylidene fluoride, or PVF<sub>2</sub>, is a crystalline polymer, highly susceptible to ordering and concomitant enhancement of crystallinity by drawing, as reported by Brown and Crawford<sup>(1)</sup> further, electrical measurements have shown the material to contain permanent dipoles<sup>(2)</sup>. To obtain pyroelectricity, films of this material are first stretched 200 - 300%, then poled by applying a field of 400 - 500 kV/cm across the thickness, at about 100°C for a few hours, and cooled with the field applied. The procedure with polyvinylfluoride, or PVF, also a crystalline polymer, is similar, except we did not stretch the material first.

The first figure shows, on top, a schematic diagram of the demountable detector, which is convenient for rapid interchange of different detector elements. The polymer film, coated with semitransparent metal films on both faces, is attached to a copper heat sink with a little silver paste, and the aperture in the sink defines the active area. The heat sink is connected to the shell of the minibox, which is grounded, thus grounding the front face of the polymer film. The back surface of the polymer is connected to the source follower with a dab of silver paste. The detector element may be regarded as an "infinite" impedance and some sort of impedance matching is required to drive external circuitry. A circuit diagram of the simple source follower used is shown at the lower portion of the figure. A more suitable circuit could be designed.

Figure 2 shows the detectivity, D\*, and the responsivity of a PVF<sub>2</sub> detector as a function of chopping frequency. A 500 K blackbody source was used. Note that at 2.5 Hz, D\* is  $1 \times 10^8 \text{ cm Hz}^{1/2} \text{ W}^{-1}$  and the responsivity is  $3200 \text{ VW}^{-1}$ . The variation of responsivity and D\* with frequency depends on the circuitry used. Improved circuitry would lessen the dropoff with frequency. The D\* is approaching that of the usual TGS pyroelectric detector, and is about an order of magnitude below the best.

---

<sup>†</sup> Partly supported by the Night Vision Laboratory, Office of Naval Research and Advanced Research Projects Agency.

## UNCLASSIFIED

Figure 3 shows selected examples of  $D^*$  as a function of chopping frequency for three kinds of poled polymer film: unstretched PVF<sub>2</sub>, uniaxially stretched PVF<sub>2</sub>, and unstretched PVF. These curves are not necessarily typical, as we do not yet have a sufficient sampling. Nevertheless, stretching PVF<sub>2</sub> does appear to cause a large increase in the detectivity, and this is due to increased responsiveness.

A few remarks concerning the mechanism of pyroelectricity in polymers are in order. First, this is a very new field; polymers are complex materials, and all sorts of complicated processes may occur as a result of the intense electrical fields applied during poling; for example, ionization, electrolysis, and emission. Consequently the phenomenon is not well understood. I would like to suggest a model, however, based on our own experience to date and related published literature. It has been reported by Lando, Olf and Peterlin<sup>(2)</sup> that stretching PVF<sub>2</sub> causes a transformation from the  $\alpha$ -to the  $\beta$ -phase, in which C-F dipoles which were parallel to the plane of the film become oriented normal to the plane of the film. The electric field applied normal to the film plane then enhances this normal orientation. We believe that the pyroelectricity is a consequence of the change in the dipole moment of the dipoles that are oriented normal to the plane of the film, due to change in temperature. PVF has been reported<sup>(2)</sup> to have very strong structural similarities to  $\beta$ -PVF<sub>2</sub>, and we presume that the mechanism of pyroelectricity is also similar. A related article on pyroelectric properties of PVF<sub>2</sub> was published by Glass, McFee and Bergman<sup>(3)</sup>.

We are currently working on the problem of the mechanism of pyroelectricity in polymers, and hope through combined studies of pyroelectricity, piezoelectricity, and elasticity, to be able, in the future, to present a more definitive model.

### REFERENCES

1. H. A. Brown and G. H. Crawford, Science and Technology of Polymer Films, O. J. Sweeting, ed., Wiley - Interscience, New York (1971).
2. J. B. Lando, H. G. Olf, and A. Peterlin, J. Poly. Sci., A-1, 4, 94 (1966).
3. A. M. Glass, J. H. McFee, and J. G. Bergman, Jr., J. Appl. Phys. 42, 5219 (1971).

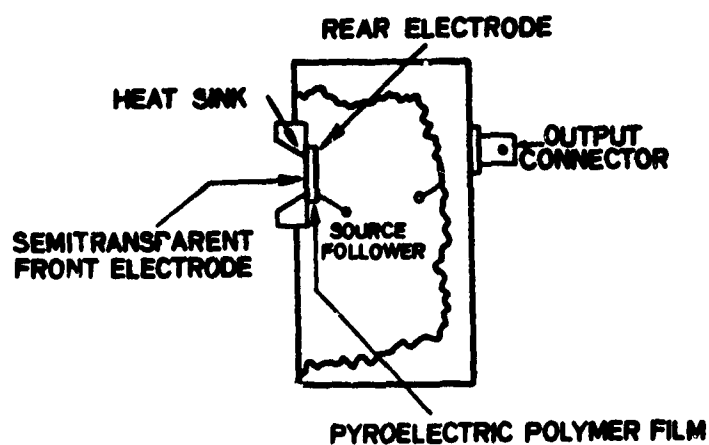
### QUESTION AND ANSWER SESSION

Q. How stable are these detectors?

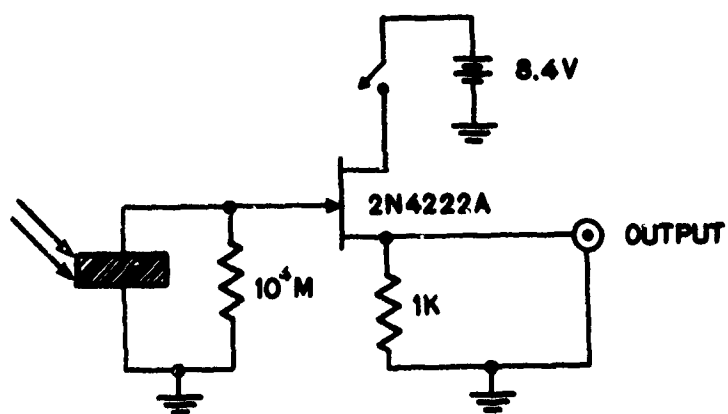
A. Over a year, that we know of, at room temperature.



UNCLASSIFIED



SCHEMATIC DIAGRAM OF DETECTOR



CIRCUIT DIAGRAM OF SOURCE FOLLOWER

FIGURE 1. Top: SCHEMATIC DIAGRAM OF DETECTOR  
Bottom: CIRCUIT DIAGRAM OF SOURCE FOLLOWER

UNCLASSIFIED

UNCLASSIFIED

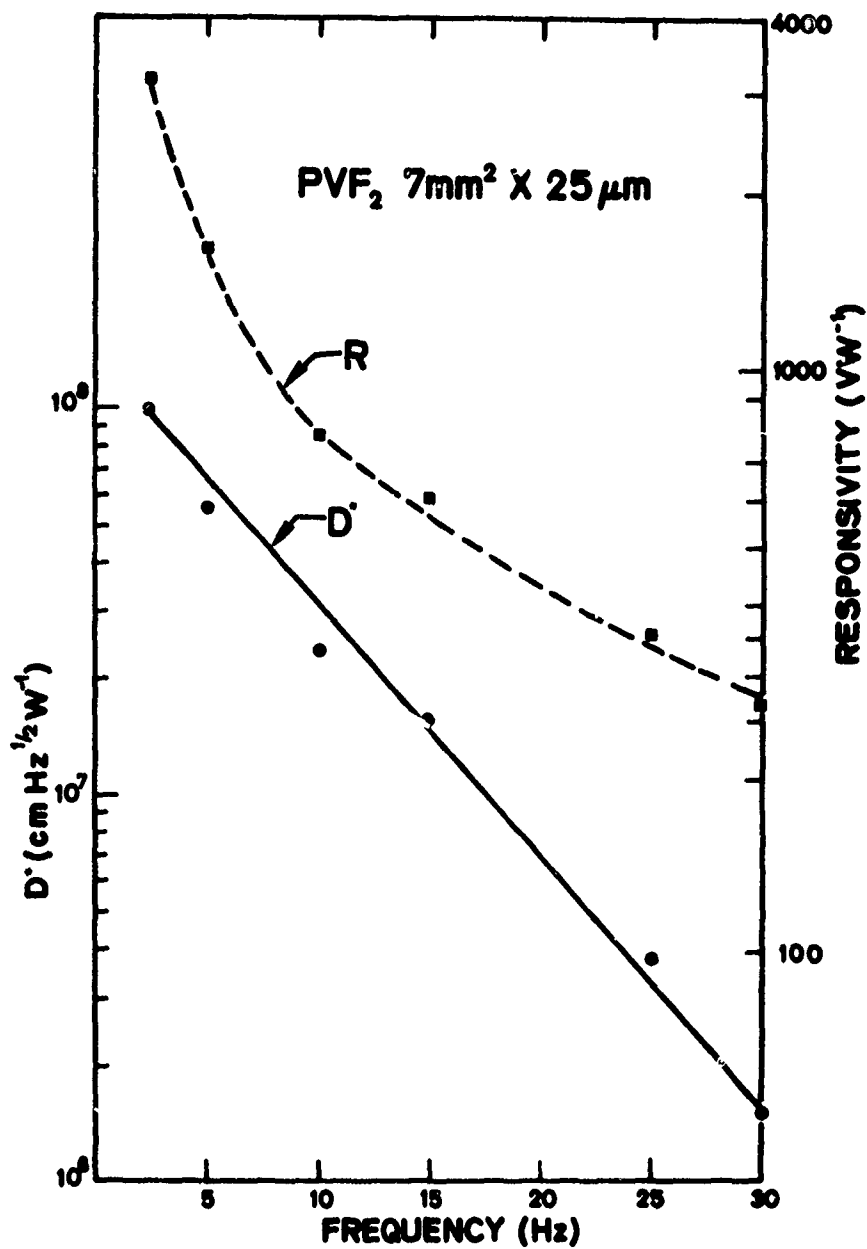


FIGURE 2. DETECTIVITY AND RESPONSIVITY OF PVF<sub>2</sub>  
AS A FUNCTION OF CHOPPING FREQUENCY

UNCLASSIFIED

UNCLASSIFIED

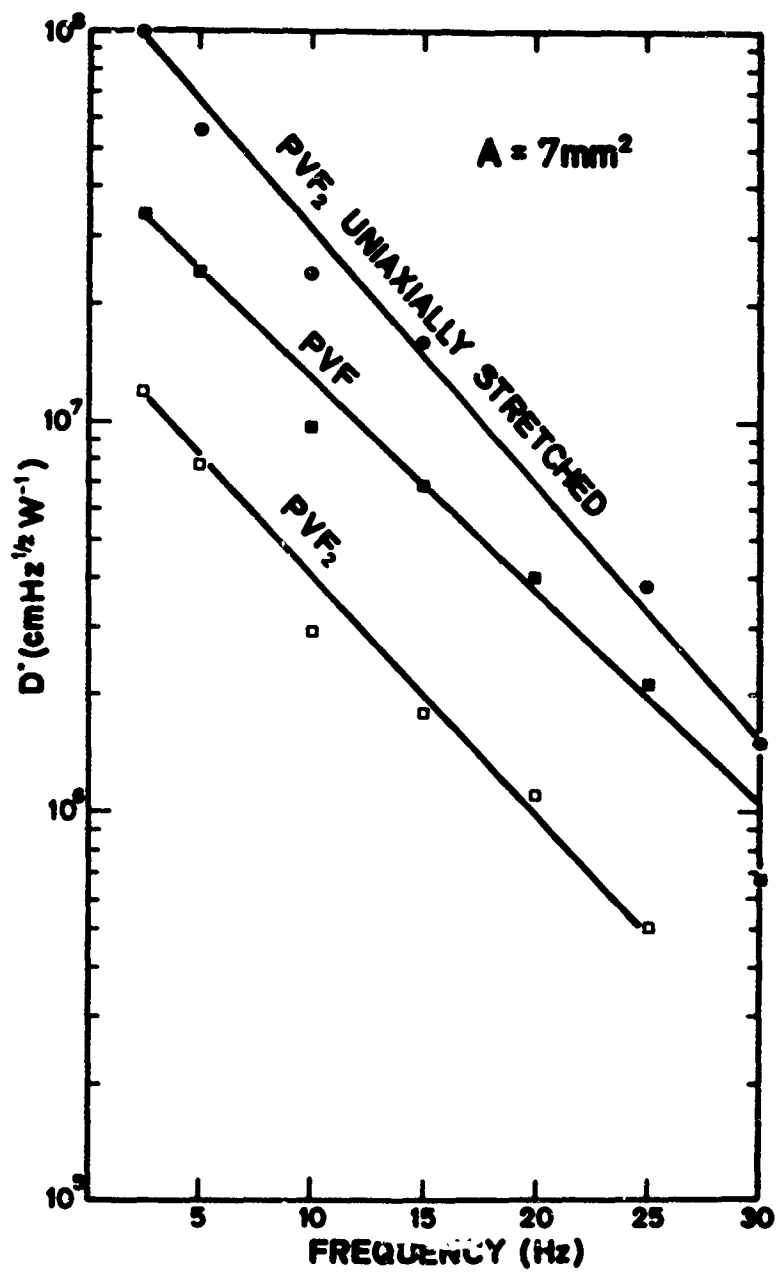


FIGURE 3. SELECTED EXAMPLES OF  $D^*$   
AS A FUNCTION OF CHOPPING FREQUENCY

Reverse page blank

UNCLASSIFIED

# UNCLASSIFIED

.... This paper is UNCLASSIFIED

## IMPROVED IRQC PERFORMANCE OF $\text{CdF}_2:\text{Er}^{3+}$ BY GENERATION OF $C_{2v}$ AND $C_{3v}$ LOCAL SITE SYMMETRY (U) (Unclassified)

N. E. Byer, T. C. Ensign, and W. M. Mularie  
Research Institute for Advanced Studies  
(RIAS)

Martin Marietta Corporation  
1450 South Rolling Road  
Baltimore, Maryland 21227

### ABSTRACT

Selective generation of trigonal ( $C_{3v}$ ) symmetry at  $\text{Er}^{3+}$  ions in  $\text{CdF}_2$  by oxygen-firing increases the green ( $^4S_{3/2} \rightarrow ^4I_{15/2}$ ) radiative efficiency from 1.9% to 52% while causing qualitative changes in the optical absorption and emission associated with these ions. Dramatic changes were observed also for  $\text{CdF}_2:\text{Er}^{3+}$  crystals, compensated by monovalent cations. Measurements of the parameters involved in the operation of an IRQC suggest that the oxygen-fired material could be used to construct an uncooled infrared detector having a minimum detectable power of  $3.6 \times 10^{-14} \text{ W}$  at  $1.53 \mu\text{m}$ , appreciably better than currently available uncooled detectors sensitive at this wavelength.

Although the attractiveness of a room temperature infrared detector based on the Bloembergen<sup>(1)</sup> InfraRed Quantum Counter (IRQC) has been emphasized in several studies,<sup>(2,3)</sup> practical devices have not yet been realized. One of the principal limitations on progress in this area has arisen from difficulties in obtaining efficient materials that also satisfy specific spectral requirements. The results described in this paper suggest that these problems may be overcome to an important degree through adequate control over the processes employed in preparing the materials.

An IRQC scheme proposed<sup>(4)</sup> for detecting  $1.536 \mu\text{m}$  radiation from an Er:phosphate glass laser<sup>(5)</sup> is shown schematically in Fig. 1. IRQC action involves successive excitation of the  $\text{Er}^{3+}$ :<sup>(6,7)</sup> first from the  $^4I_{15/2}$  ground state to the  $^4I_{13/2}$  state by the signal radiation, and from there to the  $^4S_{3/2}$  state by an 840 nm GaAlAs laser pump. The 540 nm ( $^4S_{3/2} \rightarrow ^4I_{15/2}$ ) or 660 nm ( $^4F_{9/2} \rightarrow ^4I_{15/2}$ ) emission that results during relaxation back to the ground state is detected by a photomultiplier tube. To optimize overall detector sensitivity, the absorption cross sections at the signal and pump wavelengths, the lifetime of the  $^4I_{13/2}$  state, and the radiative efficiencies of the  $^4S_{3/2}$  or the  $^4F_{9/2}$  states must be maximized. Because these parameters depend on the local crystalline field at the  $\text{Er}^{3+}$ , previous workers<sup>(8)</sup> have attempted to increase sensitivity by finding the most desirable host. Even in a particular host, however, the specific character of the charge compensation can alter significantly the local crystalline field<sup>(9)</sup> and thereby influence the sensitivity.<sup>(4)</sup> A coordinated study of the electron paramagnetic resonance (EPR) and optical characteristics of  $\text{Er}^{3+}$  in  $\text{CdF}_2$  has been performed, therefore, to determine: 1) the local site symmetries at the  $\text{Er}^{3+}$  ion resulting from various modes of charge compensation, and 11) the IRQC parameters associated with  $\text{Er}^{3+}$  in these sites. The results obtained for  $\text{Er}^{3+}$  in a trigonal site generated by oxygen compensation and an orthorhombic site generated by monovalent

UNCLASSIFIED

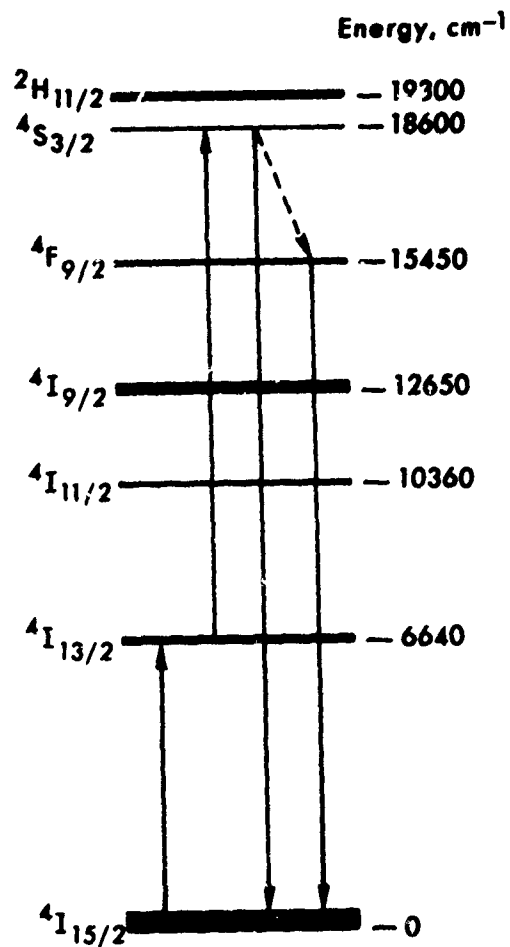


FIGURE 1. ENERGY LEVEL DIAGRAM FOR  $Er^{3+}$  IN  $CdF_2$ . Optical transitions relevant to IRQC action are indicated by arrows. The thickness of the energy level is proportional to the width of the multiplet.

UNCLASSIFIED

# UNCLASSIFIED

cation doping are summarized in this paper.

The primary IRQC materials investigated in these studies have been  $\text{CdF}_2$  single crystals containing 0.1 mole %  $\text{ErF}_3$ , which have been grown by the Bridgman-Stockbarger technique in an evacuated vessel. Three modes of sample preparation have been employed: (i) crystals in which no intentional charge compensation was provided,  $\text{CdF}_2:(\text{Er}^{3+}, \text{U})$ ; (ii) crystals which have been fired subsequent to growth in dry oxygen at  $800^\circ\text{C}$  for periods up to 20 hrs,  $\text{CdF}_2:(\text{Er}^{3+}, \text{O}^{2-})$ ; and (iii) crystals in which monovalent cations (i.e.,  $\text{Li}^+$ ,  $\text{Na}^+$ ,  $\text{K}^+$ , and  $\text{Ag}^+$ ) have been introduced as the metal fluoride prior to growth,  $\text{CdF}_2:(\text{Er}^{3+}, \text{M}^+)$ . The EPR and optical results obtained for  $(\text{Er}^{3+}, \text{M}^+)$  crystals have been found to be similar, and only those data tabulated for  $\text{CdF}_2:(\text{Er}^{3+}, \text{Na}^+)$  will be reported in this paper.

Table I shows the relative distribution of  $\text{Er}^{3+}$  sites as determined by EPR for these three types of  $\text{CdF}_2$  specimens. For  $\text{CdF}_2:(\text{Er}^{3+}, \text{U})$  ~75% of the  $\text{Er}^{3+}$  ions reside in cubic ( $\text{O}_h$ ) symmetry;

TABLE I. THE RELATIVE DISTRIBUTION OF  $\text{Er}^{3+}$  LOCAL SITES FOR SEVERAL DIFFERENTLY PREPARED  $\text{CdF}_2$  CRYSTALS

SAMPLE	$\text{Er}^{3+}$ LOCAL SITES (%)			
	CUBIC	ORTHORHOMBIC	TRIGONAL	OTHER NONCUBIC
$(\text{Er}^{3+}, \text{U})$	75	-	-	25
$(\text{Er}^{3+}, \text{Na}^+)$	50	> 49	-	< 1
$(\text{Er}^{3+}, \text{O}^{2-})$	7	-	80	13

the remaining ~25% of the ions are located in several different noncubic sites for which the symmetry has not been determined. As summarized in Table I, the EPR spectrum of  $\text{CdF}_2:(\text{Er}^{3+}, \text{Na}^+)$  has been shown to arise almost equally from  $\text{Er}^{3+}$  in sites having cubic ( $\text{O}_h$ ) or orthorhombic ( $\text{C}_{2v}$ ) symmetry.<sup>(9)</sup> The latter symmetry is consistent with that expected if a monovalent cation is substituted for a nearest neighbor  $\text{Cd}^{2+}$  ion, as illustrated in Fig. 2b. Moreover, these  $\text{C}_{2v}(\text{Er}^{3+}, \text{Na}^+)$  centers account for nearly all (> 99%) of the noncubic sites recorded for the  $\text{CdF}_2:(\text{Er}^{3+}, \text{Na}^+)$  crystals, which has permitted an unambiguous characterization of the  $(\text{Er}^{3+}, \text{Na}^+)$  center. After  $\text{CdF}_2:(\text{Er}^{3+}, \text{U})$  crystals have been fired in oxygen at  $800^\circ\text{C}$  for 20 hours, EPR measurements indicate that 80% of the  $\text{Er}^{3+}$  reside in sites having trigonal ( $\text{C}_{3v}$ ) symmetry, whereas only 7% remain in  $\text{O}_h$  symmetry.<sup>(4,9)</sup> Thus, in  $\text{CdF}_2:(\text{Er}^{3+}, \text{O}^{2-})$  crystals, the  $\text{C}_{3v}$  sites accommodate more than 86% of the  $\text{Er}^{3+}$  ions that reside in noncubic sites. As for the  $\text{C}_{2v}(\text{Er}^{3+}, \text{Na}^+)$  center discussed previously, the  $\text{C}_{3v}(\text{Er}^{3+}, \text{O}^{2-})$  center has been identified and characterized with respect to the optical properties that are relevant to IRQC operation.

These EPR studies have demonstrated that specific kinds of  $\text{Er}^{3+}$  sites can be generated preferentially by applying suitable chemical treatments during crystal growth or subsequently.

UNCLASSIFIED

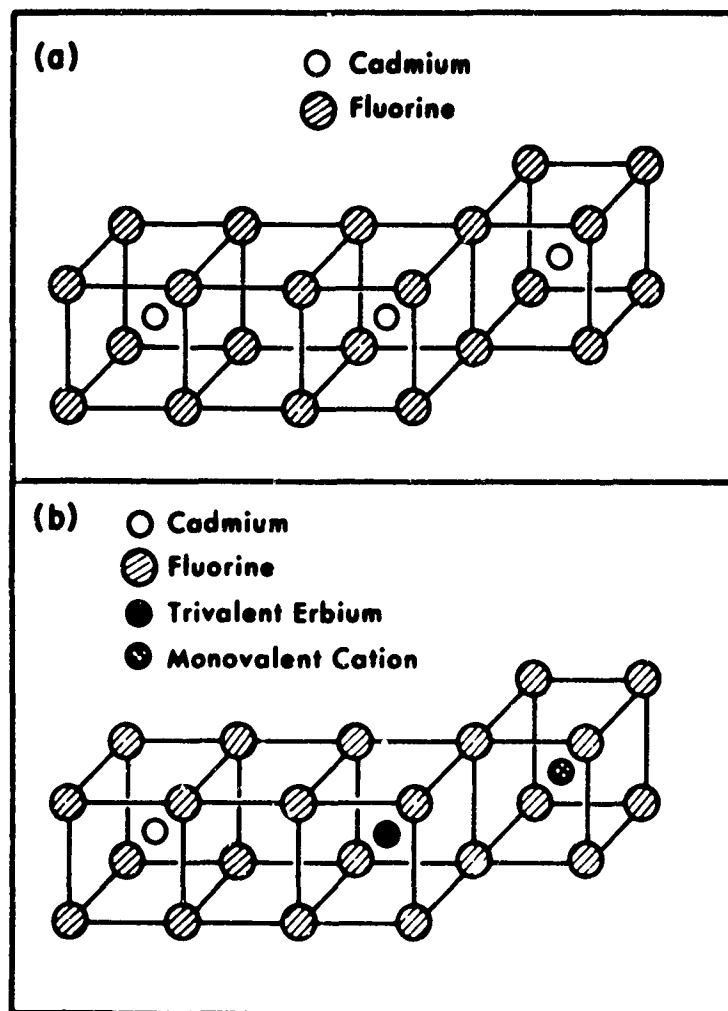


FIGURE 2. FLUORITE CRYSTAL STRUCTURE OF  $\text{CdF}_2$ . The  $\text{CdF}_2$  lattice (a) in the pure state; (b) showing an  $\text{Er}^{3+}$  ion substituting for a  $\text{Cd}^{2+}$  ion with charge compensation provided by a monovalent cation (e.g.,  $\text{Na}^+$ ) located along a  $\langle 110 \rangle$  crystal direction.

UNCLASSIFIED

# UNCLASSIFIED

Moreover, characteristic changes in the optical properties of  $\text{Er}^{3+}$  accompany these treatments. As a result, the optical properties of  $\text{Er}^{3+}$  ions in these sites can be correlated unambiguously with specific mechanisms for charge compensation. In particular, striking changes in the optical absorption spectrum are caused by  $\text{O}^{2-}$  compensation as illustrated in Fig. 3. Similar changes were observed with  $\text{Na}^+$  compensation. Not only are the absorption peaks sharper and better defined for the  $(\text{Er}^{3+}, \text{O}^{2-})$  sample, but the centroid of the absorption spectrum has been displaced to longer wavelengths. Undoubtedly, the ill-defined spectrum for the  $(\text{Er}^{3+}, \text{U})$  material is a result of the overlapping spectra associated with  $\text{Er}^{3+}$  on the wide variety of different non cubic sites observed in EPR measurements.

The structure and intensity of the emission spectrum also are altered dramatically by sample treatment. In particular, the luminescent efficiencies  $\eta_R$  or  $\eta_G$ , defined as the number of red ( $^4\text{F}_{9/2} \rightarrow ^4\text{I}_{15/2}$ ) or green ( $^4\text{S}_{3/2} \rightarrow ^4\text{I}_{15/2}$ ) photons emitted per electron excited into the  $^4\text{S}_{3/2}$  level, are compared for  $(\text{Er}^{3+}, \text{U})$ ,  $(\text{Er}^{3+}, \text{Na}^+)$  and  $(\text{Er}^{3+}, \text{O}^{2-})$  crystals in Table II. The most dramatic

TABLE II. THE LUMINESCENT EFFICIENCY,  $\eta$ , AND THE CONVERSION EFFICIENCY,  $\gamma$ , AT 295K FOR DIFFERENTLY PREPARED CRYSTALS OF  $\text{CdF}_2:0.1$  MOLE %  $\text{ErF}_3$ , TOGETHER WITH THE ANTICIPATED MDP.

SAMPLE	$\eta$ (%)		$\gamma$ ( $10^{-6} \text{ cm}^2 \text{ W}^{-1}$ )		MDP ( $10^{-14} \text{ W}$ )	
	$\eta_G$	$\eta_R$	$\gamma_G$	$\gamma_R$	Green	Red
$(\text{Er}^{3+}, \text{U})$	2.3	21	0.5	4.2	190	350
$(\text{Er}^{3+}, \text{Na}^+)$	20	1.1	2.5	0.15	37	9600
$(\text{Er}^{3+}, \text{O}^{2-})$	52	2	26	1	3.6	1400

change is that the dominant red emission of the  $(\text{Er}^{3+}, \text{U})$  material is replaced by an efficient ( $\eta_G=52\%$ ) green emission from the  $(\text{Er}^{3+}, \text{O}^{2-})$  crystal. The magnitude of these changes in efficiency emphasize the danger of characterizing an IRQC material by host crystal and dopant alone.

Table II shows also the overall conversion efficiency,  $\gamma$ , defined as the number of green ( $\gamma_G$ ) or red ( $\gamma_R$ ) photons emitted for each  $1.5 \mu\text{m}$  photon absorbed, when the crystal is illuminated by a pump (840 nm) at an intensity,  $I_p$ , of  $1 \text{ W/cm}^2$ .  $\gamma$  is a measure of the intrinsic capabilities of the material for IRQC applications, independent of pump intensity.\* Oxygen-firing is seen to have caused a 50-fold increase in the conversion efficiency for generating green photons.

\*  $\gamma_G$  and  $\gamma_R$  were determined experimentally for  $I_p = 6 \text{ mW/cm}^2$ , but are expected to be independent of  $I_p$  for all pump intensities available at present (c.f. Ref. 2).



UNCLASSIFIED

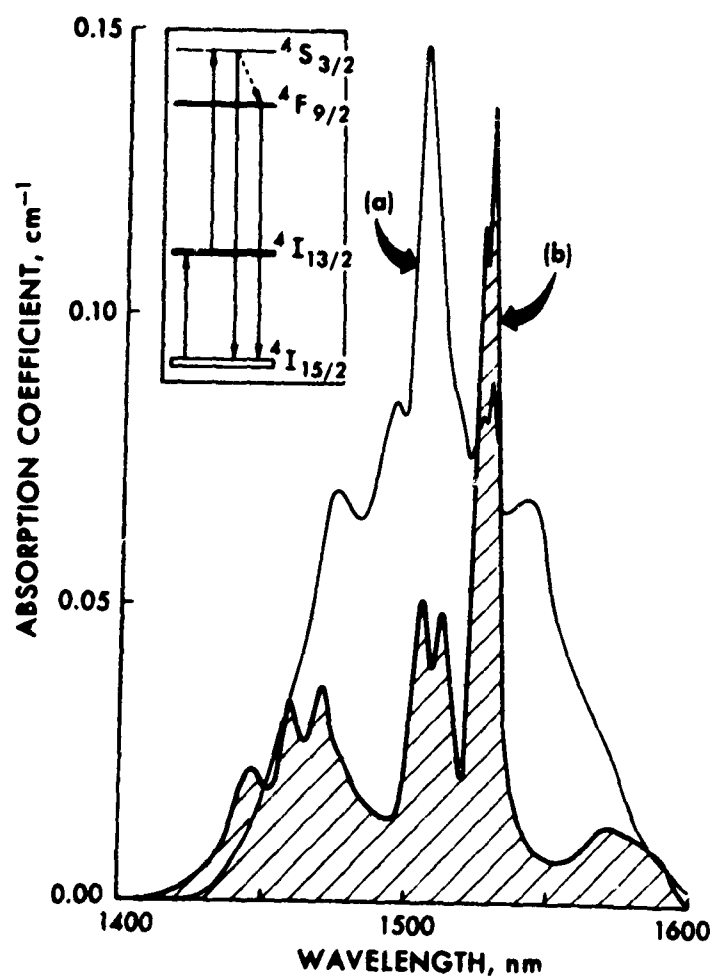


FIGURE 3. ABSORPTION SPECTRA OF  $\text{Er}^{3+}$  IN  $\text{CdF}_2$ . The ( $^4I_{15/2} \rightarrow ^4I_{13/2}$ )  $\text{Er}^{3+}$  optical absorption spectra of  $\text{CdF}_2$ :0.1 mole %  $\text{ErF}_3$  (at 295K): (a) ( $\text{Er}^{3+}, \text{U}$ ) (1507 nm maximum) and (b) ( $\text{Er}^{3+}, \text{C}^{2-}$ ) (1531 nm maximum).

UNCLASSIFIED

# UNCLASSIFIED

These results may be used to estimate the minimum detectable power (MDP) of an IRQC detector made with each of the differently prepared crystals. For this purpose, the IRQC material is assumed to be sandwiched between two GaAlAs injection laser arrays, with a third face cemented to a photomultiplier tube, and the signal radiation incident on a remaining face (Fig. 4). The crystal is assumed to have a sensitive area of  $1 \text{ mm}^2$  and a depth sufficient to absorb most of the incident signal (e.g., 3 mm for 2 mole % Er, c.f. Fig. 2).

For this analysis, it is assumed that the IRQC is photomultiplier noise limited. Other noise mechanisms were found to produce comparable contributions to the MDP, but with large uncertainties.<sup>(10)</sup> For circumstances in which the photomultiplier tube is the dominant noise source, the MDP of the system,  $P_{m1}$ , is related to the phototube MDP,  $P_{m2}$ , by

$$P_{m1} = P_{m2} / G \quad (1)$$

where the gain is defined as

$$G = \gamma I_p \beta_c \lambda_g / \lambda_0 \quad (2)$$

$\lambda_g$  is the signal wavelength,  $\lambda_0$  is the luminescence wavelength, and  $\beta_c$  is the luminescence collection efficiency (25% assumed).  $P_{m2}$  may be estimated from the MDP of the EMI 9502S photomultiplier<sup>(11)</sup> at 540 nm ( $6.6 \times 10^{-17} \text{ W}$ ) and the MDP of the EMI 9698B photomultiplier<sup>(11)</sup> at 660 nm ( $8.3 \times 10^{-16} \text{ W}$ ). The gain,  $G$ , is seen from Eq. (2) to be proportional to the pump intensity. For the present purpose, it is assumed that  $I_p = 100 \text{ W/cm}^2$ , a value that appears attainable with state-of-the-art injection laser arrays.<sup>(12)</sup>

The MDP's calculated in this manner for a signal wavelength corresponding to the maximum absorption are shown in the remaining columns of Table II. The results indicate that an IRQC prepared using the oxygen-fired crystal would have a sensitivity of  $3.6 \times 10^{-14} \text{ W}$  (at  $1.531 \mu\text{m}$ ), many times better than that of any of the more familiar uncooled detectors in the  $1.5 \mu\text{m}$  to  $1.6 \mu\text{m}$  region for an equal sensitive area ( $1 \text{ mm}^2$ ); e.g.  $\text{PbS}$  ( $1 \times 10^{-12} \text{ W}$ ),<sup>(13)</sup>  $\text{Ge}$  ( $2 \times 10^{-12} \text{ W}$ ),<sup>(14)</sup>  $\text{HgCdTe}$  ( $2.5 \times 10^{-12} \text{ W}$ ).<sup>(14)</sup>

Investigations are proceeding in an effort to obtain an efficient material with maximum sensitivity at  $1.536 \mu\text{m}$ . Preliminary measurements made on oxygen-fired (and hydrolyzed)  $\text{SrF}_2:\text{Er}^{3+}$  crystals indicate that this material provides a peak in the IRQC spectral response at  $1.536 \mu\text{m}$ , matching exactly the Er:phosphate glass laser emission.

Studies have been initiated also on some mixed fluoride single crystals, with encouraging results. Optical absorption measurements indicate that one of these fluorides also has a peak at  $1.536 \mu\text{m}$ , and preliminary double excitation experiments reveal that the conversion efficiency in the green ( $\gamma_0$ ) for this material is at least as high as that of  $\text{CdF}_2:(\text{Er}^{3+}, \text{O}^{2-})$  (c.f. Table II).

## ACKNOWLEDGEMENTS

The authors are indebted to R. G. Iye for valuable discussion and to W. R. Hosler of the Solid State Physics Section at NBS, Washington, D. C. for providing the crystals used in this study. W. Holton and J. Minnucci provided important technical assistance. We are also

UNCLASSIFIED

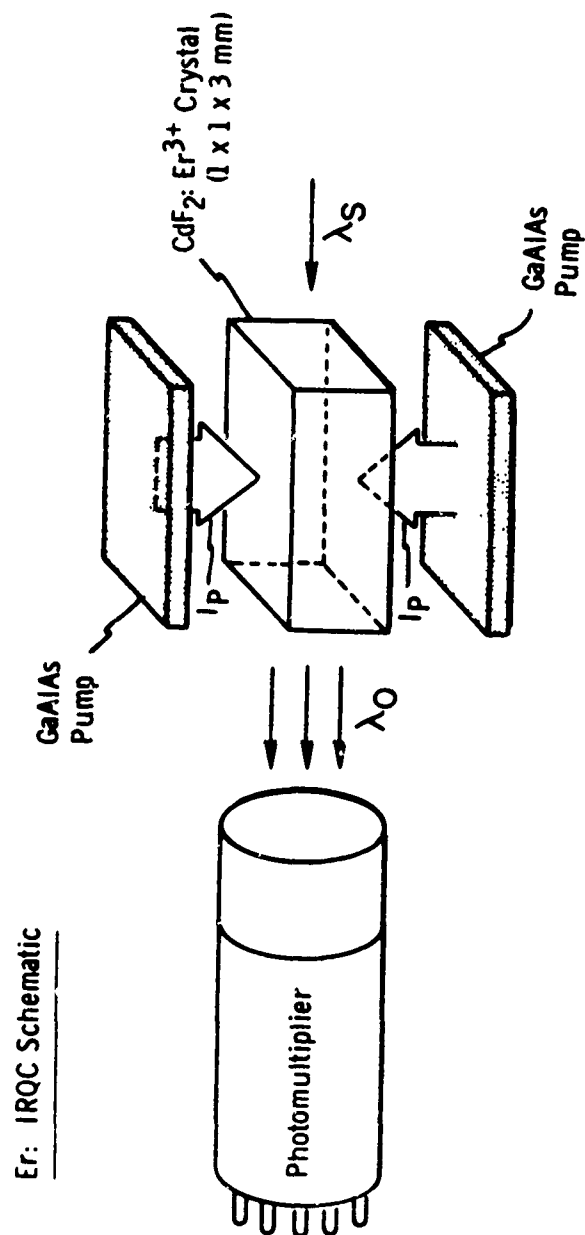


FIGURE 4. SCHEMATIC OF THE Er: IRQC. This scheme has been assumed in order to compute the MDP of differently prepared CdF<sub>2</sub>:Er<sup>3+</sup> crystals.

UNCLASSIFIED

## UNCLASSIFIED

grateful to H. Guggenheim of Bell Telephone Labs, Murray Hill, N. J. for providing the mixed fluoride crystals.

### REFERENCES

1. N. Bloembergen, Phys. Rev. Letters 2, 84 (1959).
2. W. F. Krupke, IEEE J. Quant. Electronics QE-1, 20 (1965).
3. L. Esterowitz, A. Schnitzler, J. Noonan, and J. Bahler, Appl. Optics 1, 2053 (1968).
4. N. E. Byer, T. C. Ensign, and W. M. Mularie, Appl. Phys. Letters 20, (1972).
5. C. G. Young, Proc. IEEE 57, 1267 (1969).
6. M. R. Brown and W. A. Shand, Phys. Rev. Letters 12, 367 (1964).
7. L. Esterowitz and J. Noonan, Appl. Phys. Letters 7, 281 (1965).
8. For example, J. G. Gualtieri, G. P. deIhery, T. R. AuCoin, J. R. Pastore, Appl. Phys. Letters 11, 389 (1967); Ref. 3; and Ref. 6.
9. N. E. Byer, T. C. Ensign, and W. M. Mularie, Bull. Am. Phys. Soc. 17, 310 (1972); T. C. Ensign, N. E. Byer, and W. M. Mularie, Bull. Am. Phys. Soc. 17, 310 (1972); and T. C. Ensign and N. E. Byer, to be published.
10. N. E. Byer, to be published.
11. EMI Photomultiplier Tubes and Accessories Catalog, 1970 Edition.
12. B. I. Miller, E. Pinkas, I. Hayashi, P. W. Foy and R. Capic, Appl. Phys. Letters 19, 340 (1971); B. I. Miller, J. E. Ripper, J. C. Dymont, E. Pinkas and M. E. Panish, Appl. Phys. Letters 18, 403 (1971); and M. Kressel, H. F. Lockwood and F. Z. Hawrylo, Appl. Phys. Letters 18, 43 (1971).
13. D. E. Bode, "Lead Salt Detectors," in Physics of Thin Films, G. Hass and R. E. Thun Eds. (Academic Press, N. Y. 1966), p. 275.
14. W. Scott, "(Hg,Cd)Te Photovoltaic Detectors in the Infrared," 1970 Solid State Sensors Symp., Minneapolis, 18-19 June, p. 75.

### QUESTION AND ANSWER SESSION

- Q. Have you made actual measurements of the minimum detectable power at 1.5  $\mu\text{m}$ ?
- A. Not yet.

Reverse page blank

# UNCLASSIFIED

.... This paper is UNCLASSIFIED

## DETECTION UNCERTAINTY (Unclassified)

S. R. Borrello  
Texas Instruments Incorporated  
Dallas, Texas 75222

### ABSTRACT (Unclassified)

A meaningful measure of photon detection includes the measurement time as well as ultimate sensitivity  $D^*$ . This approach considers the  $D^*f^*$  product as a constant of detection with the measurement time related to the frequency  $f^*$ . The upper limit on  $D^*f^*$  is  $(4\pi\epsilon)^{-1}(h/2m)^{1/2}$  with  $\epsilon$  the photon energy,  $h$  Planck's constant and  $m$  the electron mass. This approach suggests that maximum detection is determined by the quantum of least action of each independent absorption center.

The uncertainty in detection of photons covering the spectrum from visible to far infrared has been expressed <sup>(1)</sup> in terms of the noise equivalent power, NEP, or the related function, detectivity,  $D^*$ . The theoretical limit of  $D^*$  is determined by random generation and recombination of photo-generated free charge carriers <sup>(2)</sup>. Fluctuations in arrival of photons at the detector are only accessible via the transducing mechanism of the detector such as photoconductivity. Assuming the information containing photons (signal photons) cannot be spectrally differentiated from the background photon flux, detection is restricted to temporal variations in the total photon flux density and is manifested via Fourier analysis of the fluctuations using a filtered integrator e.g. sound analyzer. The sensitivity of the measurement,  $D^*$ , depends on the detection frequency beyond some frequency  $f^*$  where the Fourier components of the photon fluctuations are less than those associated with the internal energy.

For frequencies below  $f^*$  detectivity in principle can be arbitrarily increased by reducing the photon density and thereby its associated fluctuations. The frequency limit on  $D^*$  is a manifestation of the uncertainty in the action associated with detection. The detector acting as an array of photon counters is limited in count per bandwidth (count uncertainty) because each photon absorbed has a defined minimum energy  $\epsilon$ .

In particular consider the definition <sup>(1)</sup>

$$D^* \equiv \frac{I_R (A \Delta f)^{1/2}}{I_N} \quad (1)$$

with  $I_R$  the current responsivity,  $A$  the detector area,  $\Delta f$  the amplifier bandwidth and  $I_N$  the mean noise current associated with  $\Delta f$  is the Fourier transform of the current fluctuations <sup>(3)(4)</sup>  $\delta I$ . When the fluctuations in the background photon flux dominate then  $\delta I = \delta(qQA)$  where  $q$  is the elec-

# UNCLASSIFIED

tronic charge and  $Q$  is the background photon flux. Although fluctuations in the photon count may be obtained in a variety of ways it is convenient to define an energy<sup>(5)</sup>

$$E \equiv eQ\Delta\tau. \quad (2)$$

The carrier lifetime  $\tau$  establishes the steady state number of carriers  $E/e$  associated with the fluctuations. Thus  $\tau$  is the minority carrier lifetime for an impurity dominated intrinsic detector<sup>(6)</sup> such as HgCdTe or InSb or the majority carrier lifetime for extrinsic detection as with Ge:Hg. Therefore

$$\delta I = \frac{q}{\tau} \delta \left( \frac{E}{e} \right) \quad (3)$$

with  $\delta(E/e) = (E/e)^{1/2}$  when the fluctuations are mutually independent<sup>(3)</sup>. Taking the Fourier integral of Equation 3 over  $\tau$ , the specific noise current,

$$I_N^2 = 4 \frac{q^2}{\tau} \left( \frac{E}{e} \right) \Delta f, \quad (4)$$

the 4 representing the recombination as independent of the generation. Since the specific current responsivity<sup>(2)</sup> is simply  $q/e$  assuming no losses by reflection, transmission or non-participating absorptions (e.g. by free carriers), Equation 1 can be written

$$\frac{D^*}{\tau} = \left( \frac{A}{4eE\tau} \right)^{1/2}. \quad (5)$$

The product  $E\tau$  is the action associated with fluctuations of the number  $E/e$ . The detection  $D^*/\tau$  is optimum for least fluctuations and therefore least action in the detector of area  $A$ . The fluctuations are independent implying that the least action for  $A$  is equal to the least action per absorption of cross-section  $\sigma$ . That is

$$\text{Minimum } \frac{E\tau}{A} = \frac{\hbar}{\sigma} \quad (6)$$

where  $\hbar$  as given by the Uncertainty Principle is the least action associated with the energy transfer from photon to charged particle as measured in time  $\tau$ . Therefore

$$\text{Maximum } \frac{D^*}{\tau} = \left( \frac{\sigma}{4e\hbar} \right)^{1/2} \quad (7)$$

# UNCLASSIFIED

The constant ratio  $D^*/\tau$  suggests that detector sensitivity and speed are mutually limiting in a fundamental sense. Thus a decrease in  $\tau$  by some artificial means (e.g. introduction of defect states) implies a corresponding limit on achievable  $D^*$  providing the detector already has a  $D^*/\tau$  value close to that given by Equation 7. However larger  $\tau$  does not guarantee improved  $D^*$  since only an upper limit has been derived.

These results suggest that  $D^*$  decreases as a function of frequency beyond a particular frequency  $f^*$ . The upper limit on  $D^*/\tau$  implies a lower limit on  $\tau$  given by  $(2\pi f^*)^{-1}$ . If for example a photoconductor is operated in the background limited mode<sup>(7),(8)</sup> a hypothetical reduction in  $\tau$  would reduce the responsivity and noise identically and  $D^*$  would remain constant until the noise is no longer a function of  $\tau$  (e.g. Nyquist noise). At this point  $\tau = \tau^*$  and these results as elsewhere<sup>(9),(10)</sup> imply no further reduction in noise is possible since from Equations (1) and (7)

$$\frac{I_N}{(\Delta f A)^{1/2}} > \frac{I_R}{\tau} \frac{(4e\hbar)^{1/2}}{\sigma} \quad (8)$$

Equation (7) becomes

$$\text{Maximum } D^* f^* = \frac{1}{2\pi} \left( \frac{\sigma}{4e\hbar} \right)^{1/2} \quad (9)$$

Thus ultimate  $D^*$  is a reciprocal function of the frequency and for example  $D^* f^*$  has a value of  $6 \times 10^{17} \text{ cm Hz}^{1/2}/\text{Joule}$  when  $\epsilon = 0.1 \text{ eV}$  and  $\sigma = 10^{-16} \text{ cm}^2$ .

The photon capture cross-section may have a physical significance implied by least action. Consider the electron angular momentum in units of  $\hbar$

$$2\pi m v_e r^2 = n\hbar \quad (10)$$

where  $m$  is the mass,  $v_e$  the orbital frequency, and  $r$  the orbital radius of the  $n$ th quantum state. If  $\pi r^2$  can be considered the electron spatial uncertainty equal to  $\sigma$  and since  $v_e/n$  is the photon frequency  $\nu_p$  then

$$\sigma = \frac{\hbar^2}{4\pi m \epsilon} \quad (11)$$

with  $\epsilon = h\nu_p$ .

Equation (9) becomes

$$D^* f^* = \frac{1}{4\pi \epsilon} \left( \frac{\hbar}{2m} \right)^{1/2} \quad (12)$$

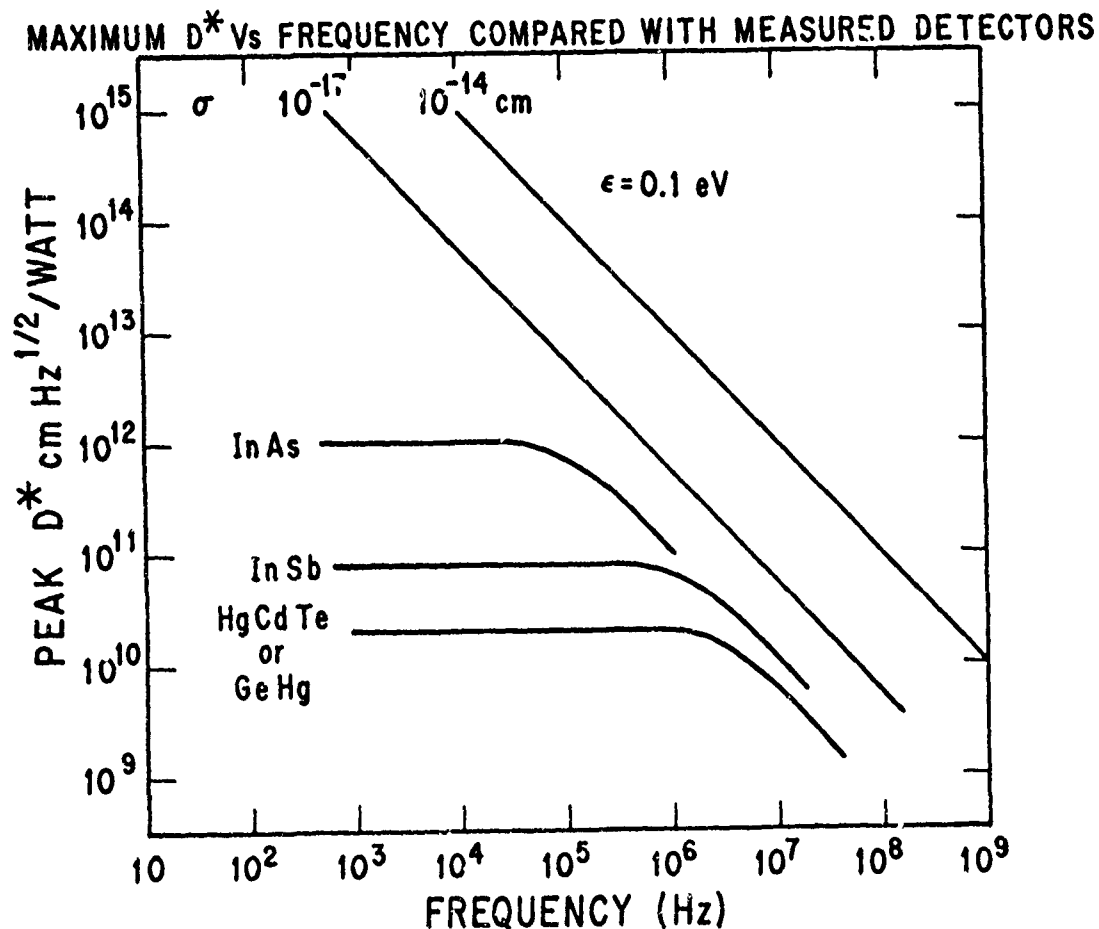
# UNCLASSIFIED

These results express the idea that detection of photons is ultimately limited by the fact that electrons are the transducing particles acting independently for a characteristic time  $\tau$  with least action  $\hbar$ .

The practical implications of detection uncertainty are indicated in figure 1. The curve for  $\sigma = 10^{-14} \text{ cm}^2$  is from Equation (12) whereas the experimental value<sup>(11)</sup>  $10^{-17} \text{ cm}^2$  is used in Equation (9). Available data<sup>(3),(6)</sup> for InAs, InSb photodiodes and HgCdTe, Ge:Hq photoconductors suggests the curves as shown and particular  $D^*/\tau$  predictions are available<sup>(12)</sup>. These results imply that any increase in  $D^*$  for a particular detector must result in a decrease in  $f^*$ .

The small value for  $\sigma$  calculated from measured data, including corrections for reflection and transmission, may result from overlap of absorption centers and the poor assumption that  $n$  is a good quantum number for the energy states in a solid. This problem requires more study as does the basic premise set forth here that maximum detection is determined by the quantum of least action of each independent absorption center.

The author is grateful to Henry Levinstein and Robert L. Williams for encouragement and suggestions.





# UNCLASSIFIED

## REFERENCES

1. R. C. Jones, Advances in Electronics V, Academic Press, New York (1953), p. 1; Advances in Electronics, XI, Academic Press, New York (1959), p. 87.
2. R. A. Smith, F. E. Jones, R. P. Chasmar, The Detection and Measurement of Infrared Radiation, Oxford at the Clarendon Press (1968), p. 322.
3. J. A. Jamieson, et al., Infrared Physics and Engineering, p. 186, McGraw-Hill Book Company, New York, 1963.
4. A. van der Ziel, "Fluctuation Phenomena in Semiconductors," Academic Press, New York (1959).
5. D. Gabor, Phil. Mag. 41, 7, p. 1161, 1950.
6. R. K. Willardson and Albert C. Beer, Semiconductors and Semimetals, 5 Infrared Detectors, Academic Press, New York (1970).
7. K. M. van Vliet, Applied Optics, 6, No. 7, 1145 (1967).
8. J. A. Jamieson, ibid, p. 389.
9. J. A. Jamieson, ibid, p. 375.
10. H. B. Callen, T. A. Welton, Phys. Rev., 83, No. 1, July 1, 1951.
11. S. R. Borrello, C. G. Roberts, B. H. Breazeale and G. R. Pruett, Infrared Physics, 11, 235, 1971.
12. R. L. Williams, Infrared Physics, 9, pp. 37-40, 1969.

Reverse page blank

# UNCLASSIFIED

.... This paper is UNCLASSIFIED

## PREPARATION OF (Hg,Cd)Te BY A NEW HIGH PRESSURE FURNACE TECHNIQUE (Unclassified)

Jacques Steininger, J. F. Butler, and J. B. Sohn

Detection Sciences Division  
Arthur D. Little, Inc.  
Cambridge, Mass. 02140

### ABSTRACT

High quality  $\text{Hg}_{1-x}\text{Cd}_x\text{Te}$  crystals, with  $x$  ranging from 0.15 to 0.40, have been prepared in a high pressure furnace (100 atm.) using a newly developed technique which eliminates the hazards associated with failure of sealed quartz ampoules and makes it possible to prepare crystals of large dimensions and high  $x$  values. It also allows direct and precise control of the vapor pressure over the charge during the critical stages of crystallization and annealing. This gives the possibility to move across the (P,T) phase diagram and proceed through all preparation stages without intermediate handling of the crystals. The result is significantly improved material with reduced impurities and defects.

As-grown ingots, 1 in. in diameter by 2 in. long, have been obtained which contained several large crystals, up to 1 in. in diameter and 100 g. in weight. Low carrier concentration and high mobility values have been obtained by Hall measurements. The mobility values for several of the samples (up to  $1.2 \times 10^6 \text{ cm}^2/\text{v-sec}$  at liquid nitrogen temperature) are believed to be the highest reported for (Hg,Cd)Te at this temperature.

---

### 1. INTRODUCTION

$\text{Hg}_{1-x}\text{Cd}_x\text{Te}$  is a ternary alloy material which is characterized by a high melting temperature (from 670°C to 1092°C depending on the  $x$  value) and a high vapor pressure over the melt (in excess of 19 atmospheres). The vapor phase is almost entirely constituted of Hg and special techniques have to be used to prevent explosive reaction or decomposition of the material during synthesis and crystal growth.

Conventional techniques for the growth of  $\text{Hg}_{1-x}\text{Cd}_x\text{Te}$  crystals are essentially Bridgman or solution techniques based on the use of narrow, heavy-walled sealed quartz ampoules which are

## UNCLASSIFIED

specially designed to contain the high vapor pressure of Hg. However, because of the relatively low mechanical strength of quartz at high temperature, these techniques are quite hazardous and often result in failure of the ampoule by explosion of the highly reactive material. The problem becomes more severe for short-wavelength material with high Cd content (high x values) because of the higher temperatures and higher pressures required for melting. Because of these difficulties, the preparation of  $\text{Hg}_{1-x}\text{Cd}_x\text{Te}$  crystals by conventional techniques is slow, limited to ingots of small diameter and difficult to apply to material with high x values.

### 2. HIGH PRESSURE FURNACE TECHNIQUE

This communication describes a new technique for the preparation of  $\text{Hg}_{1-x}\text{Cd}_x\text{Te}$  in a high pressure furnace which avoids the hazards associated with failure of sealed quartz ampoules and makes it possible to prepare crystals of large dimensions and high x values. It also allows direct control of the vapor pressure over the melt during the critical stages of crystallization and annealing. This gives the possibility to move across the (P,T) phase diagram and proceed through all preparation stages without intermediate handling of the crystals.

The high pressure furnace is a Model HP Crystal Growing Furnace fabricated by A. D. Little, Inc. It is designed to operate at temperatures up to 1600°C and pressures up to 100 atmospheres of inert gas. Heating is by resistance heating of a 2.25 in. I.D. x 5 in. H. graphite crucible. The dimensions of the high pressure chamber are approximately 7 in. I.D. x 20 in. H. The walls and seals are cooled by water circulating through coils on the outside of the chamber. The particular unit used in our laboratory is equipped with two vertical pulling heads which allow synchronized or independent rotation and vertical translation of the crucible stage and upper monitoring thermocouple. Two water-cooled quartz windows allow direct viewing or remote TV control of the interior of the pressure chamber. This unit is suitable for either Bridgman growth, solution zoning or Czochralski crystal pulling.

It should be noted that the walls and seals of the high pressure chamber have to be cooled to retain their desirable mechanical properties. This cooling, however, creates large temperature differences between the heated crucible region and the colder outer areas of the pressure chamber. Even under high inert gas pressure, therefore, the volatile species tend to evaporate and diffuse toward the cold areas of the furnace. To prevent or reduce decomposition of the volatile material, it is still necessary to introduce sealing devices between hot and cold regions.

The simplest sealing devices for high pressure furnaces are sealed quartz ampoules. By carefully balancing the inert gas pressure inside the furnace and the vapor pressure of the volatile species inside the sealed ampoule, it is possible to reduce the stress on the ampoule walls. However, miscalculation or sudden variation of the inside vapor pressure frequently leads to failure of the ampoule, either by implosion or explosion.

## UNCLASSIFIED

A major advance was made a few years ago with the development of the liquid encapsulation technique. A molten layer of an inert, viscous and transparent liquid, such as boric oxide,  $B_2O_3$ , is placed over the volatile material to form a liquid diffusion barrier. A high inert gas over-pressure is then applied over the liquid encapsulant to contain the volatile species. Crystal pulling of GaP is now routinely done by the liquid encapsulation technique.

We have made several unsuccessful attempts to apply the liquid encapsulation technique to the preparation and growth of (Hg,Cd)Te crystals. The first difficulty was caused by the relatively high melting point of  $B_2O_3$  (around  $450^\circ C$ ) which prevents the formation of a liquid encapsulation layer over the charge during the highly energetic reaction of the starting materials. A second difficulty, similar in a sense to the first one, is caused by the high viscosity of  $B_2O_3$  over the temperature range ( $640^\circ C$  and less) required for crystallization and annealing of (Hg,Cd)Te. This high viscosity prevents the formation of a vapor-tight encapsulation layer during melting and annealing. A third problem, of a more general character, is due to the observed contamination of II-VI materials by  $B_2O_3$ . So far, therefore, very little success has been achieved in the preparation of this type of material by the liquid encapsulation technique.

A new containment technique without liquid encapsulant has now been developed to overcome these difficulties (1). It allows rapid reaction of the starting elements (1/2 hour instead of several days) with no measurable loss of volatile material and with direct control over the Hg vapor pressure during crystallization and annealing. It has now been successfully applied to the preparation of  $Hg_{1-x}Cd_xTe$  crystals with  $x$  ranging from 0.15 to 0.40 and is expected to perform equally well at higher  $x$  values.

In a typical run, a stoichiometric charge of the high purity elements plus a small excess of Hg is loaded into a specially designed carbonized quartz ampoule. The ampoule is placed inside the high pressure furnace which is first evacuated several times to eliminate oxygen and then pressurized with high purity argon to the maximum working pressure of 100 atmospheres. The charge is rapidly taken over the reaction temperature (around  $350^\circ C$ ), melted, homogenized for one hour above the liquidus temperature and then rapidly solidified by quenching to a temperature below the solidus temperature. Because of the high inert gas pressure and strong convection currents in the pressure chamber, extremely rapid quenches (up to  $100^\circ C/min.$ ) can be obtained if desired. During solidification, the inert gas pressure is slightly reduced and precisely controlled to avoid the formation of metallic Te inclusions or blow-holes due to trapped excess Hg. Crystallization is then achieved by a high temperature anneal of several days. A second anneal at lower temperature and reduced Hg vapor pressure is finally made for stoichiometric adjustment and control of the electrical properties of the crystals.

## UNCLASSIFIED

Wafers are cut from the large ingots with a wire saw or laboratory I.D. slicing machine. Small Hall bars are then diced with the wire saw, lapped, polished and etched with the usual bromine-methanol mixture. The composition of the samples is determined either from the specific gravity or by electron microprobe analysis.

### 3. RESULTS

As-grown ingots, 1 in. in diameter by 2 in. long, have been obtained which contained several large crystals, up to 1 in. in diameter and 100 g. in weight. Figure 1 is a photograph of an ingot from an early run showing several large single crystals. By controlling the growth parameters, it has been found possible to prepare in a reproducible way, material with either metallic Te inclusions (Fig. 2A), excess Hg blow-holes (Fig. 2B) or uniform material free of microscopic inclusions (Fig. 2C). Figure 2C is an X-ray microphotograph for the Cd  $L_{\alpha}$  line. The random distribution of black and white dots shows the uniformity of the sample and the absence of microscopic inhomogeneities.

Spectroscopic analysis of the high purity starting elements and of several grown crystals showed no evidence of impurities being incorporated during crystal growth and annealing.

Hall measurements were made by the Van der Pauw technique at liquid nitrogen and room temperatures and at magnetic fields ranging from 4900 to 61 gauss. The results of these measurements (Table I) show that either p or n-type material with high mobility and low carrier concentration values can be produced by this technique. Of particular interest are the mobility values obtained for either p or n-type material. The mobility values for n-type material are believed to be the highest reported for  $Hg_{1-x}Cd_xTe$  at liquid nitrogen temperature. Similarly, the values obtained for p-type material are remarkably high. The mobility and carrier concentration data for several n-type samples of Table I have been plotted against theoretical curves calculated by Long (2). Figure 3 shows that the mobility values are very close to the theoretical values calculated for liquid helium temperature. On Figure 4, the carrier concentrations for the same samples are also seen to be in close agreement with the theoretical intrinsic carrier concentration curves at both liquid nitrogen and room temperature.

It should be noted that high mobility values can sometimes be explained by the presence of metallic inclusions in the crystal (3). However, careful examination of polished samples by optical microscopy and electron microprobe analysis showed no evidence of a metallic second phase. In addition, the mobility was found to remain essentially constant when the magnetic field was varied from 4900 to 61 gauss, in agreement with the conclusions of a recent study of the effects of metallic impurities in semiconductors (3).

## UNCLASSIFIED

High mobility values are usually taken as evidence of high crystalline perfection. We believe that this result is due to the particular preparation technique of large, bulky crystals relatively insensitive to thermal transients, under controlled vapor pressure of Hg, and to the elimination of intermediate handling steps which often result in the introduction of impurities and defects.

Photoconductive infrared detectors have been fabricated from these crystals. Operating characteristics will be presented and discussed at a later date.

### ACKNOWLEDGMENTS

The authors wish to acknowledge the capable technical assistance of F. L. Johnston, J. B. Weltchek, and R. J. Woods.

### REFERENCES

- (1) J. Steininger, to be published
- (2) D. Long, Phys. Rev. 176, 923 (1968)
- (3) C. M. Wolfe, G. E. Stillman, and J. A. Rossi, J. Electrochem. Soc. 119, 250 (1972)

UNCLASSIFIED

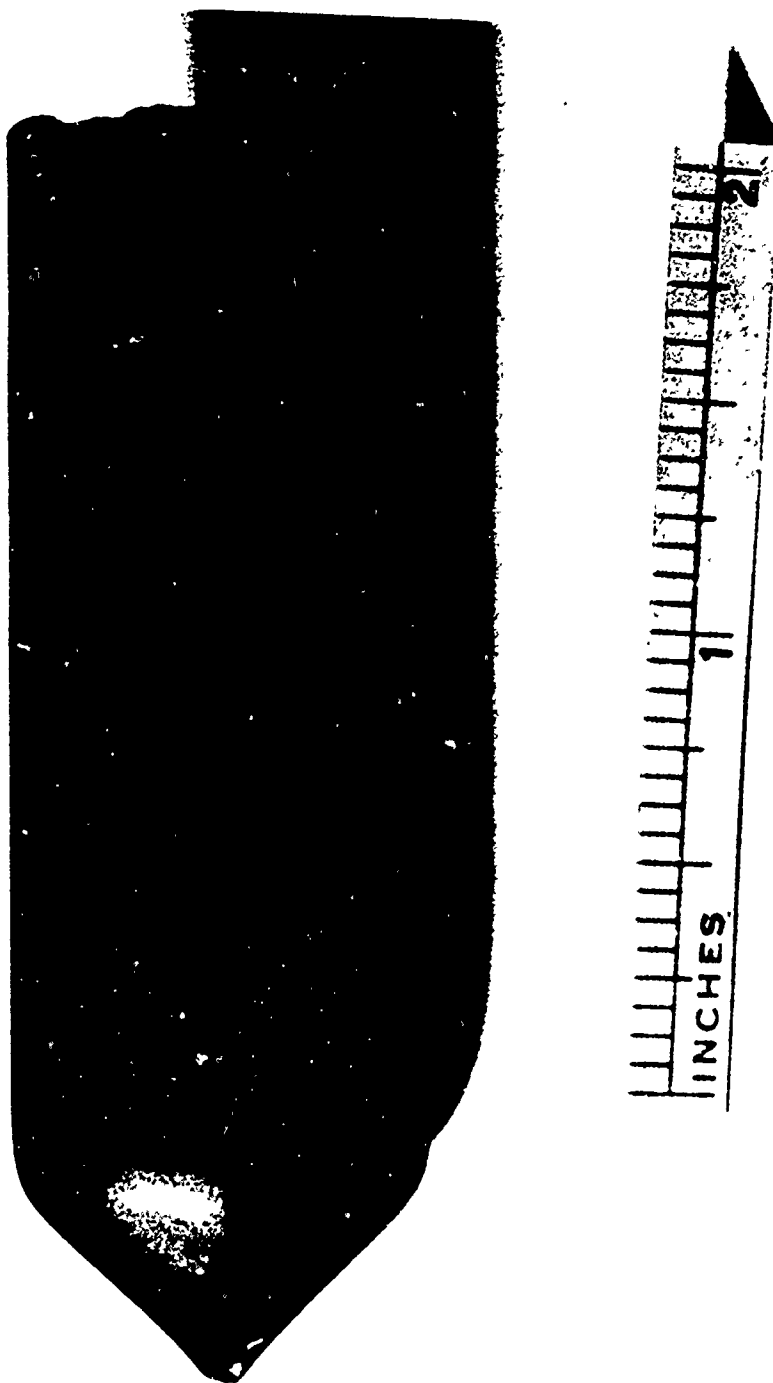


FIGURE 1. PHOTOGRAPH OF  $(\text{Hg,Cd})\text{Te}$  INGOT GROWN BY THE  
HIGH PRESSURE FURNACE TECHNIQUE

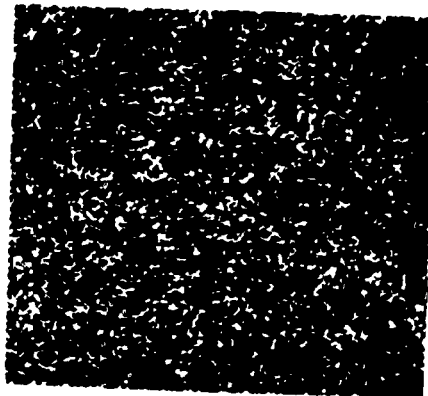
UNCLASSIFIED

UNCLASSIFIED



A. Optical Photograph (5X) showing dendritic structure with excess Te

B. Optical Photograph (50X) showing large uniform areas and small blow-holes due to excess Hg



C. X-ray Photograph (600X) showing uniform concentration of Cd (uniform density of black and white dots)

FIGURE 2. MICROPHOTOGRAPHS OF (Hg,Cd)Te POLISHED WAFERS

UNCLASSIFIED



UNCLASSIFIED

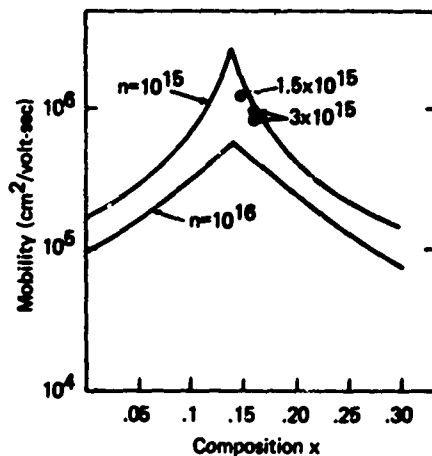


FIGURE 3. COMPARISON OF EXPERIMENTAL MOBILITY VALUES WITH THEORETICAL CURVES

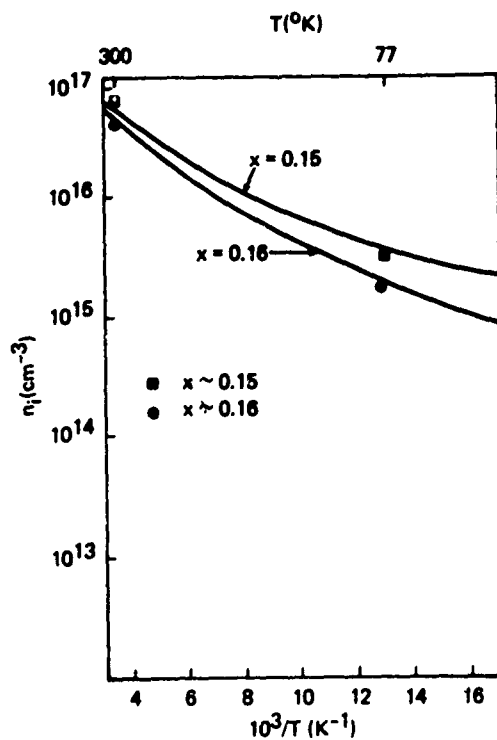


FIGURE 4. COMPARISON OF EXPERIMENTAL CARRIER CONCENTRATION DATA WITH THEORETICAL INTRINSIC CARRIER CONCENTRATION CURVES

UNCLASSIFIED

# UNCLASSIFIED

TABLE I

## ELECTRICAL PROPERTIES OF HP FURNACE GROWN Hg<sub>1-x</sub>Cd<sub>x</sub>Te CRYSTALS

Sample	Composition x	Temperature °K	Type	Mobility cm <sup>2</sup> /v-sec	Carrier Concentration cm <sup>-3</sup>
10-38A	.21	77	P	$8.27 \times 10^2$	$1.09 \times 10^{16}$
9-16A	.16	77	N	$8.24 \times 10^5$	$2.92 \times 10^{15}$
		300	N	$2.54 \times 10^4$	$6.46 \times 10^{16}$
9-16H2	.16	77	N	$7.62 \times 10^5$	$3.28 \times 10^{15}$
9-17A	.16	77	N	$1.25 \times 10^6$	$1.5 \times 10^{15}$